UNIVERSIDADE FEDERAL DE MINAS GERAIS

Programa de Pós-Graduação em Engenharia Metalúrgica, Materiais e de Minas

Tese de Doutorado

Flexible TiO_2 coating on superelastic NiTi alloys for bioapplications

Autor: Diego Pinheiro Aun

Orientadores: Prof. Dr. Vicente Tadeu Lopes Buono
Prof. Dr. Grégory Berthomé

Fevereiro/2016

Diego Pinheiro Aun

Flexible TiO_2 coating on superelastic NiTi for bioapplications

Tese apresentada ao Programa de Pós-Graduação em Engenharia Metalúrgica, Materiais e de Minas da Escola de Engenharia da Universidade Federal de Minas Gerais, como requisito parcial para obtenção do Grau de Doutor em Engenharia Metalúrgica, Materiais e de Minas.

Área de Concentração: Metalurgia Física.

Orientadores: Prof. Dr. Vicente Tadeu Lopes Buono.
Prof. Dr. Grégory Berthomé

Belo Horizonte
Universidade Federal de Minas Gerais
Escola de Engenharia
2016

Acknowledgements

During the years spent with this research I met a lot of good people who helped me directly or indirectly with my work. I would like to thank them all but the list of names would be huge. I saved this space to express my gratitude to a few specific ones who helped actively for the development of this study.

First, I would like to thank Prof. Dr. Damien Fabrègue and Prof. Dr. José Antônio da Cunha Ponciano Gomes for accepting the invitation to be the thesis reviewers in a so short notice. I also like to thank Prof. Dr. Laurence Latu-Romain and Prof. Dr. Ana Cecília Viana Diniz who also accepted the invitation to be a part of the jury.

I would like to thank my supervisors Prof. Dr. Vicente Tadeu Lopes Buono and Prof. Dr. Grégory Berthomé who accepted me as their student, teaching a lot about how to produce science and giving me all the resources necessaire to complete this thesis. They both work hard in this study, mainly in this final part.

A special thank you needs to be given to Prof. Dr. Manuel Houmard. He was always available to help me and his knowledge in chemistry and in sol-gel was fundamental to obtain the main results of the study. He was also the link connecting Brazil and France for this partnership that generates a cotutelle agreement between these two countries and that can generate other future collaborations.

A big part of the thesis theme involved knowledge about endodontics which was a completely new subject for me. To ease the transition between exact sciences and dentistry I could count with the patience, dedication and good mood of Dr. Isabella Faria da Cunha Peixoto, known by everybody as Bebel. She would always bring up everyone’s spirit up during working days and was always thinking positively. Her knowledge in endodontics was also fundamental for the development of this research.

Throughout my stay in France I had the assistance of several people. I have to thank a lot Prof. Dr. Jean-Charles Joud and Prof. Dr. Laurence Latu-Romain who participated in several meetings about my results enduring my terrible french and giving brilliant ideas about experiments that generated excellent results. I also would like to thank Prof. Dr. Michel Mermoux who helped me with the Raman experiments and Jacqueline Cuoq who assisted me a lot with bureaucratic and non-bureaucratic work.

For the corrosion tests, I had the help of Dr. Dalila Sicupira and Prof. Dr. Vanessa de Freitas Cunha Lins. They opened their lab for me and taught me a little about corrosion which is a vast and difficult subject that was essential in my investigation.

I also had the assistance of Prof. Dr. Andrea Bicalho Henriques and Patrícia Mara Trigueiro de Azevedo who were always eager to help irrespective if the subject rely on their specialty.

Likewise, I want to thanks the grad student Pedro Damas who spent some of his reduced free time to assist or perform some of the experiments needed for the research.

My friend Fernando Guedes (Bamboo) produced some very nice figures for this thesis and the presentation and deserves my recognition. Thank you, Bamboozim.

My girlfriend Fernanda Souza Sabatini was too very helpful to the progress of the work. She gave me comfort and strength, mainly in this final part, having the patience to withstand my bad mood caused by the high stress with the deadlines and non-working experiments. She supported all my decisions and was always present for me, even when I was in France.

Finally, I want to thank my parents, Msc. Miguel Ricardo Aun and Prof. Dr. Marta Macedo Kerr Pinheiro, who encouraged me to pursue an academic career and gave me all the support I needed in life. Being a professor in the UFMG University, my mother was able to give me some very good advice during the most difficult times of the post-graduation.

To all those above mentioned, my sincere thank you!

Summary

List of figures

List of tables

Acronyms

A_f	Austenitic final temperature
AFM	Atomic force microscopy
A_n	Annodizing
A_p	Austenitic peak temperature (DSC)
AR	As received (endodontic instrument control group)
A_s	Austenitic start temperature
BE	Binding energy
Ce	Chemically etched
CI	Coated instruments (endodontic instruents)
Ep	Electropolishing
FWHM	Full width at half-maximum
GIXRD	Grazing incidence X-ray diffraction
Ht	Heat treated
M_d	Maximum temperature to form stress-induced martensite
M_f	Martensitic final temperature
M_p	Martensitic peak temperature
M_s	Martensitic start temperature
MT	Martensitic transformation
N_f	Number of cycles until fracture
SE	Superelastic
SEM	Scanning electron microscopy
SIM	Stress-induced martensite
SMA	Shape memory alloy
SME	Shape memory effect
Td	Deformation temperature
TEM	Transmission electron microscopy
TT	Thermally treated group (endodontic instruments)
Wb	Water boiled
XPS	X-ray photoelectron spectroscopy
XRD	X-ray diffraction

ABSTRACT

In this work, a dip-coating sol-gel deposition route was developed to coat superelastic NiTi alloy with a flexible TiO_2 protective layer. The film was produced by emerging the samples at 7.5 mm/s and thermally treating at 100ºC in a humid atmosphere for 45 min, 110ºC in a dry atmosphere for 2 hours and at 500ºC for 10 min. The film was first deposited over chemically etched substrates and characterized by SEM, TEM, AFM, GIXRD, XPS, Raman cartography and three-point bending tests. Results showed that a ~100 nm nanocomposite film constituted of amorphous TiO_2 on the upper half and a mixture of 10 to 50 nm anatase and rutile grains on the oxide/metal interface was formed. This film was capable of sustaining up to 6.4% strain without cracking or peeling. A high decrease in the concentration of Ni at the surface was measured, indicating that an increase in the biocompatibility of the material was achieved. Besides, this route was used to coat NiTi endodontic instruments Model RaCe 25/0.06, which were tested regarding fatigue life, cutting efficiency and corrosion resistance in NaClO. Results showed a statistically significant improvement in fatigue life for the coated instruments, mainly after corrosion tests. Cutting efficiency measured by an original developed technique was similar for coated and uncoated endodontic instruments.

Key words: flexible ceramic, TiO_2 film, sol-gel, NiTi alloys, endodontic instruments, fatigue, corrosion.

RÉSUMÉ

Dans cette étude, nous avons élaboré un revêtement de TiO_2 par sol-gel sur des alliages super-élastiques de NiTi. L'idée générale était de développer une couche mince de TiO_2 protectrice et flexible. Le film mince est formé en immergeant les échantillonsde NiTi, préalablement chimiquement gravés, dans une solution réactive à 7,5 mm/s, puis en effectuant plusieurs traitements thermiques :un premier traitement thermique à 100 °C pendant 45 minutes dans une atmosphère humide, un deuxième traitement à 110 °C pendant 2 heuresdans une atmosphère sèche et enfin un dernier traitement à 500 °C pendant 10 minutes. Les couches minces de TiO_2 ont été caractérisé par de laflexiontrois points, par MEB, par MET, par AFM, par GIXRD, par XPS et par de la cartographie Raman. Les résultats de l'étude ont montré un film nanocomposite, avec ~100 nm de TiO_2 amorphe formé à l'interface externe de la couche et d'un mélange de grains cristallisés de 10 à 50 nm, d'anatase et de rutile à l'interface interne métal/oxyde. Cette hétéro-structure est capable de soutenir 6,4% de déformation sans l'apparition de défauts plastiques majeurs (cloques, fissures...). Une faible concentration de Ni a été observé au niveau de la surface externe des couches minces de TiO_2, ce qui se traduit par une augmentation de la biocompatibilité du matériau. La technique sol-gel a été utilisée pour revêtir des instruments endodontiques modèle RaCe 25/0.06. Ce deuxième système a été testé à la fois en fatigue pour estimer sa durée de vie, et à la résistance à la corrosion en NaClO, et à des températures correspondant aux transformations de phase. Les résultats ont montré une augmentation statistiquement significative de la durabilité en fatigue, en particulier après les essais de corrosion. L'efficacité de la « coupe », mesurée par une procédure originale, a été similaire aux instruments revêtus et non revêtus. Le traitement thermique n'a pas été suffisamment efficace pour modifier de façon significative les températures de transformation de phase : le comportement mécanique d'origine de l'instrument a été maintenu.

Mots Clés : alliages NiTi, céramique flexible, corrosion, fatigue, film de TiO_2, instruments endodentiques, sol-gel

RESUMO

Neste trabalho foi desenvolvida uma rota de deposição sol-gel por imersão para revestir ligas de NiTi superelásticas com uma camada protetora e flexível de TiO_2. O filme formado pela emersão de amostras a 7,5 mm/s seguida de tratamentos térmicos a 100ºC por 45 minutos em atmosfera úmida, 110ºC por 2 horas em atmosfera seca e 500ºC por 10 minutos. O filme foi depositado sobre substratos decapados quimicamente e caracterizados por MEV, MET, AFM, GIXRD, XPS, cartografia Raman e dobramento de três pontos. Resultados mostraram que um filme nanocompósito com ~100 nm constituído de TiO_2 amorfo na metade superior e uma mistura de grãos de 10 a 50 nm de anatase e rutila na interface metal/óxido foi formado. Este filme é capaz de sustentar 6,4% de deformação sem trincar ou descamar. Uma grande redução na concentração de Ni na superfície foi detectada, indicando um aumento na biocompatibilidade do material. A rota foi usada para revestir instrumentos endodônticos de NiTi modelo RaCe 25/0.06 que foram testados em relação à vida em fadiga, eficiência de corte, resistência à corrosão em NaClO. Detectou-se um aumento estatisticamente significativo na vida em fadiga, especialmente após os ensaios de corrosão. A eficiência de corte, medida por um procedimento original desenvolvido, foi similar para instrumentos revestidos e não revestidos. O tratamento térmico não foi suficiente para alterar significativamente as temperaturas de transformação de fases, mantendo o comportamento mecânico original do instrumento.

Palavras-chave: cerâmica flexível, corrosão, fadiga, filme de TiO_2, instrumentos endodônticos, ligas NiTi, sol-gel.

1. Introduction

Equiatomic NiTi is the shape memory alloy with one of the highest recoverable strain of 8% in its polycrystalline state. Its differential mechanical properties associated with shape memory effect classifies NiTi as a smart material used for the manufactory of devices in numerous areas, such as protection plates against seismic vibrations, non-welding connectors, thermal sensors and actuators, flexible antennas, interior design objects and even in the textile sector as smart clothes.

However, the major application area for this metal is in biomedicine and dentistry areas. A natural passive TiO_2 layer is formed on the surface of NiTi alloys, making them chemically stable, favoring their use inside the highly corrosive human body. Main applications include orthopedic implants, endovascular stents and filters, flexible guide catheters and orthodontic arch wires. The only disadvantage for this kind of application is the possibility of the release of small quantities of Ni, which can trigger allergenic and carcinogenic reactions. With that in mind, intense research was developed over the past 30 years in order to modify NiTi surface to reduce or prevent Ni release. By altering surface composition or increasing the natural TiO_2 layer, a few authors had succeeded to perform this task, yet neglecting to consider the mechanical behavior of the newly developed surface. The alloy is used as a biomaterial mainly in applications that require severe strain, which could deteriorate the protective capacity of the modified layer. The problem is even more critical since NiTi is susceptible to stress induced corrosion.

Another usage for the NiTi shape memory alloys in dentistry is as endodontic instruments. Its greater flexibility, when compared with stainless steel files, reduces the chance of iatrogenic errors during root canal shaping and enabled NiTi endodontic files to be engine driven, which significantly reduced treatment time while producing a correct conic tapered profile, ideal to medicament delivery and to remove contaminated tissue. Nonetheless, NiTi endodontic instruments can sometimes fail by torsional overload or fatigue. Torsional overload will happen when the tip or some part of the file get stuck between root canal walls while the engine keep rotating the shaft causing plastic deformation followed by fracture.

Fatigue fracture of endodontic instruments can occur due to cyclic tensile/compressive loading arising during file rotation inside a curved canal. The complex root canal system can impose strains over 4% on the metallic tools during treatment (6% strain were already reported). The basic mechanism of rupture is the nucleation of microcracks at the material surface, followed by inward propagation of these cracks until the cross-sectional area reduction achieves a critical value in which the tensile stress becomes high enough to fracture the object. It is a common belief that the high concentration of surface defects generated during machining the instrument into its final shape is related to the failure process, these defects acting as crack nucleation sites. With this in mind, some manufacturers have employed treatments to produce a smoother surface, to avoid or retard the formation of these cracks. The instruments fatigue life can also be reduced by corrosion, since the mechanical action of the file during endodontic therapy is performed in the presence of highly corrosive irrigants such as NaClO solutions.

This work proposes to develop a procedure to coat NiTi shape memory alloys with a flexible TiO_2 protective layer with the goal of improving corrosion resistance and reducing the concentration of Ni at the material surface, in order to improve the alloy biocompatibility, even when it is severely strained and apply this route in an engineering practical case. The methodology was tested to coat NiTi strips and endodontic instruments (practical case). The resulting composite layer was tested regarding mechanic and corrosion performance.

2. Objectives

2.1. General objective

This work proposes to develop a route to coat NiTi shape memory alloys with a flexible TiO_2 protective layer to improve the metal corrosion resistance and biocompatibility, and apply the developed procedure in a practical case. For this last part, it was chosen to apply the oxide deposition on superelastic endodontics instruments.

2.2. Specific objectives

To complete the proposed objective above mentioned, a sequence of specific tasks needs to be completed:

- Adapt the dip-coating sol-gel route developed by Burgos and Langlet (1999a, 1999b) to coat superelastic NiTi strips with a thick and flexible TiO_2 layer.
- Optimize the thermal treatment post deposition to obtain maximum film flexibility and biocompatibility without affecting the mechanical properties of the substrate.
- Characterize the deposited film regarding mechanical properties (flexibility), phase composition and corrosion resistance.
- Use the deposition procedure to coat endodontic instruments and test their corrosion resistance and fatigue life.
- Develop a methodology to test cutting efficiency of the endodontic instruments and use it to compare coated and uncoated samples.

3. Literature review

3.1. Shape Memory Effect and Superelasticity

The shape memory effect (SME) was first observed by Arne Örlander in 1932 on an AuCd alloy, followed by observations on CuZn and CuSn (Greninger & Mooradin 1938). The explanation for the phenomenon, based on the thermoelastic behavior of a specific martensitic transformation, came later with Kurdjumov and Khandros in 1949 (Kurdjumov & Khandros 1949) and also with Chang and Read (Chang & Read 1951).

The one way shape memory effect (OW-SME) is well illustrated in Figure 3.1. The material is shaped at its high temperature, highly symmetric, austenitic phase (normally with a cubic lattice), in order to "print" the desired shape to be recorded. The object is then cooled passing through a martensitic phase transformation (MT). This is an adiffusional phase transformation involving cooperative small displacements of each atom through a shear process. This change does not occur in a definite temperature. Due to internal friction in the boundary between austenitic and martensitic phases, the transformation starts at a temperature denoted M_s and finishes at a lower temperature denoted M_f (Saburi 1998).

The martensitic product of the transformation has a less symmetric lattice (monoclinic, orthorhombic, trigonal, tetragonal, etc.) and can be produced with several energetically equivalent variants, forming laths of martensite which are rotations or specular images of each other. In order to minimize the distortion caused by the phase transformation and the total free energy of the product, the martensite will pass through a process known as self-accommodation, shown in Figure 3.2. Metals can self-accommodate in two different ways: through slip (Figure 3.2b) and through twinning (Figure 3.2c). Slip involves breaking of chemical bonds and introduction of dislocations in the lattice in an irreversible manner. Materials that accommodate strain through this method cannot present the shape memory effect. Twinning of martensite variants is the basic mechanism responsible for the SME. In this configuration, two different variants (or one variant and the austenitic phase) are separated by a coherent boundary. These twin boundaries have relatively low energies and high mobility. Since no bonds were broken and no dislocations were added to the lattice, the transformation is completely reversible through heating, defined as a thermoelastic transformation (Otsuka & Ren 2005).

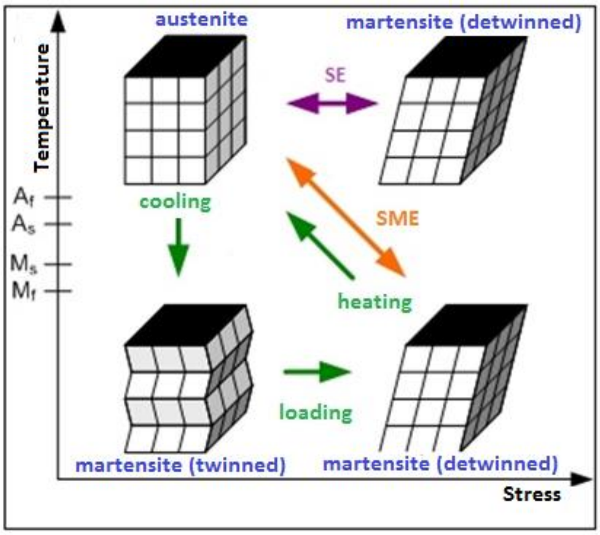

Figure 3.1 - Shape Memory Effect and Superelasticity (adapted from site: http://mb.uni-paderborn.de/)

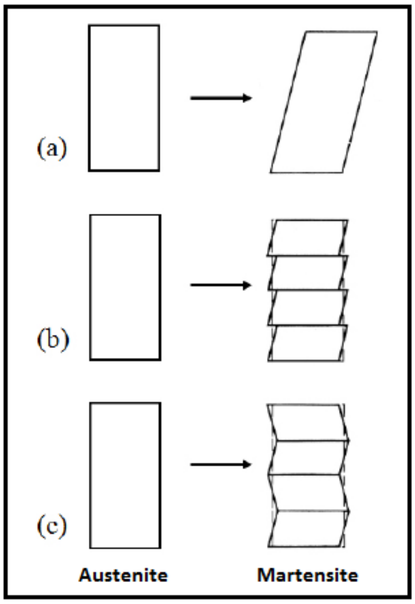

Figure 3.2 - Martensite self-accommodation mechanisms : a) shape change; b) slip; and c) twinning (adapted from Wayman & Duerig 1990)

The twinned structure of the material can now be easily strained through the application of stress. When loaded, the martensite variants which are well oriented in relation with the stress will grow. Twin boundaries will move until the entire object is constituted by a single martensite variant (right bottom side of Figure 3.1). If the stress ceases, this detwinned structure will be stable and the object will be deformed. Heating this object will start the reverse transformation into the austenitic state. This transformation is also affected by internal friction and starts and ends at temperatures denoted A_s and A_f. Being a highly symmetric phase, all the martensite variants will transform back to a single phase configuration, returning the material to its original shape (Otsuka & Waymann 1998).

The driving force for the martensitic transformation is a difference in vibrational entropy, which is lower for the martensite and it is favorable at lower temperatures. Another way of starting a MT from an austenitic state is applying stress. The martensite so formed is called stress-induced martensite (SIM) and is composed of a single variant oriented according to the stress direction. When the stress is removed and the temperature is above A_f, the martensite will be unstable and will transform back to austenite without any additional heating required (upper part of figure 3.1). This is the superelastic (SE) behavior of a shape memory material, also known as pseudoelasticity and it is a special case of the SME (Otsuka & Waymann 1998).

The critical stress required to induce martensite shows a linear behavior with temperature above M_s, as indicated in Figure 3.3. The higher the temperature, more unstable is the martensite and critical stress needed to form SIM increases. There is a limiting temperature in which martensite can be induced by stress (M_d). Above this value, the stress to form the less symmetrical phase is higher than the one that promote slip in the austenite and the SME cannot be explored.

The mechanical behavior of any shape memory alloy (SMA) is intrinsically linked with the temperature in which the object is being deformed (T_d). The three stress-strain plots on Figure 3.4 summarize the mechanical response of SMA to applied stress (or strain) on different temperature ranges.

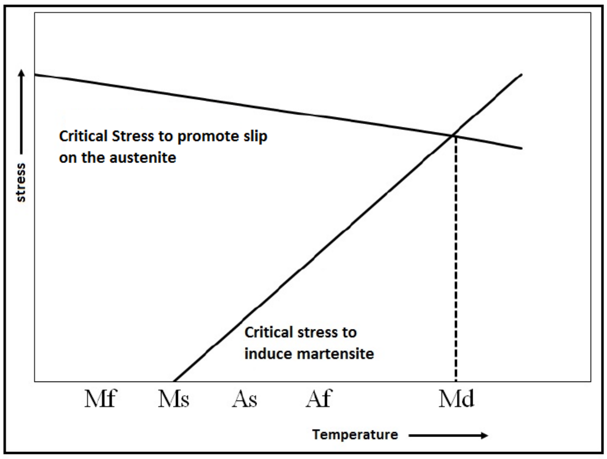

Figure 3.3 - Critical stress to induce martensite and to promote austenitic slip (adapted from Ostuka & Waymann 1998)

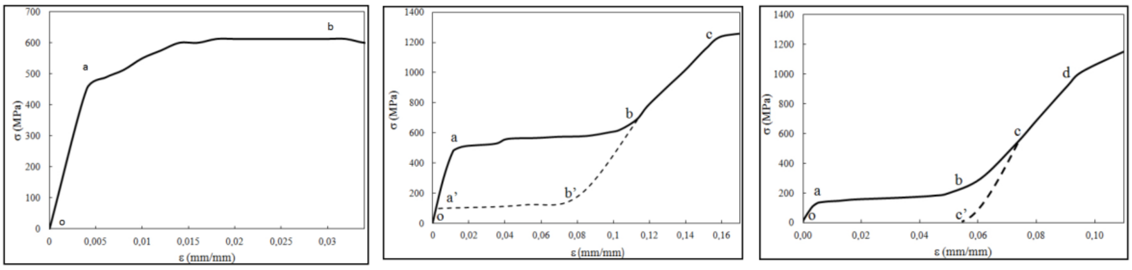

a)

b)

c)

Figure 3.4 - Stress x Strain curves for a hypothetical SMA with: a) $T_d > M_d$; b) $A_f < T_d < M_d$; c) $T_d < M_f$ (adapted from Santos 2013)

- $T_d > M_d$ (Figure 3.4a): The stress needed to induce martensite is higher than the stress to promote slip in the austenitic phase. The material will behave as a common metal exhibiting an elastic behavior of the austenite (oa) followed by its plastic deformation when dislocations are created and moved (ab).

- $A_f < T_d < M_d$ (Figure 3.4b): The material is initially austenitic. With applied load, austenite will start deforming elastically (oa) until the stress is high enough to induce martensite. At this point, the detwinned martensite will form and a large pseudoplastic deformation is achieved (ab). This deformation plateau (ab) emerge with very little or no variation in stress. If loading continues to grow after this deformation plateau, martensite will deform elastically and the last pockets of trapped austenite will transform in detwinned martensite (bc). Above point “c”, increasing stress will plastically deform the martensite in an irreversible way. If at any point between “o” and “c” the stress is removed, the stressed martensite will first relax (if elastically deformed) and become unstable. At a lower value of stress (lower than the one needed to induce SIM) the martensite will transform back to austenite and all the pseudoplastic strain will be recovered (dotted line). This shows the SE behavior of a shape memory material.
- $T_d < M_f$ (Figure 3.4c): The material is in its martensitic state. With increasing applied stress, the martensite will first deform elastically (oa) until stress is high enough to move the twin boundaries. At this point, a plateau of pseudoplastic deformation is formed at an almost constant stress (ab). Increasing the load will make the detwinned martensite to continue its elastic deformation followed by a plastic one, and the last pockets of retained austenites will transform in SIM. If stress is removed before plastic deformation, the elastic component of the martensite will be retrieved, but a large amount of strain caused by the detwinning will remain (oc’). This pseudoplastic deformation can be restored through heating above A_f. This is the behavior of the SME. A very similar mechanical behavior with a few modifications can also be observed if $T_d < A_s$.

If the SMA is stressed at an intermediate temperature between M_f and A_f, a mixture of both SME and SE will occur.

3.2. NiTi Shape Memory Alloys

Shape Memory effect on near equiatomic NiTi alloys were first observed by Willian Buehler in 1959, but only in 1962, he and Frederick Wang showed its potential for commercial applications (Kauffman & Mayo 1997). At first, the NiTi alloy competed against Fe and Cu based SMAs, but its unique properties allied with the highest recoverable strain by the time, made this metal dominate the market and research fields (Duerig *et al.* 1990, Humbeeck 1999).

The first successful commercial application of NiTi was a “shrink-to-fit” connection used to join Ti hydraulic pipes on F-14 combat aircrafts produced by Grumman Aerospace. A few years after, this material was used on its first bioapplication by George B. Andreasen in orthodontic arch wires (Andreasen *et al.* 1971, Kauffman & Mayo 1997).

Since then, several studies were performed enabling the use of NiTi alloys in many fields of application (Jani *et al.* 2014). The metal can be “programmed” to present SME or SE at room temperature with a retrievable strain of up to 8%. The relatively high recoverable strain allied with a small temperature hysteresis made NiTi alloys ideal to act as actuators, replacing electromagnetic motors or hydraulic or pneumatic triggers (Humbeeck 1999, Kohl 2010, Sun *et al.* 2012). The mobility of the twin boundaries makes NiTi an excellent damping material to be used as protection from seismic vibrations in civil engineering (Qian *et al.* 2010). Automobile and aerospace industries also make use of these smart materials in the production of its vehicles (Humbeeck 1999, Leo *et al.* 1998, Hartl & Lagoudas 2007).

NiTi is also chemically stable. For that, and its SME, this material has been used for a wide range of bioapplications, mostly as components of minimal invasive surgeries

(Shabalovskaya *et al.* 2008). Biocompatibility of SE NiTi alloys will be discussed in more detail latter in this chapter.

3.2.1. NiTi physical metallurgy and its shape memory alloy

Equilibrium phase diagram for NiTi alloy was controversial for several years (Otsuka & Ren 2005) until a consensus has arrived. The diagram accepted today is the one proposed by Massalki *et al.* (1990) and it is shown in Figure 3.5. The alloy compositions presenting the SME with a high recoverable strain are the ones close to the equiatomic proportion. This phase is marked in the diagram as TiNi, and is delimited by the Ti_2Ni intermetallic component at the Ti rich side and by $TiNi_3$ on the Ni rich side. The solvus line virtually superpose each other for temperatures under 650ºC, but it is accepted that, at low temperatures, this phase admits a Ni content from 50.0 to 50.5 at.% (Saburi 1998).

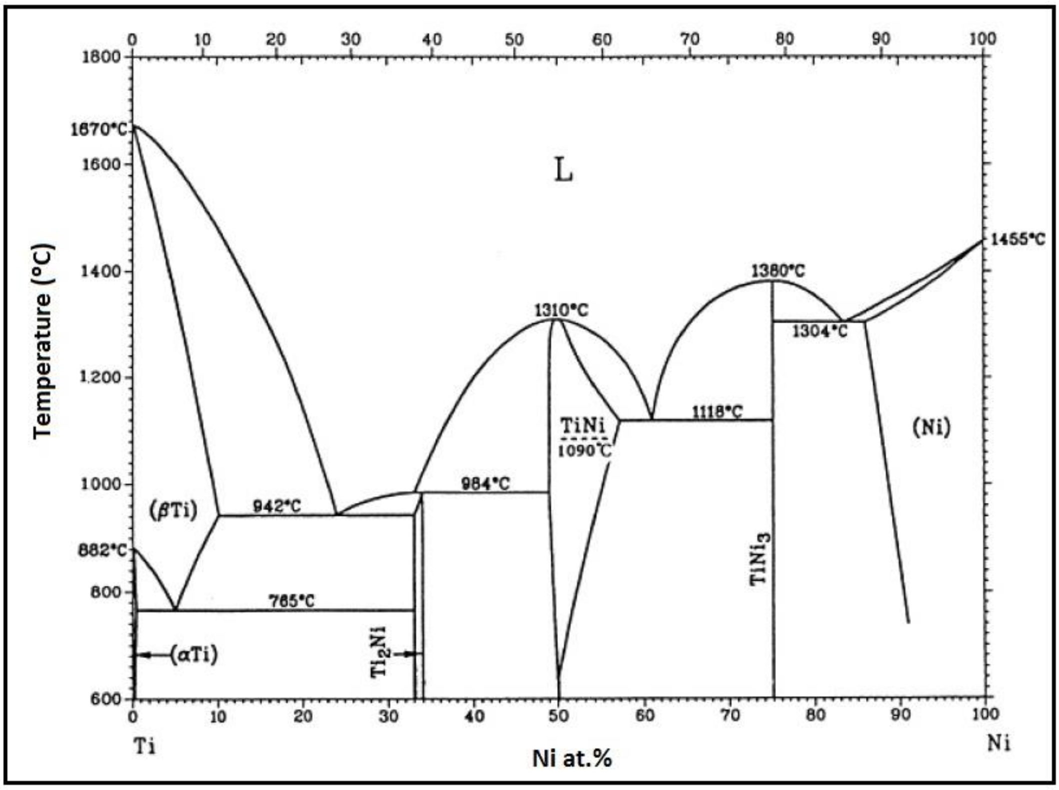

Figure 3.5 - Phase diagram for NiTi alloy (adapted from Massalki at al. 1990)

The equilibrium phase of NiTi at high temperatures has an ordered body central cubic lattice showed in Figure 3.6a, named B2. When quenched, NiTi will pass through a martensitic transformation to an ordered monoclinic phase denoted B19’ (Figure 3.6b). The reaction B2 → B19’ can occur in three different manners depending on alloy composition and thermomechanical treatment (Otsuka & Ren 2005):

B2 → B19’

B2 → R → B19’

B2 → B19 → B19’

The first reaction will happen with fully recrystallized samples. The deformation plateau on the stress x strain curves for this kind of samples is small, with a low recoverable strain. NiTi objects fully recrystallized are soft, and some local plastic deformation may occur during the large strains imposed on SMA materials, reducing the amount of retrievable strain (Otsuka & Ren 2005).

The reaction passing through the B19 orthorhombic phase may occur for ternary alloys of Ti-Ni-Cu, with the copper acting as a substitutional element for the Ni on the NiTi alloy (Otsuka & Ren, 2005).

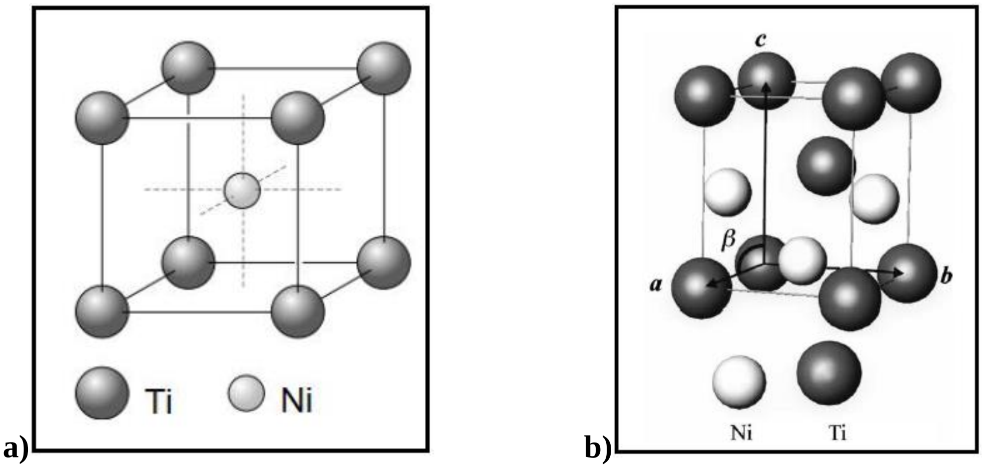

Figure 3.6 - Unit cell for NiTi equiatomic alloy: a) B2 ordered body centered cubic cell; b) B19’ ordered monoclinic cell (adapted from Otsuka & Ren 2005)

The R phase, which has a trigonal structure, will appear as an intermediate step when internal stress is caused by the presence of dislocations, inclusions or precipitates in the NiTi matrix, and also when a ternary alloy is composed with Fe or Al (Stroz 2002). The transformation B2 → R is a martensitic transformation with a very small temperature hysteresis ($\Delta T \sim 1.5$ºC) with a low recoverable strain (around 0.94%). This phase is very important on the thermomechanical processing of SME and SE NiTi alloys. The lattice characteristics of the three main phases involved in the SME of NiTi alloys are presented in Table III.1 (Otsuka & Ren 2005).

This table shows the maximum recoverable strain for the NiTi system as 10.7% in single crystals on a specific direction of applied stress. However, single crystals are fragile materials and the SME rapidly deteriorates with repeated deformations. Polycrystalline NiTi can be treated to obtain 8% recoverable strain. In order to get a large deformation plateau with a high recoverable deformation for SME and SE in NiTi alloys, the recrystallized samples pass through a thermomechanical processing, involving cold work followed by recovery at intermediate temperatures (~500 ºC). The cold work will introduce dislocations that will harden the NiTi matrix, preventing plastic deformation to appear when deformed. These dislocations also hinder twin boundary movement, so the recuperation treatment is required to remove some dislocations and arranging the remaining ones on a substructure leaving large spaces for the boundaries to move. The introduced dislocations will generate stress fields on the NiTi matrix responsible for stabilizing the martensite and inducing the appearance of the R phase (Saburi 1998).

NiTi alloys with less than 50.5 at.% Ni are immune to aging. Alloys richer in Ni will decompose in a mixture of TiNi and $TiNi_3$ if slowly cooled from high temperatures. This phase transformation can also have intermediate steps depending on the temperatures used during the cooling, as indicated in the TTT diagram of Figure 3.7.

Table III-1– Lattice characteristics of the main phases involved in NiTi SMA (adapted from Otsuka & Ren 2005).

Phase	**B2**	**R**	**B19’**	**Ti_3Ni_4**	**$TiNi_3$**
Structure	Ordered bcc	Trigonal	Monoclinic	Rhombohedral	Hexagonal
Lattice parameters	a = 0.3015nm	(hexagonal lattice) a_R = 0.738*nm c_R = 0.532*nm	a = 0.2889*nm b = 0.4120*nm c = 0.4622*nm β = 96.8 º	a = 0.670nm α = 113.8º	a = 0.5101nm c = 0.8307nm
Recoverable strain	-	0.94% strain on [111] B2 phase direction	10.7% strain on [233] B2 phase direction	-	-

*- Values dependent on Ni content. The values listed are for a Ni-52 at.%Ti alloy.

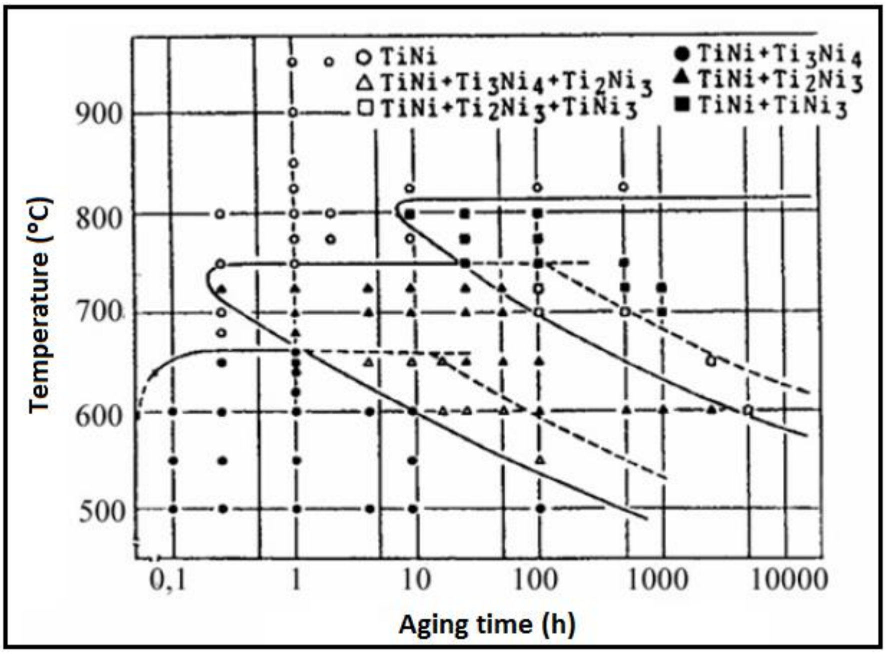

Figure 3.7 - TTT diagram for Ti-52Ni alloy (adapted from Otsuka & Ren 2005)

For temperatures under 680ºC, the decomposition of supersaturated NiTi alloys in $TiNi_3$ will pass first to the transformation into the metastable phase Ti_3Ni_4. This rhombohedral phase is formed by heterogeneous nucleation and growth on grain boundaries, inclusion boundaries or next to oxide particles, such as Ti_4Ni_2O, normally formed during casting and thermomechanical processing of the alloy (Schmahl *et al.* 2004). At the first stages of growth, the Ti_3Ni_4 particles will have a lenticular shape, a few dozen nanometers in size and will be coherent with the NiTi matrix. The control of the amount and size of these particles is fundamental for the engineers to choose the specific SME properties desired for the metal.

The coherent Ti_3Ni_4 particles will generate a stress field in the NiTi matrix, stabilizing the martensite. This would increase M_s and M_f temperatures and induce the formation of the R phase during cooling. Another effect of the precipitation of these particles is to reduce the Ni content in the matrix. The martensitic transformation temperatures are highly Ni dependent for concentrations above 50 at.%, as shown in Figure 3.8. This reduction in the amount of Ni in the matrix increases the martensitic transformation temperatures. Using the aging treatment, the engineer can control the transformation temperatures and choose between SME or SE for his alloy at its work temperature.

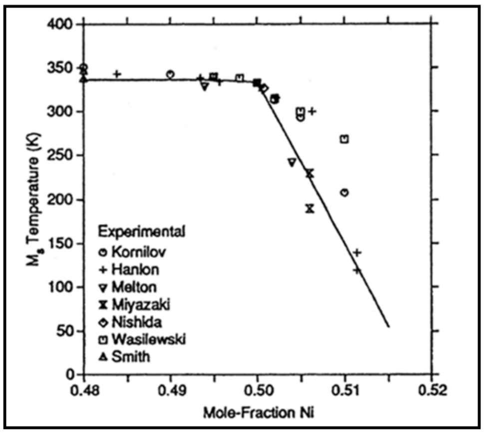

Figure 3.8 - M_s temperature dependence on Ni concentration for NiTi SMAs (source: Otsuka & Ren 2005)

The other metastable phase (Ti_2Ni_3) and the $TiNi_3$ are incoherent with the matrix, generating small stress fields. The major effect of those two phases is also to reduce the Ni content of the NiTi matrix.

Table III-2– Physical and mechanical properties of NiTi alloy (adapted from Bahia 2004)

Physical properties	
Melting point	1300ºC
Density	6.45 g/cm^3
Thermal conductivity (B2)	0.18 W/cmºC
Thermal conductivity (B19')	0.086 W/ cmºC
Thermal expansion coefficient (B2)	11.0 x 10^{-6} /ºC
Thermal expansion coefficient (B19')	6.6 x 10^{-6} / ºC
Specific Heat	0.20 cal/gºC
Corrosion resistance	Excellent
Mechanical properties	
Young's modulus (B2)	≅83 Gpa
Young's modulus (B19')	≅ 28 a 41 Gpa
Yield strength (B2)	≅ 195 a 690 Mpa
Yield strength (B19')	≅ 70 a 140 Mpa
Poisson's ratio	≅ 0.3
Strain to fracture (annealed)	≅ 25 – 50 %
Strain to fracture (harden)	≅ 5 – 10 %
Hot formability	Very good
Cold Formability	Hard (fast hardening)
Machinability	Hard
Weldability	Hard

3.2.2. NiTi biocompatibility

During the first years of development of NiTi shape memory alloys, the use of the metal as a biomaterial was considered unsafe, due to the high Ni concentration (normally more than 50 at.% for SMA). Nickel is an essential trace element in human body, participating on the process of protein synthesis. However, concentrations of Ni above a threshold value (still undefined) can cause carcinogenic and allergenic reactions (Berger-Gorbet *et al.* 1996, Es-Souni *et al.* 2005). Still, the high bonding energy on NiTi bulk ordered lattice and a natural passive external TiO_2 layer make the alloy to exhibit an excellent biocompatibility. First use on the metal as a biomaterial was reported in 1971 by Andereasen (Andreasen *et al.* 1971) using the material in orthodontic arch wires. In 1989, the US Food and Drug Administrations (FDA) approved the use of NiTi as an orthopedic implant material. The mechanical behavior of the superelastic alloy is closer to the bone, when compared to stainless steel (Figure 3.9), making NiTi an excellent choice for orthopedic implants. After this first use, the high biocompatibility, allied with its differential mechanical properties, made NiTi shape memory alloys the material of choice for the manufacture of numerous utensils used in several areas of medicine and dentistry (Figure 3.10; Jani *et al.* 2015).

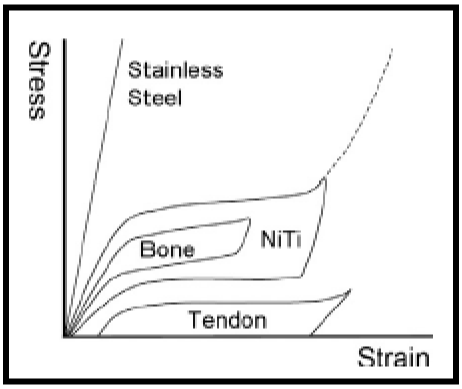

Figure 3.9 - Comparative stress x strain curves for bone, tendon, NiTi and stainless steel (adapted from Morgan 2004)

NiTi biocompatibility is deeply connected to its natural oxide surface layer. Difference in formation enthalpy for Ti and Ni oxides generate a preferential oxidation of titanium. The main oxide formed on the alloy surface is the TiO_2. This ceramic coating is chemically stable and presents a high biocompatibility and biofunctionality which will be explained in more detail in section 3.3.2. Small quantities of other Ti oxides (Ti_2O_3) and Ni oxides (NiO, $Ni(OH)_2$), as well as metallic Ni are found on the surface of the metal (Wever 1998).

The main concern about NiTi biocompatibility is the release of Ni ions in the blood stream caused by alloy corrosion from the body fluids. With this in mind, several studies have been conducted over the last 30 years in order to modify the alloy surface, reducing Ni concentration to prevent its release (Shabalovskaya *et al.* 2008). These studies focused mainly on comparing bare surface and modified alloy corrosion resistance on simulated body fluids (Hank's solution, Kokubo Simulated Body Fluid, Tyrode's solution, artificial saliva, etc).

Bare NiTi surface present high breakdown potentials and low corrosion current densities on potentiodynamic tests on several saline solutions, showing a natural high corrosion resistance for the alloy, mainly when compared with stainless steel and Co-Cr-Mo-based medical alloys (Es-Souni *et al.* 2005). However, its repassivation capability is considered lower than that of pure Ti, but equivalent of those of stainless steel (Shabalovskaya *et al.* 2008). Mechanical polishing (Mp) would reduce surface roughness decreasing exposed area to the corrosive fluids. The problem with this technique is that it also removes the natural protective TiO_2 layer and can encrust inclusions on the surface, resulting in a lower corrosion resistance (moreover, it has a low reproducibility; Shabalovskaya *et al.* 2004).

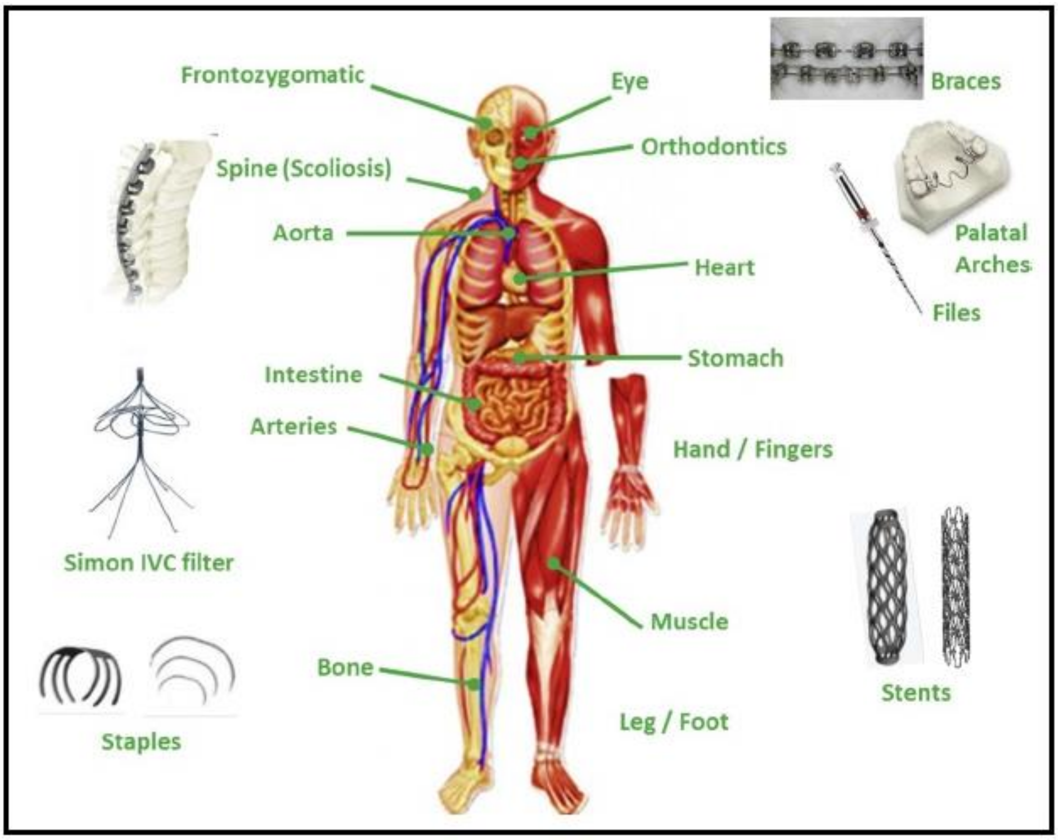

Figure 3.10 - Main applications of NiTi shape memory alloys in medicine and dentistry (source: Jani *et al.* 2015)

Other techniques to treat bare surfaces as electropolishing (Ep), chemical etching (Ce, HF + HNO_3) and anodizing (An) were attempted (Fushimi *et al.* 2006, Heβing *et al*. 2007, Shi *et al.* 2007). These procedures also remove the oxide layer reducing the metal corrosion resistance, but allied with some other method for reconstruction of the TiO_2 film can generate good results. Boiling in water (Wb) is an easy process to recreate the passive layer with the titania in its amorphous state with a thickness of approximately 20 nm (Wever 1998). The combined techniques (Mp or Ep or Ce or An + Wb) will produce a smooth protected surface with improved corrosion resistance. Heat treatments (Ht) on air can crystallize and increase the oxide layer. Crystalline TiO_2 have biological advantages (discussed later) but, depending on the temperatures used on the Ht, energy can be enough to activate Ni diffusion from the Ni rich sub-layer (positioned right under the Ti rich oxide film) to the surface, defeating the main purpose of eliminating Ni release (Shabalovskaya *et al.* 2008).

Modification of the surface was also attempted with ion implantation through plasma immersion treatment or ion sputtering. Systematic studies with O, C, N, Ar, Cu, Zn, Zr, C_2H_2 implantation and electron beam modification were performed (Shevchenko *et al.* 2004, Lotkov *et al.* 2005, Poon *et al.* 2005, Yeung *et al.* 2005, Cheng & Zheng 2006, Maitz & Shevchenko 2006). With the correct deposition parameters, it is possible to completely deplete the presence of Ni on the composite surface, at the same time improving the SMA corrosion resistance. The main disadvantages of the methods are the fragility of the formed layer (cracking with low strains) and changes in the alloy mechanical behavior. The energy used to implant ions is high enough to induce changes in the bulk structure, destroying the symmetry of the top NiTi layers, modifying its hardness and transformation temperatures, consequently its shape memory effect.

A potential problem regarding the Ni release is the susceptibility of NiTi to suffer stress induced corrosion. Under stress, breakdown potentials for pitting corrosion initiation became reduced, and current densities increased, as showed in the works of Chan *et al.* (2012), who tested the susceptibility to stress corrosion on laser welded NiTi immerged in Hank’s solution. Liu *et al.* (2014) showed the same effect on NiTi orthodontic arch wires in saliva. Treatments to improve corrosion resistance should endure the high strains imposed upon NiTi used inside the human body. Normal using conditions of NiTi alloys as a biomaterial imposes strains of 3-4%, but in some extreme cases, this deformation can reach the recoverable limit of 8% (Shabalovskaya *et al.* 2002). Ionic implantation protection quickly deteriorates with strain, the film cracking with deformations as low as 1%. Treatments on the bare surface (Mp, Ep, Ce, An + Wb + Ht) can generate a thin film that sustain some deformation (3-4%). In the case of TiO_2 reconstruction with just Wb treatment on a smooth surface, the thin film can sometimes keep its protective characteristic through strains of 6-8% (Shabalovskaya *et al.* 2008), but presenting a thin film that could leave a relatively high surface Ni concentration.

Another parameter regarding NiTi biocompatibility is its surface cytotoxicity. More details about cellular response of NiTi surface will be described in section 3.3.2.

3.2.3. NiTi endodontic instruments

Endodontics is the dentistry branch that works with diagnosis and treatment of infections in the dental pulp (Figure 3.11a, Santos 2013). Endodontic therapy is based on the complete removal of this dental pulp together with all contaminated tissue from the root canal. The canal preparation determines the efficacy of all subsequent procedures and includes mechanical debridement, creation of space for medicament delivery, and optimized canal geometries for adequate obturation (Peters 2004). This preparation and disinfection is accomplished by mechanical action of a rotatory endodontic instrument also known as endodontic file (Figure 3.11b), allied with the chemical action of a lubricant solution, normally sodium hypochlorite (NaClO), which also acts as bactericide and organic tissue solvent (Haapasalo *et al.* 2010).

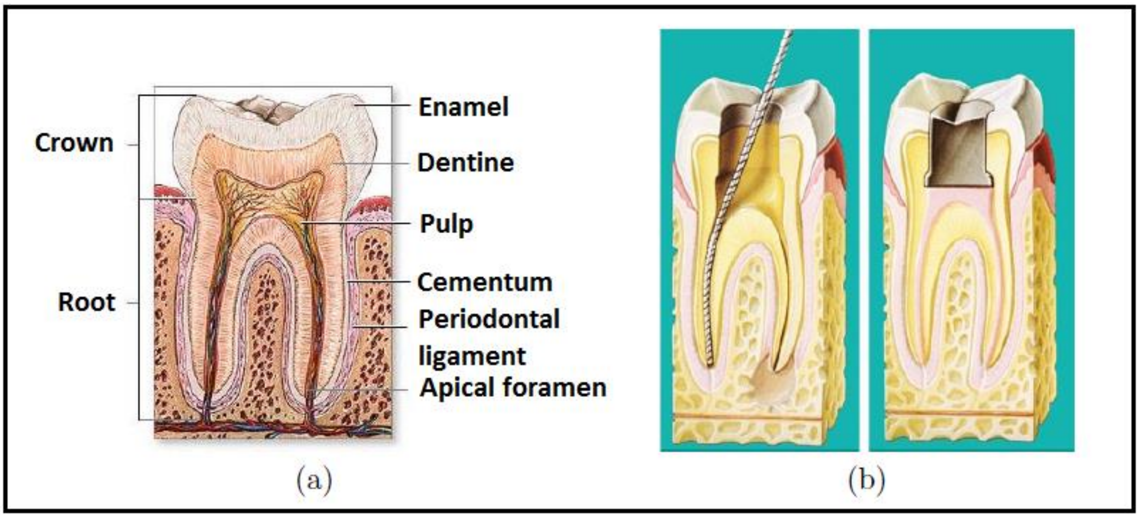

Figure 3.11 - a) Root canal anatomy; b) Main steps of endodontic therapy showing mechanical action of a endodontic instrument (left) and posterior obturation (right); (Adapted from Santos 2013)

The root canal system can assume a very complex geometry, presenting curved shapes, mainly in molars (Bahia 2004), that difficult the mechanical action of the endodontic files. Thus, NiTi shape memory alloys are an excellent choice of material to manufacture instruments capable of adjusting to this complex geometry and performing the canal preparation. Since the 80's, NiTi files (Figure 3.12) have been replacing stainless steel instruments due to their superior properties (Table III.3). NiTi lower Young's modulus reduces the possibility of iatrogenic mistakes during treatment, and it presents a high fatigue resistance, which decreases the chance of internal instrument fracture (Thompson, 2000, Peters 2007, Haapasalo *et al.* 2010). Its mechanical properties allowed the design of new blade geometries, alternative caliber and taper systems and enabled the introduction of engine driven rotary movement, facilitating a fast and efficient conical-tapered shaping of the root canal (Bahia 20014, Peixoto 2013, Santos 2013).

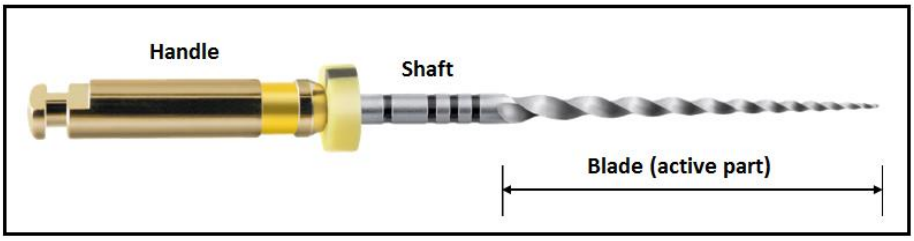

Figure 3.12 - Typical NiTi endodontic instrument and its basic components

Table III-3– Comparative properties between near equiatomic NiTi and austenitic stainless steel (adapted from Russel, 1998).

Properties	**NiTi**	**Stainless Steel**
Recoverable strain	8.0%	0.8%
Biocompatibility	Excelent	Good
Young's modulus	43 GPa (martensite) 83 GPa (austenite)	193 GPa
Density	6.45 g/cm3	8.03 g/cm3
Magnetic	No	Yes
Ultimate tensile stress	1240 Mpa	760 MPa

Despite of its great advantages when compared with stainless steel files, NiTi endodontic instruments can eventually fracture during procedure. Fracture of endodontic files during the shaping of a curved root canal is one of the main concerns among practitioners. The failure of the instrument can sometimes prevent the correct chemo-mechanical preparation and total disinfection of the root canal (Parashos & Messer 2004). Rotary NiTi files can fail by two mechanisms: excessive torque and flexural fatigue (Plotino *et al.* 2013, Montalvão *et al.* 2014, Santos *et al.* 2014).

Torsional overload will happen when the instrument tip or other part gets stuck inside the root canal while the engine keeps spinning the shaft. Depending on the torque applied by the motor, the yield strength can be surpassed, leading to plastic deformation followed by the instrument rupture. Modern endodontic engines are equipped with torque limiters which, allied with the control of the apical force applied by the practitioner, can help to prevent this type of failure (Peixoto 2013; Santos 2013).

Fatigue fracture may occur when the material is subjected to cyclic tensile/compressive loading, as it is the case when the instrument is rotating inside a curved canal. The basic mechanism of the rupture is the nucleation of microcracks on the material surface, followed by the inward propagation of these cracks until the cross-sectional area reduction achieves a critical value at which the tensile stress becomes high enough to fracture the instrument (Bahia *et al.* 2006). NiTi endodontic instruments are susceptible to this kind of failure, mostly with instruments of greater caliber. The high deformation imposed to the files in curved canals (~4 %, Martins *et al.* 2006, Vieira *et al.* 2008) quickly initiate cracks on the surface. Since this crack initiation is hardly avoided, actions must be taken in the instrument project to reduce its propagation speed.

Fatigue fracture can also be assisted by corrosion. Corrosion of NiTi endodontic instrument in NaClO had been studied by several authors (Busslinger *et al.* 1998, O’Hoy *et al.* 2003, Darabara *et al.* 2004, Berutti *et al.* 2006, Martins *et al.* 2006, Nóvoa *et al.* 2007). Sodium hypochlorite is the main irrigant used for root canal treatment, due to its excellent properties as lubricant, bactericide, organic tissue solvent (Zehnder 2006) and also because it is less corrosive then R-EDTA (ethylenediamine tetraacetic acid, Darabara *et al.* 2004). The main conclusion of those previous studies was a high pitting and crevice corrosion resistance of the NiTi instruments within the short period of time in which the file is exposed to the solution during treatment. Some galvanic corrosion may occur if the instrument is completely submerged in the NaClO solution (Berutti*et al.* 2006, Nóvoa *et al.* 2007). However, long term exposure can occur. Martins *et al.* (2006) showed that normal cleaning procedures after instrument usage are sometimes not enough to completely remove the NaClO from the file surface, in a way that eventually it can be stored contaminated by the solution.

Another concern is the fact that instruments can suffer stress-induced corrosion during instrumentation. Yokoyama *et al.* (2004) tested stressed NiTi wires in solutions with different concentrations of NaClO and showed that when the stress is enough to induce martensitic transformation, the corrosion resistance is reduced. A similar result was published by Chan *et al.* (2012) for laser welded NiTi wires submerged in Hank salt solution. Liu *et al*. (2014) tested stressed NiTi arch wires immerged in artificial saliva. Their results also endorse the susceptibility of the alloy to stress corrosion.

Another important feature to be considered for a better design of the endodontic instruments is regarding an important mechanical property: cutting efficiency. No standardized method for measuring this parameter has been reported in the literature. Several authors created different methodologies to perform this task (Felt *et al.*1982, Yguel-Henry & Stebut 1994, Haïkel *et al.* 1996, Silva 2004, Schäfer & Oitzinger 2008). Independent of the method employed for measuring the cutting efficiency, there is a strong relation between blade geometry and cutting capacity (Peixoto 2013). In this work, a new methodology for measuring cutting efficiency based on the total energy spent to shape an artificial, standardized root canal maintaining constant rotation and apical speeds will be presented. More details about this technique will be discussed in the next chapter.

3.3. Titanium dioxide

Titanium dioxide was first largely used as a substitute for lead based pigments on white paint. After Fujishima and Honda established (1972) that a TiO_2 electrode illuminated by UV light caused water hydrolysis, intense research was initiated and several new applications for the ceramic material were developed. Nowadays, TiO_2 is still used as a white pigment for ink, paper and plastics, but it is also used in toothpastes, sun blockers, cosmetics, anti-fog glasses, solar panels, biomedical implants and numerous other devices.

The oxide can be obtained in the form of powders, crystals or films through different techniques, like magnetron sputtering, spray pyrolysis, pulsed laser deposition, chemical vapor deposition, oxidation of a substrate, precipitation, sol-gel, among others (Carp *et al.* 2004).

3.3.1 TiO_2 structure and properties

Titanium dioxide (titania) can be found in nature in four different crystalline configurations: anatase (tetragonal), rutile (tetragonal), brookite (orthorhombic) and TiO_2 (B) (monoclinic). The two most common phases, anatase and rutile, are illustrated in Figure 3.13 and their main properties are listed in table III.4.

Thermodynamic calculations showed rutile as the most stable structure at normal pressures and temperatures. The small differences in Gibbs free energy for rutile, anatase and brookite (4 – 20 KJ/mol) make the last two phases virtually stable at room temperature. Also, in the polycrystalline form, the increase in energy caused by grain boundaries is enough to influence stability, in a way that anatase become the most stable phase for materials with grain size d < 10 nm, followed by brookite (10 < d < 35 nm) and rutile (d > 35 nm; Carp 2004). Rutile TiO_2 is a material with one of the highest refractive index for visible light. Rutile films are used as anti-reflective layer on solar panels. Anatase to rutile phase transition happens by nucleation and growth normally at high temperatures (above 600ºC). But the transformation is strongly affected by several factors, such as pressure, dopants, concentration of lattice and surface defects and substrate influence. Transitions at lower temperatures (under 200 ºC) have been reported (Mondal *et al.* 2015).

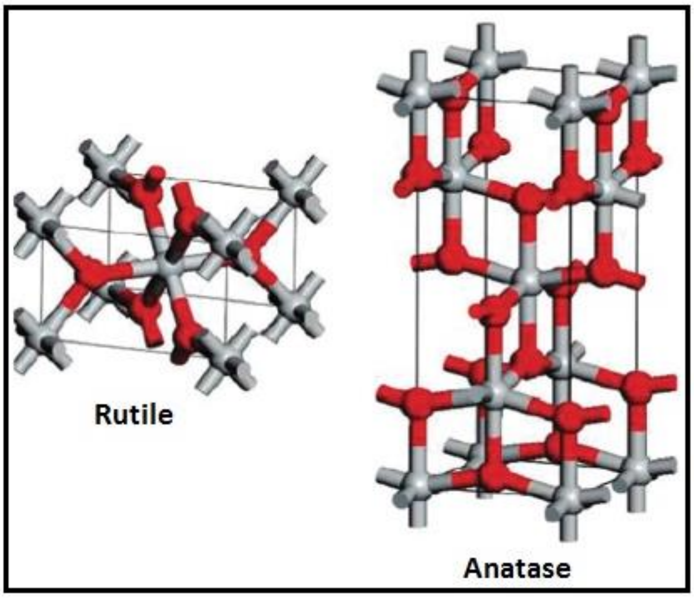

Figure 3.13 – Crystal structure of TiO_2 rutile and anatase showing each Ti atom (gray) surrounded by 6 oxygen atoms (red; adapted from Yin *et al.* 2013)

Titanium dioxide is a semi-conductor material presenting a strong photocatalytic activity and superhydrophilicity. These important features of this ceramic material are stronger in the anatase phase, due to higher electron mobility. When struck by UV light ($\lambda < 380$ nm for anatase and $\lambda < 410$ nm for rutile), electrons will be excited to the conduction band leaving a hole in the valence band (Figure 3.14). On conducting materials, the electron-hole pair is almost instantly recombined, but in semi-conductors this pair can migrate to the surface and act as oxidizing (hole) and reducing (electron) agents.

Table III-4– TiO_2 anatase and rutile properties (adapted from Carp *et al.* 2004).

Properties	**Anatase**	**Rutile**
Crystal structure	Tetragonal	Tetragonal
Lattice parameters	a = b = 0.3733nm c = 0.937nm	a = b = 0.4584nm c = 0.2953nm
Density	3.83g/cm^3	4.24g/cm^3
Band gap	3.26eV	3.05eV
Refractive index	2.5688	2.9467

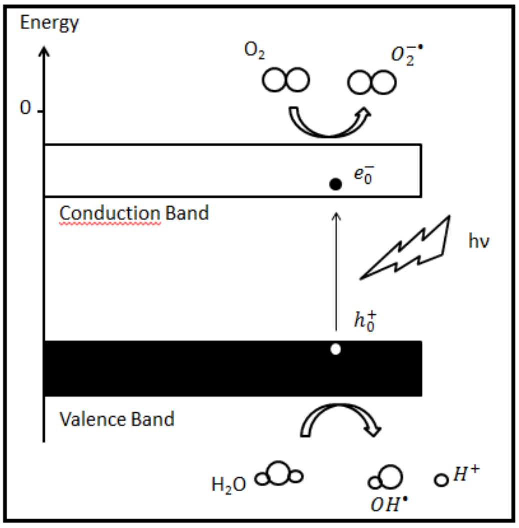

Figure 3.14 – Photocatalytic effect on TiO_2 scheme

In the presence of water and oxygen, the electron and holes on the titania surface will react generating the radicals $OH^{\bullet}$ and $O_2^{-\bullet}$. These radicals are strongly oxidizing agents, and will decompose organic and some inorganic matter. For this reason, TiO_2 anatase films are widely used as agents for water and air purification (Leong *et al.* 2014). The main reactions involved in the photocatalytic behavior of TiO_2 are the following:

$$TiO_2 + h\nu \rightarrow e_0^- + h_0^+$$

$$O_2 + e_0^- \rightarrow O_2^{-\bullet}$$

$$H_2O + h_0^+ \rightarrow H^+ + OH^\bullet$$

When illuminated by UV radiation, TiO_2 also exhibits the superhydrophilic behavior. This water affinity is caused by a structural modification on the surface. Under UV light, some electrons of the conducting band will reduce the Ti^{4+} to Ti^{3+}, while holes can be trapped in the lattice, weakening the bonds of O and Ti. This will generate oxygen vacancies on the surface. These vacancies will be occupied by the oxygen from water molecules (Figure 3.15; Houmard 2009).

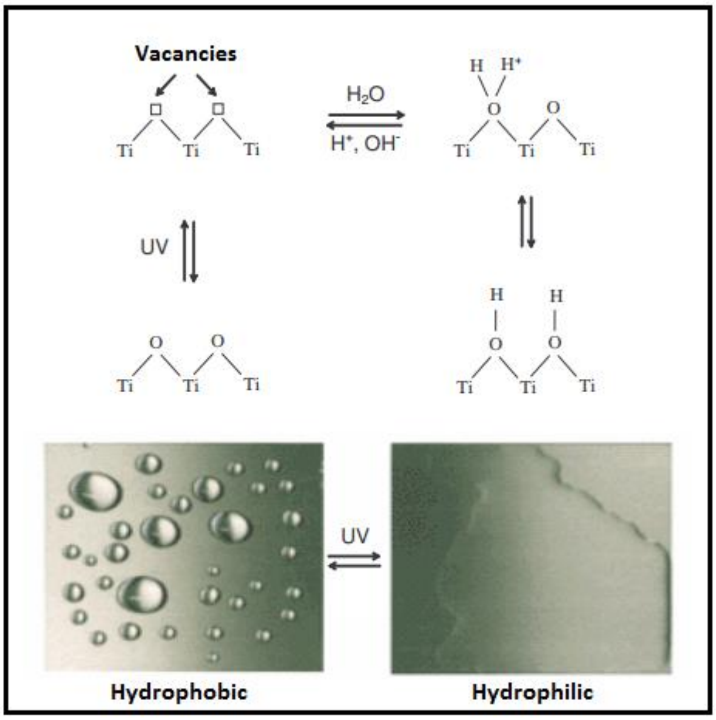

Figure 3.15 - Superhydrophilic behavior of TiO_2 (adapted from Houmard 2009)

The TiO_2 superhydrophilicity is used to generate anti-fog surfaces. The film, when illuminated by the sun (for instance) will prevent the accumulation of water droplets (Figure 3.16). This property, allied with the photocatalytic effect of degrading organic matter, make objects coated with TiO_2 self-cleaning. Titania coated surfaces illuminated by UV light will decompose organic (and some inorganic) matter and a simple water rinsing would remove the reaction products.

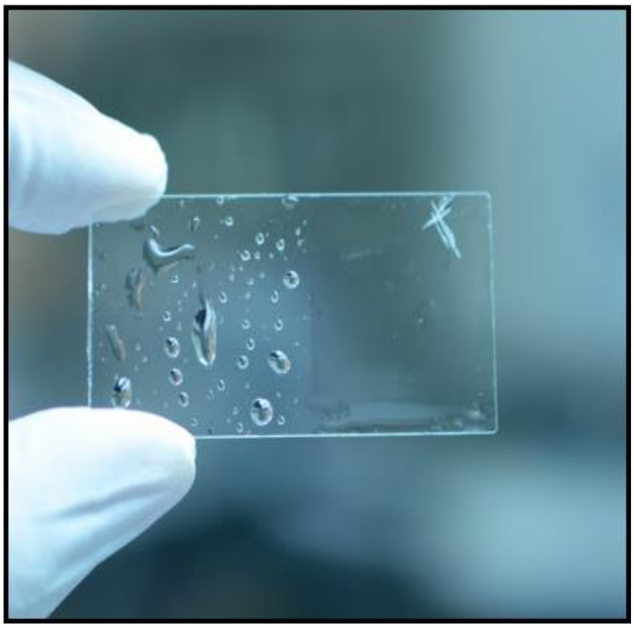

Figure 3.16 - Anti-fog TiO_2 coating deposited on the right part of the glass (Source: https://www.ipi-singapore.org)

3.3.2 TiO_2 film biocompatibility

As mentioned in section 3.2.2, NiTi biocompatibility is directly related to the natural TiO_2 layer formed on its surface. The highly stable titanium dioxide formed on the alloy surface act as a protective passivating barrier, preventing the corrosion of the bulk alloy and consequently the release of Ni.

Under normal conditions, TiO_2 is highly stable and will not react with other materials, making the alloy inert. Besides being biocompatible (not triggering any negative reaction as an allergy or cytotoxicity), the TiO_2 can act as a biofunctional material. The cellular response to the presence of the oxide was extensively studied. This factor was tested through adhesion and proliferation of several kinds of human and animal cells.

Shabalovskaya *et al.* (2008) reported results with different kinds of cells and techniques for the specific case of NiTi (with its TiO_2 top layer). The main conclusion of all the studies is a close relation between surface morphology and chemistry with cellular adhesion and proliferation.

Titania coatings can be “programmed” to have a high or low thrombogenic potential (formation of clots). This is very useful to design biofunctional surfaces for specific applications. Clotting mechanism on an implant surface will occur following a logic sequence. First, the negatively charged TiO_2 surface will attract a “positively charged” protein, as the fibrinogen (with a quadrupolar internal charge distribution). These proteins will attract and activate the negatively charged platelets (Figure 3.17). The platelets will spread forming a lattice and liberate cytokines that will attract specific kind of cells (for instance osteoblasts) to form the new tissue (Kulkarni *et al* 2015).

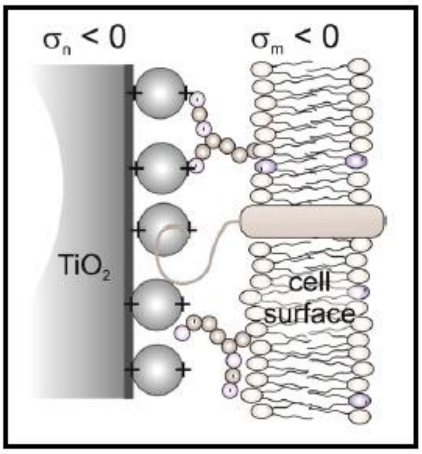

Figure 3.17– Cell attraction mechanism of negatively charged TiO_2 surface (adapted from Kulkarni *et al*. 2015)

Film crystallinity and roughness can influence the attraction of proteins, controlling the thrombogenic potential of the implant. Figure 3.18 shows the variation of concentration of fibrinogen adsorbed as a function of thermal treatment and surface composition. It is clear from the results of the samples chemically etched (Ce – used to remove the natural

TiO_2 film), CeWb (reconstituted amorphous film) and CeWbHt (crystalline film), and also Mp600 and Mp (used to reduce surface roughness and to remove the natural oxide layer) that the higher crystallinity of the TiO_2 film increases adsorption of the protein and the surface thrombogenic potential (Shabalovskaya *et al.* 2008).

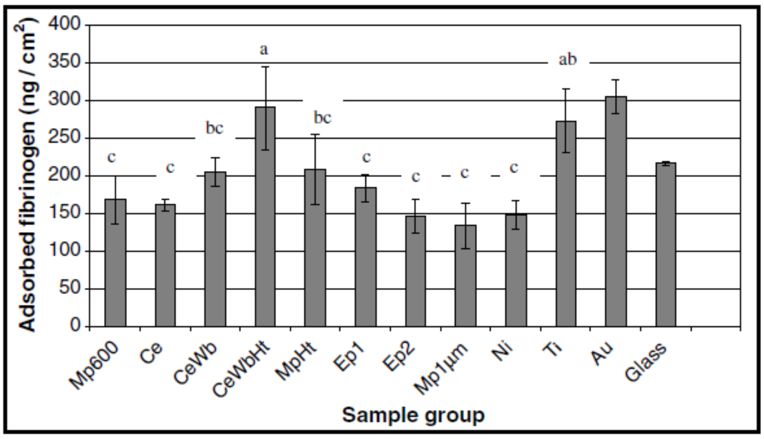

Figure 3.18 – Effect of surface treatment and composition in fibrogen adsorption. Initials: Mp – mechanical polished; Ce – Chemically etched (HF + HNO_3); Wb – water boiled; Ht – heat treated (600ºC); Ep – electropolished (adapted from Shabalovskaya 2008)

Roughness, controlled by the substrate surface treatment, will also have an important part on the clotting and inflammatory behavior. Rougher surfaces have a larger surface area, and also can concentrate negative charges at the surface defects, attracting more fibrinogen. A rough and crystallized TiO_2 surface would be the perfect choice for an orthopedic implant, since a high fibrinogen concentration would lead to fast clotting and healing. A higher number of osteoblast cells would be attracted to the region increasing osseointegration. On the other hand, for an endovascular applications (coronary stent, for instance), the thrombogenic potential should be kept as low as possible to avoid restenosis (narrowing of the blood vessel). A smooth surface with amorphous TiO_2 would be the better choice for this kind of application.

4. Materials and Methods

This research was performed in a joint effort between Universidade Federal de Minas Gerais (UFMG, Belo Horizonte – Brazil) and Université Grenoble Alpes (Grenoble – France) through SIMaP laboratory. The study was divided into three main steps: the development and optimization of the deposition route, characterization of the TiO_2 coated samples and application of the procedure to coat endodontic instruments in a practical case. The deposition route was developed using the labs of both universities. Characterization of the film was mainly performed at SIMaP labs, while the coating and tests on endodontic instruments were done using UFMG facilities.

4.1 Materials

The substrate chosen for the development of the coating route and characterization of the film was a superelastic NiTi rectangular strip (0.64 x 3.56 mm) acquired from Nitinol Devices and Components (NDC, Fremont, CA, USA) with the nominal composition 50.8 at.% Ni – 49.2 at.% Ti (Figure 4.1a). Despite the fact that most of the biomedical and dental devices are manufactured from NiTi wires, the strips were chosen to facilitate the characterization, since some of the techniques employed work better with flat substrates (XRD, XPS, Raman, etc.).

For the practical application of the developed TiO_2 coating, 48 endodontic instruments model RaCe (FKG, La Chaux-De-Fonds, Switzerland) with a triangular cross-section, a 0.25 mm tip diameter and a 0.06 mm/mm taper were employed (RaCe 25/0.06 – Figure 4.1). They were equally and randomly divided into 3 groups: a control group with as-received instruments (AR), a TiO_2 coated instruments group (CI) and a third comparative uncoated group which passed through the same thermal treatment (TT) used for film drying and crystallization of the samples of the CI group. All experiments were performed comparatively between these three groups of samples. The RaCe

25/0.06 instruments were chosen due to their large caliber, making them more susceptible to fatigue fracture (one of the properties this work is trying to improve), and also because they passed through electropolishing, presenting a smoother surface that facilitates the deposition of a continuous film.

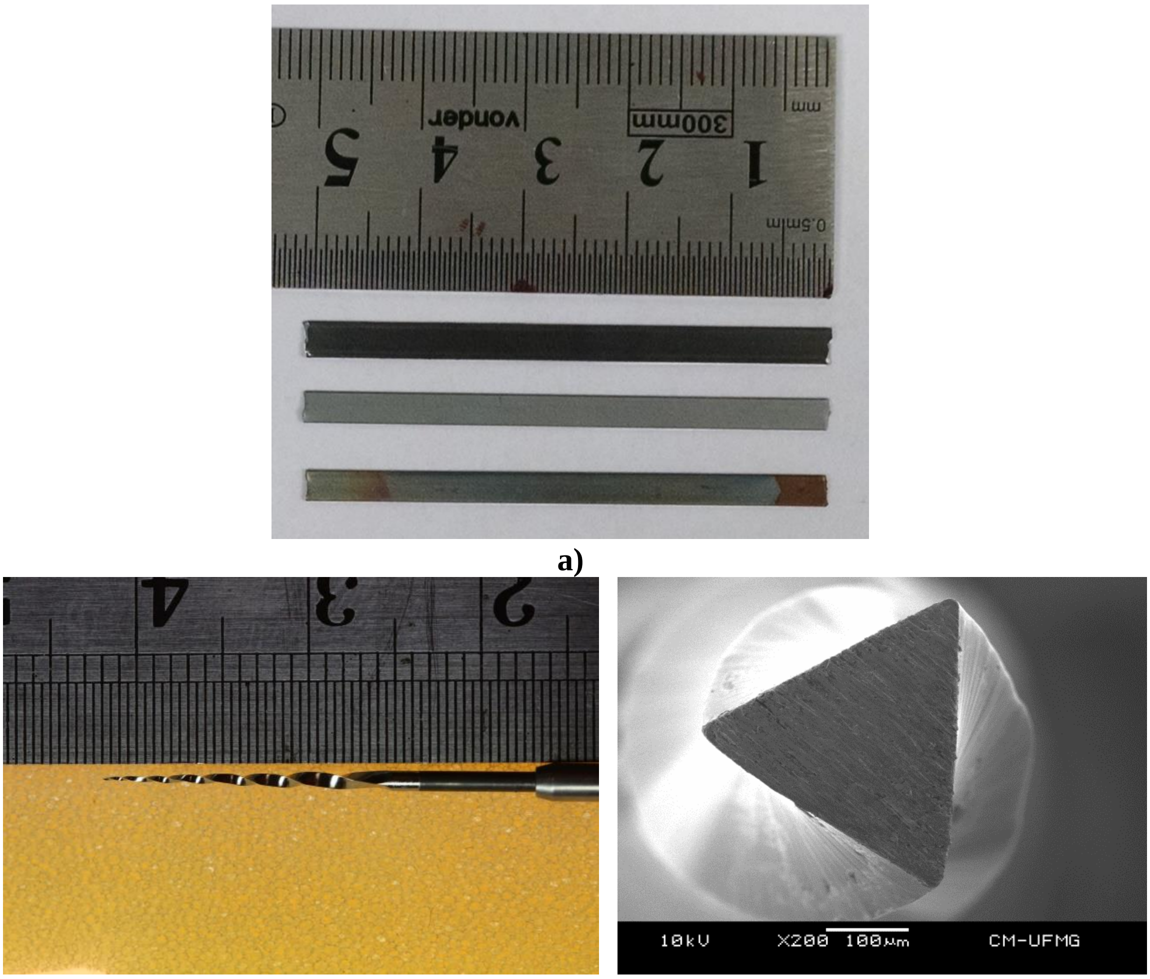

a)

b) **c)**

Figure 4.1 - a) NiTi superelastic strips used to develop the deposition route and perform film characterization; strip as received (top), chemically etched (middle) and TiO2 coated (botton); b) NiTi endodontic instrument model RaCe 25/0.06; c) endodontic instrument cross section

4.2. Sol-gel TiO_2 deposition

Sol-gel is the name given to a group of techniques in which an inorganic or hybrid inorganic/organic solid (gel) is obtained by means of reactions in a liquid dispersion (sol). Films, fibers, powder and glasses can be produced using the sol-gel method (Houmard 2009).

The deposition solution can be produced with metallic salts or alkoxides precursors. Since they do not require elimination of supplementary anions after the reactions, alkoxide routes are currently more used. This route is based on the hydrolysis and condensation of $M(OR)_N$ type molecules, where “M” is a metal atom with valence “N” and R represent an organic radical. The complete reactions involved in the process for a metal of valence 4^+, as is the case of Ti, would be:

$$M(OR)_4 + 4\ H_2O \rightarrow M(OH)_4 + 4\ ROH \text{ (hydrolysis)}$$

$$M(OH)_4 + M(OH)_4 \rightarrow (OH)_3\text{-}M\text{-}O\text{-}M\text{-}(OH)_3 + H_2O \text{ (aqueous condensation)}$$

$$M(OH)_4 + M(OR)_4 \rightarrow (OH)_3\text{-}M\text{-}O\text{-}M\text{-}(OH)_3 + ROH \text{ (alcoholic condensation)}$$

The sol is formed when alkoxide condensation generates polymeric oxide chains with sizes in the order of 100 nm, which are kept disperse in the liquid solution by the Brownian movement. The control of particle size and sol stability is performed adding acids or bases. Over time (aging), condensation reactions will form a solid lattice (gel), trapping the solvent inside its pores. The removal of this liquid can be achieved either by supercritical drying, forming a light density solid with a high porosity (aerogel) or by natural evaporation, creating a more dense but still porous material (xerogel). The solid thus formed is generally in its amorphous state (Figure 4.2). To eliminate the porous and crystallize the material, a heat treatment can be applied after the sol-gel process is complete (Hench & West 1990, Houmard 2009).

Films can be deposited from the sol through dip, spin or spray-coating techniques. The dip-coating sol-gel route was chosen in this work for the following reasons: its practicality, making it easily applied in the industry, relatively low cost, capacity to coat complex geometries (as is the case of endodontic instruments, for instance) by a simple immersion of the object in the precursor solution, good film composition and thickness control and the fact that, for the case of deposition of amorphous films, it does not require a high temperature treatment.

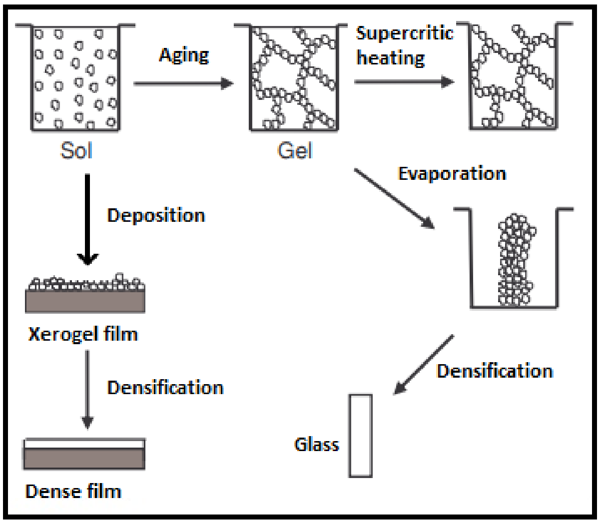

Figure 4.2 – Formative stages of a solid generated via sol-gel (adapted from Houmard 2009)

The precursor solution for this research was prepared according to the route proposed by Burgos and Langlet (1999a; 1999b; Houmard *et al.* 2009) based on the hydrolysis and policondensation of the titanium (IV) isopropoxide (TIPT). The reactions involved in the process are illustrated in Figure 4.3.

The TIPT is highly reactive with water, in the presence of which it will quickly hydrolyze, condensate and precipitate in the form of TiO_2. The stability of the sol was achieved by Burgos and Langlet by using absolute ethanol as a solvent, controlling the amount of water added to the solution and changing the pH with the addition of HCl.

The water to TIPT ratio will control kinetics and reduce speed of the hydrolysis reactions. The high concentration of H^+ on the solution caused by the addition of HCl will eventually cause protonation of the polymeric TiO_2 chains, charging positively the nanometric particles. Electrostatic forces will then avoid the approximation of these electrically charged chains, preventing their condensation reactions. Figure 4.4 summarizes the results of Burgos and Langlet studies performed at 60ºC and the final solution composition. The indicated solution was reproduced, generating a translucent dispersion of TiO_2 stable at room temperature for a period superior to 4 months. This solution was used on the deposition of all the TiO_2 films related to this work.

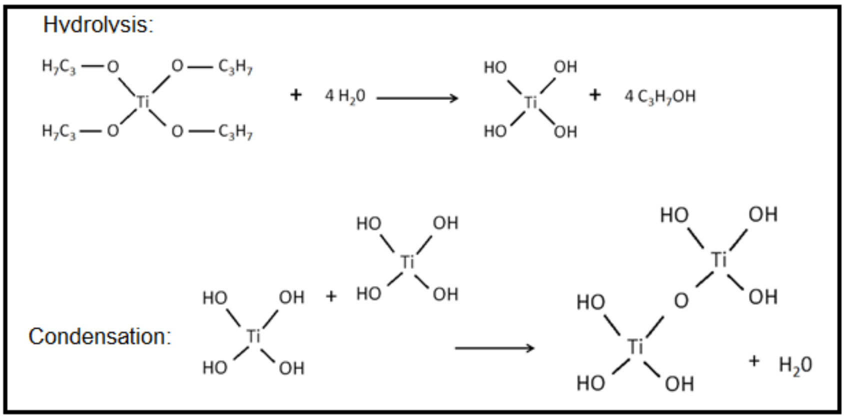

Figure 4.3– Hydrolysis and condensation of TIPT

Prior to the deposition, NiTi strips were chemically etched in a 50 wt.% H_3PO_4 30 wt.% H_2O_2 (Okazaki *et al.* 2013) during 20 min at 80ºC to remove the surface defects and natural oxide formed during rolling. Strips and endodontic instruments were ultrasonically cleaned in a 1/1 vol. acetone and ethanol solution for 2 min, rinsed with water and dried in air immediately before the deposition.

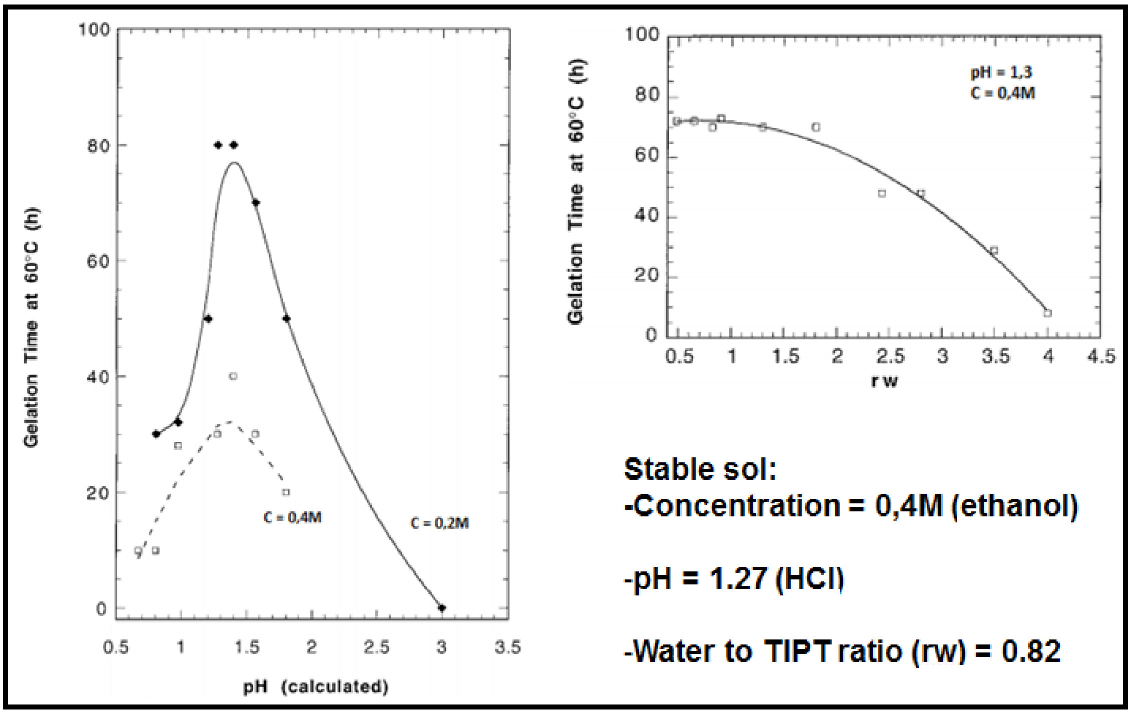

Stable sol:

-Concentration = 0,4M (ethanol)

-pH = 1.27 (HCl)

-Water to TIPT ratio (rw) = 0.82

Figure 4.4– TiO_2 sol stability at 60ºC study performed by Burgos and Langlet (1999a)

The samples were then dipped in the solution for 2 minutes and removed with a withdraw speed of 7.5 mm/s controlled by a dip-coating machine developed to have a high control of velocity (Figure 4.5). After removal, samples were left to dry in air on the vertical position (still attached to the dip-coating machine clamp) for 1 minute before being taken to the thermal treatment.

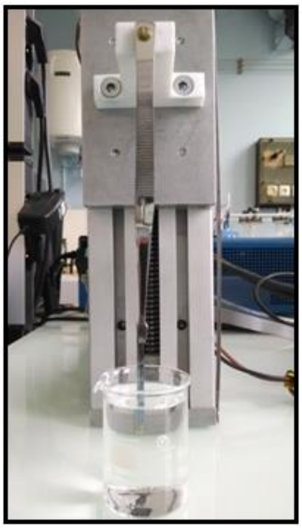

Figure 4.5– Dip-coating machine (SIMaP, Grenoble – France)

The maximum film flexibility was achieved with a thermal treatment post-deposition in 3 steps:

1) Humid thermal treatment at 100ºC: firstly, the samples were dried on a humid atmosphere at 100ºC for 45 minutes. The water vapor in this step will reduce ethanol evaporation rate. The film will slowly be formed over a thermally expanded NiTi substrate. After removal from the oven, the film will be on a compressive state, ideal to avoid crack formation.
2) Dry atmosphere thermal treatment at 110ºC for 2 hours: This step is needed to completely remove any residual solvent still trapped in the TiO_2 layer pores. At the end of this step, a flexible amorphous TiO_2 film will be attached to the NiTi surface.
3) Crystallization at 500ºC for 10 minutes: as will be discussed in chapter 5, maximum film flexibility was achieved for a semi-crystallized layer. The best result was accomplished with a fast crystallization treatment for 10 minutes at 500ºC in a preheated furnace.

4.3. Film characterization

After optimization of the deposition route, the oxide layer was applied to coat chemically etched NiTi superelastic strips and endodontic instruments model RaCe 25/0.06. The coated and uncoated samples were analyzed regarding chemical, mechanical end physical properties. The techniques employed will be described below.

4.3.1. Three-points bending tests

The three-points bending test is a mechanical test in which a sample with a known cross section (normally rectangular or circular) is supported over two fix pins separated by a distance “L” and a third loading pin is lowered from above applying a force at a distance “L/2”. The reaction force on the loading pin is recorded as a function of the lowering distance “d” (Figure 4.6a). During the test, the half upper-part of the sample will be compressed, while the down part will be under tensile load. The results can be used to calculate modulus of elasticity on bending, flexural stress and strain, fracture toughness, among other parameters.

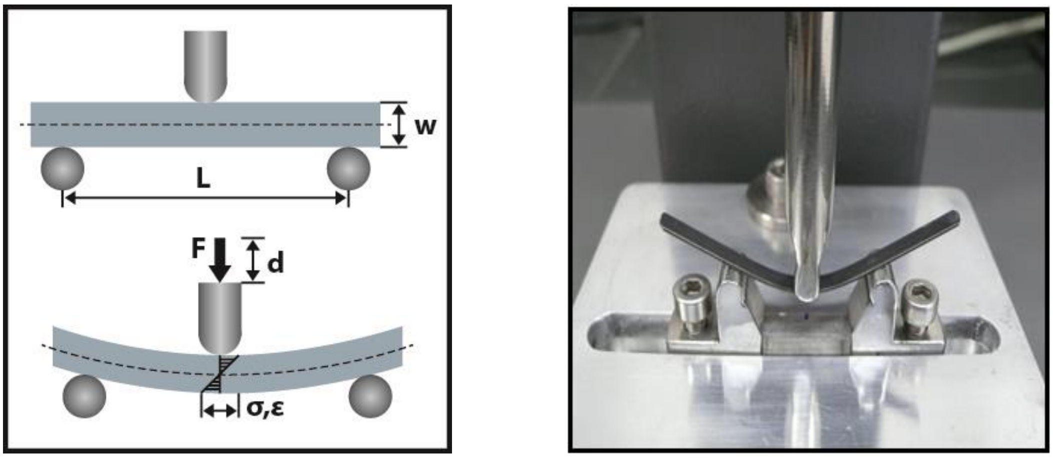

a) **b)**

Figure 4.6 – Three-points bending test. a) experimental setup scheme; b) experimental assembly used on this work

For this research, the three-points bending test was used to apply a chosen strain on the sample surface in order to study film flexibility and also, force x distance curves (distance of movement of the loading pin) were recorded to investigate the influence of the thermal treatment in the substrate mechanical properties. The maximum strain applied was calculated according to the equation (Timoshenko 1958):

$$\varepsilon = \frac{6wd}{L^2}, \tag{4.1}$$

where "ε" is the maximum strain, "w" is the sample width, "d" the lowering distance of the loading pin and "L" is the distance between the support pins. Controlling the lowering distance of the loading pin and knowing the sample dimensions, it was possible to calculate specific values of strain applied on the bottom central part of the NiTi coated strips. This value is not entirely precise since, for large deformations, sliding between sample and the support pins will slightly change the values of “L”. The objective of this experiment was to investigate the TiO_2 coating flexibility by applying successively larger deformations and look for film cracking using scanning electron microscope images. Table IV.1 shows the values of deformation applied. A total of 10 samples were tested for each deformation, 5 of them strained once and the other five strained 10 times before the analysis in the microscope.

Table IV-1– Strains applied on TiO_2 coated NiTi strips.

ε (%)	**L (mm)**	**w (mm)**	**d (mm)**
1.0	26	0.56	2.01
2.0	26	0.56	4.02
2.5	23	0.56	3.94
3.0	26	0.56	6.04
4.0	26	0.56	8.05
5.1	23	0.56	8.03
6.4	23	0.56	10.08

4.3.2. Flexural fatigue tests

To assess the fatigue life of endodontic instruments, the methodology employed (Bahia *et al.* 2006) makes use of an artificial canal made of AISI H13 tool steel (Figure 4.7) consisting of an arch whose angle of curvature was 45°, radius of 5 mm and a guide cylinder 1 mm in diameter, made of the same material. After machining, the artificial canal was quenched to prevent wear by friction with the rotating files. Because each instrument was adjusted to the guide cylinder, all tests were performed with the same radius of curvature measured tangentially to the open side of their curved region. The artificial canal geometry was chosen in accordance with the mean values of angle and radius of curvature previously determined in molars (Bahia & Buono 2005, Martins *et al.* 2006, Vieira *et al.* 2008) and placed the area of maximum tensile strain amplitude at about 3 mm from the tip of the instrument, region where most frequently fractures by fatigue occur.

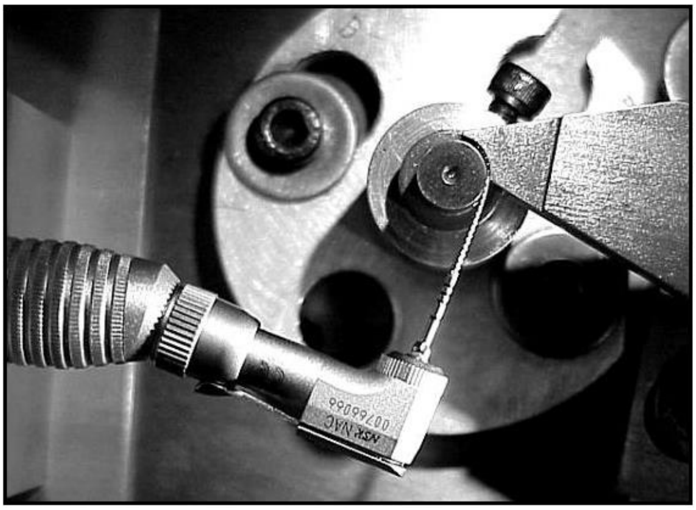

Figure 4.7– Artificial canal bench used to perform fatigue tests on the endodontic instruments

The fatigue life was measured by the number of cycles (N_f) until the fracture. The time to fracture was recorded using a digital chronometer and converted to N_f by multiplying the time measured by the rotation speed (300 rpm) selected to the test. During rotation of the instruments inside the artificial canal, mineral oil was used as lubricant to avoid heating and torsional overload. The point of fracture in relation to the tip of the instrument was determined by measuring the broken file with an endodontic rule. The tests were performed at room temperature (25 ± 3 ºC)

For this investigation, 10 NiTi instruments model RaCe 25/0.06 of each group (AR, CI and TT) were tested in flexural fatigue before the corrosion experiments, and 6 instruments after this test. These files were chosen because of their larger diameters, which make them more prone to fatigue failure during clinical use (Melo 1999, Bahia & Buono 2005).

4.3.3. Cutting efficiency

As mentioned in section 3.2.3, there is no standardized experiment to measure the cutting efficiency of endodontic instruments. Cutting capacity of the instruments was assessed using a procedure developed by the group and already used in another research (Peixoto *et al*. 2015). The method is based on the amount of the energy necessary to drill through a standard artificial canal keeping constant the engine rotation and the apical speed. The device is show in Figure 4.8. A total of 10 samples from each group (AR, CI and TT) were used to shape a 20 mm straight artificial canal carved in acrylic blocks (IM DO BRASIL, São Paulo, Brazil). The new plastic blocks were manually explored with stainless steel K-files diameter #10 and #15 by an experienced endodontist prior to the experiment in order to normalize its shape, diameter and taper. After that, the analyzed instruments were attached to a fix handpiece linked to an X-Smart motor (Dentsply Maillefer, Ballaigues, Switzerland), which was set to rotate at a constant speed of 300 rpm and a maximum torque of 5.0 Ncm. The acrylic blocks were attached to a universal testing machine (Analógica AN8032, Belo Horizonte, Brazil) capable of moving the piece at constant speed of 5.4 mm/min and record the apical force during the experiment. The electrical current delivered to the handpiece was recorded with an ammeter (DMM 4020, Tokyo, Japan) in order to maintain rotation and penetration speed constant. A previous calibration of the set up changing the values of maximum torque and measuring the maximum currents delivered to the handpiece (mean values after 10 measurements) showed a linear relation between current and torque. A simple linear equation was then created to transform the measured current into torque units. The calibration curve is presented at appendix A.

The test machine load cell recorded the apical force measured in Newtons (N) exerted by the instrument along the canal length. The torque and apical force curves were averaged using OriginPro 9.0 software (OriginLab, Northampton, MA).

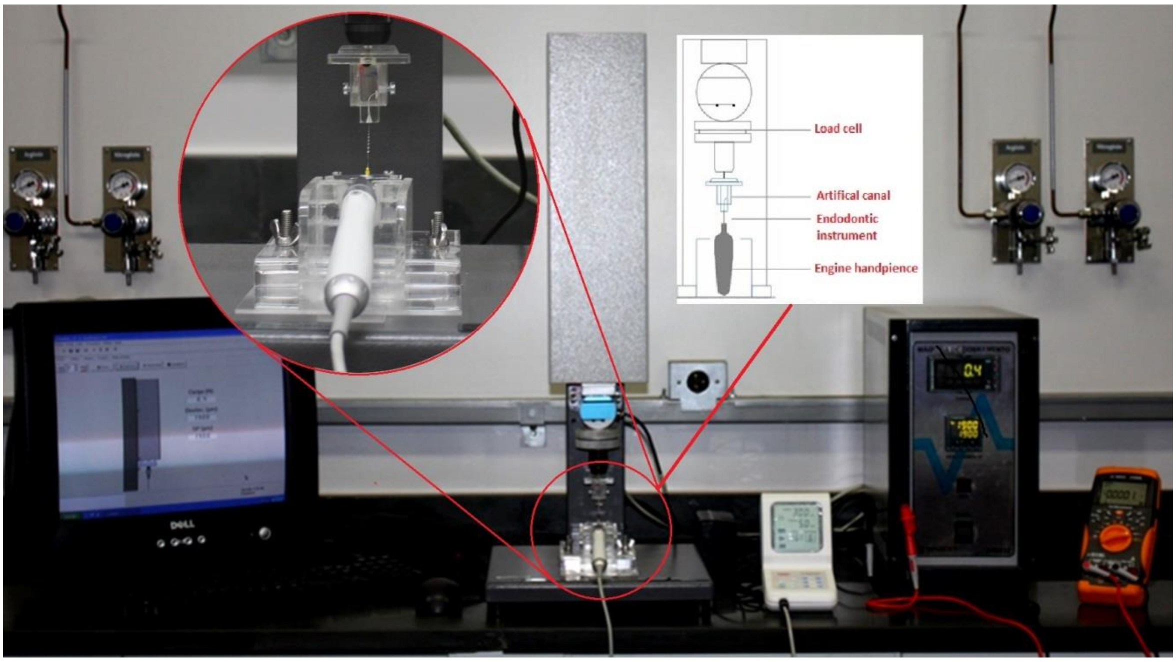

Figure 4.8– Cutting efficiency assembly developed to investigate endodontic instruments (Source: Peixoto 2015)

4.3.4. Microscopic images

Optic microscopes have a limitation of magnification, due to the visible light wavelength. In order to get higher magnifications, other sources of electromagnetic waves with smaller wavelengths should be used. Electronic microscopy is used to analyze samples with a larger level of details. The image is formed when a beam of high energy electrons is focused on the sample. The interaction between the electron beam and the sample will generate a series of particles and wave emissions that can be collected and used for analysis (Figure 4.9). Secondary and backscattered electrons arriving at their specific detectors can be used to generate the image of the illuminated sample. These images show qualitatively the sample morphology and its chemical contrast. The lower energy secondary electron formed by the inelastic interaction between primary beam and sample atoms are used to form high definition images of the sample topography. The elastically reflected electrons (backscattered) are normally used to generate composition dependent images. The probability of elastic chocks increases with the atomic number of the constituents of the sample. Backscattered electron images will then show a contrast between light and heavy elements (Mansur 2012).

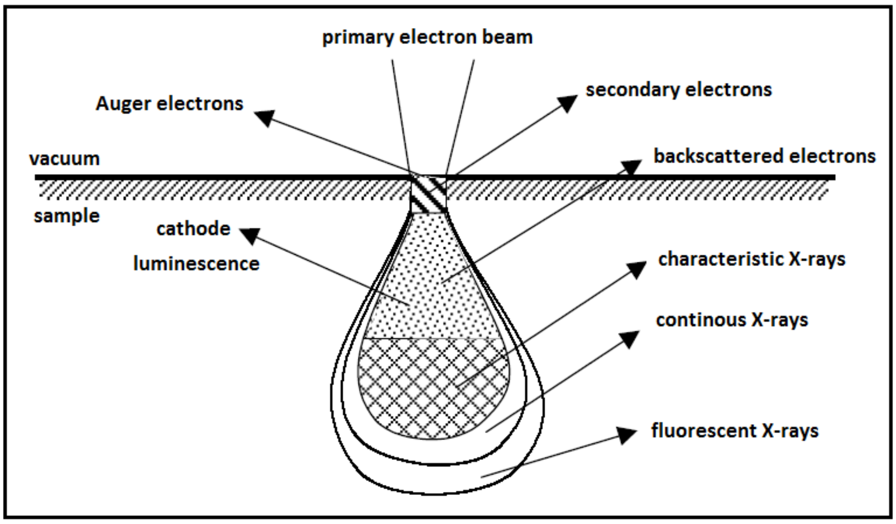

Figure 4.9 – Particles and waves generated by the interaction of a primary electron beam and a sample in the electronic microscope (adapted from Mansur 2012)

The primary electron beam can be focused to present a very small spot size (~1 nm for Field Emission Gun microscopes). The beam can be deflected through application of magnetic fields or electrical potentials and controlled to scan large areas of the sample. The images can be acquired in two main modes: scanning electron microscopy (SEM) or transmission electron microscopy (TEM). The electrons detected to form the image in the TEM technique need to cross through the material to be analyzed, so the sample need to be specially prepared to be extremely thin (50 to 200 nm). The high energy electrons (~200 keV) crossing this thin sample will also be diffracted in the lattice and form a diffraction pattern. This pattern can be used to acquire information about lattice configuration and composition.

A newly developed technique with the commercial name of ASTAR uses the diffraction patterns to generate phase and crystallographic orientation maps in TEM images. In this technique, the diffraction pattern of each point on the sample, collected with a high speed camera, is compared with theoretical patterns generated for all phases present in the sample in all possible orientations, using the kinematic approach. Each point is indexed as the phase oriented in the direction of the best match between measured and calculated patterns. Since the transmitted electron can pass through more than one grain, the diffraction pattern can be formed as a mixture of two or more arrangements. To ensure precision, a reliability map is also generated as a ratio for the two best diffraction matches (two best combinations of phase and orientation). Only points presenting a high values on the reliability map will be indexed. To avoid strong influence of dynamic effects on the diffraction, the incident electrons are precessed (Rauch & Véron 2014).

In both techniques (SEM and TEM), the collisions among electrons of the primary beam and the sample will excite the atoms. The relaxation of these particles will occur by the emission of a characteristic X-ray photon. These photons can be detected and analyzed to give information about the chemical composition of the samples (EDS – Energy Dispersive Spectroscopy). This information can be combined with the topography or transmitted images to form a composition map of the samples.

SEM images where taken with a W-LEO S440 microscope (in France) and a FEI Inspect F50 microscope (in Brazil) with an accelerating voltage of 15 kV, both capable of performing EDS measurements. The main objectives of the images were to verify TiO_2 film uniformity and presence of microcracks before and after deformation of NiTi coated strips an endodontic instruments. Three magnifications were used to examine the presence of defects on the oxide layer: 500x, 1000x, and 5000x. SEM images were also used to compare surface of the endodontic instrument of the three groups before and after the corrosion tests. No metallization was necessary, as determined by comparing images of metallized and non-metallized samples.

Transmission electron microscopy (TEM) images were acquired with a JEOL 2300F transmission microscope using an accelerating voltage of 200kV; it was also possible to apply energy-dispersive X-ray spectroscopy (EDS) and precession-assisted crystal orientation mapping (ASTAR) techniques with this instrument.

Another way to characterize sample surface morphology is through atomic force microscopy (AFM). In this family of techniques, the deformation caused by interatomic forces between atoms of the surface sample and the microscope tip is used to generate a topographic image. In order to get a high resolution, the tip point must be constructed with a very small radius. The small cantilever deformations caused by tip/sample interactions are normally detected with an optical amplification system composed of a laser source and a photodiode (Figure 4.10). The image is constructed with the position of the laser spot on the photodiode as the tip scans the sample surface. Three different modes of scan can be used to generate an AFM image. On the contact mode (right part of Figure 4.10), the electromagnetic repulsion (reaction force) will deflect the tip cantilever as it “scratches” the surface. In the non-contact mode, tip is slightly elevated, and the forces responsible to deflect the support are attractive London forces that are distance dependent. A third “hybrid” mode is called “tapping”, where the tip is set to vibrate “touching” the sample at the lower part of its trajectory. A well calibrated AFM with a sharp tip can produce surface images with atomic resolution, as well as providing information about surface roughness and friction coefficients (Mansur 2012).

The tapping mode was used in this work to generate 3D images of 40 x 40 μm^2 regions of TiO_2 coated and uncoated NiTi superelastic strips (after being chemically etched). Root mean square roughness (rms) measurements were acquired in different locations of the samples. The experiments were performed on an AFM Digital Instrument Nanoscope 3100 with a silicon nitride tip with a 15 nm curvature radius.

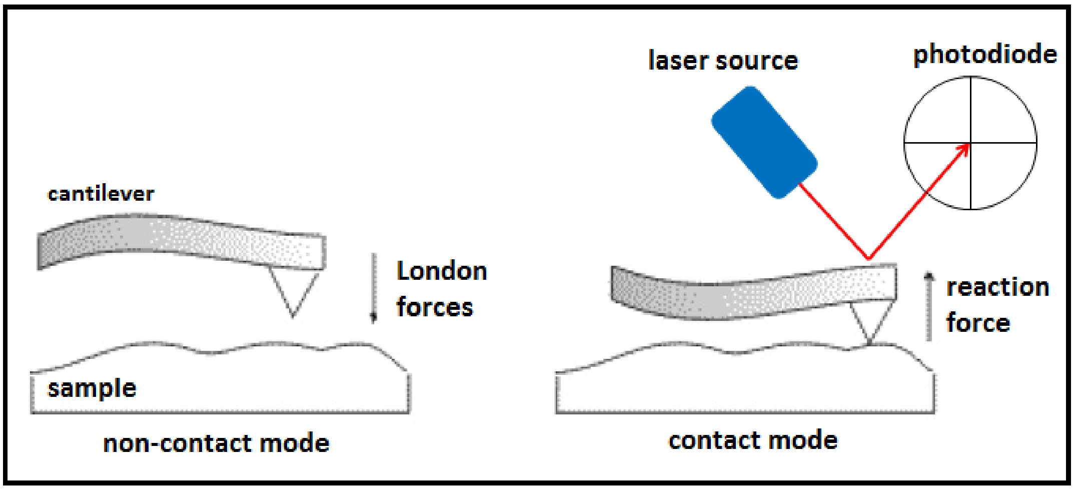

Figure 4.10 – AFM microscopy image generation methods (adapted from Mansur 2012)

4.3.5. Differential Scanning Calorimetry

Differential Scanning Calorimetry (DSC) is a technique used to investigate the thermodynamic of materials phase transition. With its use, it is possible to determine the phase transformation temperatures and also the enthalpy involved in the process. The experiment is performed by heating (or cooling) the examined and a reference samples at a fix rate. The difference between heat fluxes needed to maintain the equal heating (cooling) is computed as a function of the temperature. If, the examined sample passes through a phase transition during this process, it will use all the heat to modify its configuration. The DSC controller will try to compensate the newly formed difference in heating (cooling) rates by adding or removing heat from one of the samples. The difference between heat fluxes will change, forming a peak at the heat flux x temperature plot that can be used to calculate phase transition temperatures and enthalpy (Höhne *et al.* 2003).

With the objective to investigate if the crystallization thermal treatment described on section 4.2.1 was enough to induce significant changes on the martensitic and austenitic phase change temperatures, samples from the three groups of endodontic instruments where analyzed by DSC. The tests were performed on a Shimadzu DSC-60 (Tokyo, Japan) with a temperature range of -100ºC to 100ºC at a fix rate of ±10 ºC/min cooled through liquid nitrogen and heated with nitrogen flow. The tangent intercept method was used to determine the transformation temperatures of the 5 mg samples cut from the active part of 3 instruments of each group.

TiO_2 powder obtained by drying the precursor solution described on section 4.2.1 at 60ºC was also analyzed with DSC. The 10 mg sample was heated from 30 to 600ºC at a 10 ºC/min rate twice, in order to investigate the phase transitions of the oxide.

4.3.6. Grazing Incidence X-ray Diffraction (GIXRD)

X-ray diffraction (XRD) is a powerful technique to analyze crystalline samples, bringing information of its phase composition, lattice structure, preferential orientation, grain size and texture. In this technique, a collimated beam of monochromatic X-ray hits the sample surface and it is scattered by the electrons of the atoms, forming a constructive interference pattern following the Bragg's law and giving information about the interplanar distances of the lattice (Figure 4.10):

$$n\lambda = 2d_{hkl}\sin\theta, \tag{4.2}$$

where "n" is the order of the reflection, "λ" is the X-ray wavelength, "d_{hkl}" is the interplanar distance of the (hkl) plane and "θ" the incidence angle according to the Figure 4.11 (Cullity & Stock 2001).

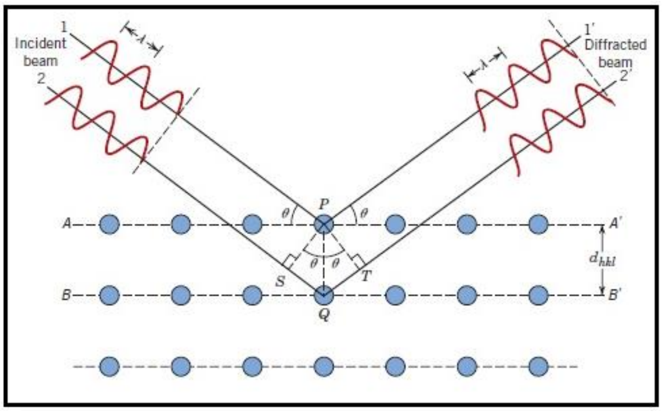

Figure 4.11 – Bragg’s model for diffraction of X-ray by atomic planes (source: Callister 2010)

The normal procedure used in a XRD experiment consists in changing the incidence angle θ while measuring the intensity of the diffracted beams at an angle 2θ measured from the incident beam(Figure 4.12). The penetration depth of the incident and diffracted beams will vary with the angle, but in metals it can reach dozens of micrometers. In order to analyze thin films, a special configuration can be used by fixing the incident angle at a low value and changing only the inclination of the detector (Grazing Incidence X-ray Diffraction – GIXRD). With this setup, the penetration of the X-rays can be reduced to the order of 10 nm, allowing the technique to be applied for the study of thin films.

The result of a GIXRD experiment is given by a plot of diffracted X-ray beam intensity as a function of the detector angle 2θ. The angle position of the diffracted peaks is used to identify the lattice planes and the interplanar distances. For nanocrystalline materials, the peak width will be related to the grain size. Smaller grains will produce wider diffraction peaks. The relation between the peak width and grain size diameter is described by Scherrer equation (Cullity & Stock 2001):

$$t = \frac{k\lambda}{\beta cos\theta} \ , \tag{4.3}$$

where “t” is the grain size, “k” is a constant next to the unit for a sphere model, “λ” the X-ray wavelength, “θ” the diffracted angle and β is the peak width that can be measured by full width at half-maximum (FWHM) or by integral breadth.

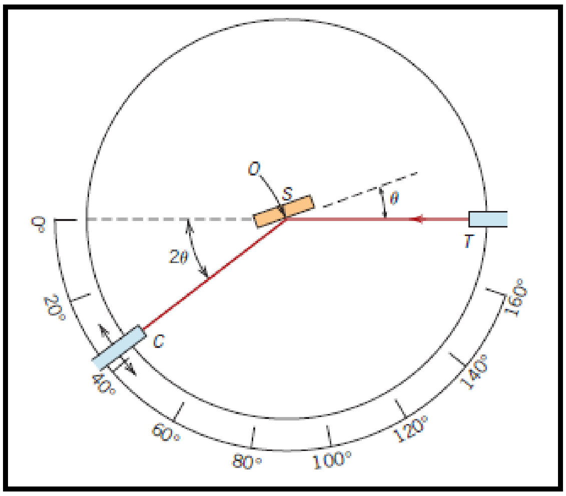

Figure 4.12 – Normal assembly for XRD experiments (Source: Callister 2010)

In this work, TiO_2 coated NiTi superelastic strips that passed through different thermal treatments after deposition where analyzed by GIXRD using a PANalytical X’Pert Pro MPD diffractometer with Cu-K_α radiation (λ = 1.5418 Å), an incidence angle smaller than 1.5º, and an acquisition angle ranging from 20º to 95º with a 0.06º step.

For the crystallite size calculation, the integral breadth was used to measure peak width since this value better computes the widening on the base of the diffracted lines when compared with FWHM values. The contribution of $K_{\alpha 2}$ lines were removed before the calculation, as also the equipment line broadening measured with a Si standard sample.

4.3.7. X-ray Photoelectron Spectroscopy

X-ray Photoelectron Spectroscopy (XPS) is a method developed to analyze the chemical composition of the first few atomic layers of the surface of a solid material. In this technique, an X-ray beam with a known energy is directed to the surface to induce the emission of photoelectrons from the core level of the atoms (Figure 4.13). The kinetic energy of these photoelectrons is then measured with the help of an electron analyzer. The binding energy "BE" of these electrons can then be calculated:

$$BE = h\nu - K - \varphi, \tag{4.4}$$

where "BE" is the binding energy, "hν" the photon energy, "K" the measured kinetic energy and "φ" is the work function of the specific material (difference between the vacuum level and the top energy of the valence band of the solid). The spectrum is built with the count of number of electrons arriving at the detector as a function of the binding energy (Prutton 2002).

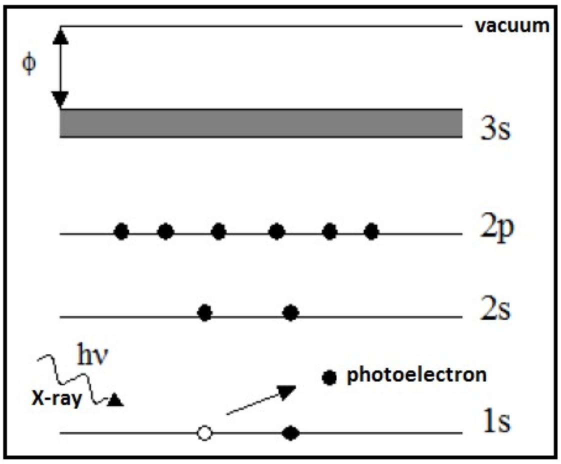

Figure 4.13 – Photoelectron effect on XPS

The X-ray is produced by the relaxation of metallic atoms excited by an electron beam. The most common elements used as a target are the Al and Mg, since they present a lower line width for the emission of the X-ray photons. These photons can penetrate several microns inside a metallic sample. However, the mean free path of electron with the energy between 100 and 1000 eV (normal energies involved on the XPS measurements) inside the solid is generally lower than 10 atomic layers. Only the electrons emitted from the few first dozen monolayers can leave the sample and arrive at the detector without suffering any inelastic collision. Electrons that passed through an inelastic process normally loose kinetic energy and are counted as a background signal for higher binding energies.

Since the binding energy of each element is very specific, the analysis of the spectrum will give the chemical composition of this few dozen nanometers on the surface. The analyzed depth can be modified collecting emerging photoelectrons at different angles (Figure 4.14). Photoelectrons emerging with a grazing incidence angle will have to cross a larger path inside the solid, suffering more collisions. In this situation, only electrons arriving from the first few atomic layers will arrive at the detector without suffering inelastic chocks.

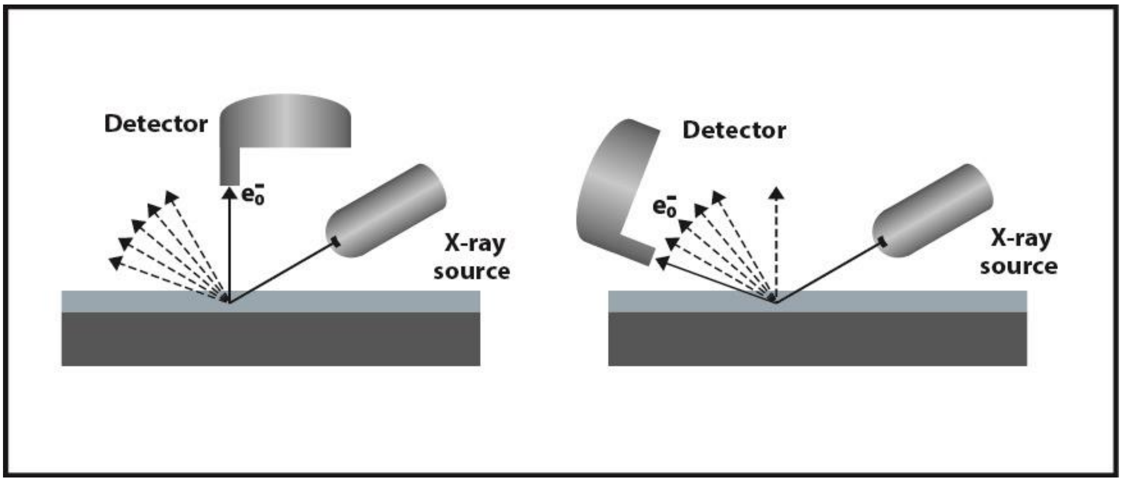

Figure 4.14 – Angle resolved XPS for depth analysis control

The presence of the immediate neighbor atoms can induce a small change (~1 eV) in the core energy level of an element, and consequently the detected energy of the photoelectron. Each element will then emit photoelectrons with slightly different energies. The superimposed combination of the counts will form a single peak in the spectrum that should be deconvoluted for refinement of the analysis. This procedure will tell not only the concentration of that specific element on the surface, but also the oxidative state of each contribution. In order to measure the concentration of each contribution and each element, the follow equation can be used:

$$C_N = \frac{\frac{I_N}{S_N}}{\sum_x \frac{I_x}{S_x}}, \qquad (4.5)$$

Where" C_N" is the concentration of element "N", "I" is the peak area on XPS spectrum and "S" is the sensibility factor of that specific element. The sensibility factor is an experimental constant involving the element cross section for the photoelectron effect and the specific XPS assembly.

In this work, NiTi substrates and coated alloys were analyzed by XPS using Mg K_α radiation and an Alpha 110 electron analyzer, with acquisition angles of 30° and 90°. The coated strips were introduced in the vacuum chamber soon after being ultrasonically cleaned in a solution 1/1 vol. of acetone and ethanol, followed by argon plasma cleaning at 50 W for 10 min. Survey spectrums were collected from 0 to 1100 eV with constant pass energy of 40 eV and a 0.5 eV resolution. Specific spectra were collected with a 0.1 eV resolution for C_{1s}, O_{1s}, Ni_{2p}, and Ti_{2p} orbitals. All the results were calibrated using the position of the C_{1s} peak, set as 284.6 eV. The base pressure for the experiments was 5×10^{-10} mbar. Decomposition of selected peaks was performed with Advantage software with a smart background and a 0.10 ratio for the Lorentzian/Gaussian curves.

4.3.8. Raman cartography

Raman spectroscopy is a technique based in the inelastic scattering of a monochromatic light by the tested sample. In a Raman experiment, the material is illuminated by a beam of monochromatic light, normally in the visible specter (near infrared and near ultraviolet are also used) and the emerging photons presenting a different energy are collected and counted (Vandenabeele 2010).

Atoms and molecules vibrate with specific and quantized frequencies. When interacting with an incident photon of frequency ν_o, the system can respond in three different ways:

1) The atom/molecule in its base vibrational state will absorb the photon, increase its frequency by $\nu_{o,}$ relax back to the base state and emit a photon with frequency ν_o. This would characterize an elastic interaction with light called Rayleigh scattering.
2) The atom/molecule will absorb the photon, use part of its energy to go to a higher vibration mode and emit a photon with a lower frequency $\nu_o - \nu_m$, called Stokes frequency.
3) The atom/molecule already on an excited vibration mode will absorb the incoming photon, relax back to the base state and emit an anti-Stokes photon with frequency $\nu_o + \nu_m$.

Since the vibrational modes of atoms and molecules are specific (as energy levels for electrons in the atom), the inelastic scattering described on items 2 and 3 can be used to identify sample composition and types of chemical bonding between elements. The result of the experiment is a plot of number of scattered photons as a function of its energy. More often, the energy axis is substituted to the Raman shift Δw, measured in wavenumbers and proportional to the energy by a factor hc (Planck's constant times speed of light).

$$\Delta w = \frac{1}{\lambda_0} - \frac{1}{\lambda_r}, \tag{4.6}$$

where $1/\lambda_o$ and $1/\lambda_r$ are wavenumbers of the exciting and the Raman radiation respectively.

A Raman spectrum can be decomposed as a linear combination of the standard signal of each element or molecule present in the sample. The coefficients of the best fit, corrected by a sensibility factor, will inform the relative quantities of the constituents. Applying this methodology in different points of the sample can generate a composition map of the surface (Raman cartography).

In this work, Raman cartography was performed using a RM1000 Renishaw spectrometer equipped with an air-cooled CCD detector, an objective lens of 50x (Na = 0.75), and a 10 mW green Ar^+ laser (λ = 514 nm) using an acquisition time of 20 s. The wavenumber range analyzed was 80 – 1300 cm^{-1} with a 0.1 cm^{-1} resolution. Two cartographies were acquired in different locations on a 35× 50 μm^2 area with a lateral resolution of 1.3 µm of the TiO_2 coated NiTi samples treated at 500ºC for 10 min post sol-gel deposition. The standard spectra for the TiO_2 phases (amorphous, anatase and rutile) used for the decomposition of the result spectra were acquired at specific points on the same sample. Measurements at the same point with different acquisition times showed that 20 s was not enough to induce any phase transformation through heating.

Renishaw WIRE 3.0 software was used to determine the peak frequency and perform width extraction and experimental spectrum fitting.

4.3.9. Cyclic polarization tests

Cyclic Potentiodynamic Polarization test (CPP) is an electrochemical experiment designed to investigate the corrosion behavior of metals in a specific environment. The technique is used to differentiate between corrosion modes (general, uniform or localized corrosion) and to calculate corrosion current densities, which is related to the corrosion rate of the sample through the Faraday's law (McCafferty 2010).

The test is conducted in an electrochemical cell consisted of a recipient filled with the electrolytic solution, one working electrode (WE, metallic sample), one reference electrode (RE) and a counter electrode (CE). In CPP, the potential between work and reference electrodes is scanned in the noble direction, starting at (or lower than) the open circuit potential, while recording the electrical current between WE and CE. The scan direction is reversed when the potential or current reaches a specified maximum value. Usually, the result of the experiment is presented on a semi-log plot of potential (E) x log (current - i). A typical curve of a sample susceptible to localized corrosion is shown in Figure 4.15.

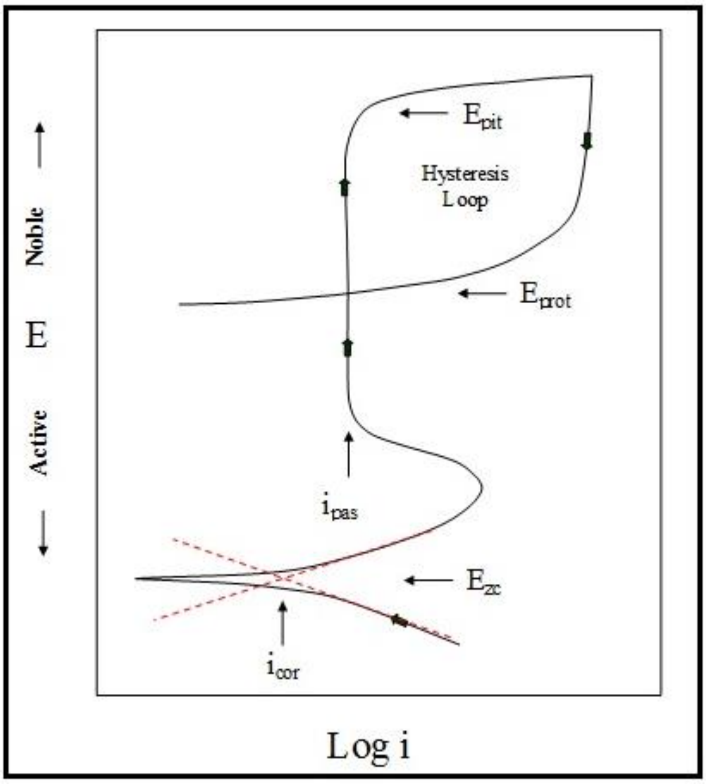

Figure 4.15 – Typical cyclic polarization E x log(i) curve for a metal susceptible to pitting corrosion

The values indicated in Fig. 4.15 are used for the corrosion analysis and are described below (McCafferty 2010):

- E_{ocp} (not shown in the plot): open circuit potential. Is the measured potential between WE and RE before energization of the CPP circuit. Normally, E_{ocp} changes during a certain time until reaches an equilibrium value, when the sample is immerged in the solution. Prior to the CPP experiment, one should wait the stabilization of the E_{ocp} since this parameter is used as an input for the test.

- E_{zc}: zero current potential. Potential at which the current density changes polarity during the forward scan. Is also the potential value where current is smaller. E_{zc} is normally slightly nobler then the open circuit potential (E_{ocp}).
- E_{pit}: pitting potential or breakdown potential. Potential at which current density starts increasing rapidly, due to development of pitting corrosion
- E_{prot}: protection potential. Potential at which pits stop developing (passivate) during reverse scan.
- i_{cor}: corrosion current density. This value is related to the overall corrosion rate of the sample.
- i_{pas}: passive current density. Current density in the passive range of the scan.

Some materials will present a left (negative) hysteresis loop, indicating that pits are not stable (high repassivating capability). Crevice and pitting corrosion are unlikely to occur in this type of samples. Also, materials presenting a right hysteresis loop but with a high value of E_{prot} - E_{zc} are corrosion resistant. This high difference indicates that the normal potentials in which the samples are subjected are distant from the values where pits are stable (above E_{prot}). A curve showing a continuous increase on the current density would characterize a material susceptible to general corrosion.

In this work, cyclic polarization tests were performed to compare corrosion behavior of coated and uncoated endodontic instruments. The CPP tests were performed using ASTM F2129 norm as a guide on a Autolab 8086 galvanostat, with a 5.25 % NaClO solution (measured pH = 12.3) prepared immediately before each experiment from a more concentrated solution (12%) stored in an opaque vial kept in a dark armoire at temperatures under 25ºC to avoid aging of the liquid. Saturated Calomel Electrode (SCE) was used as a reference electrode with a platinum grating working as the counter electrode. Only the firsts 14 mm of the active part of the instrument were submerged in the solution for the tests. The open circuit potential (E_{ocp}) was acquired for a period of 1 hour. Initial potential was set 200 mV bellow OCP, with a scanning rate of 0.5 mV/s up to a maximum potential of 2.0 V over OCP, higher than the one recommended by the ASTM F2129. This higher value was chosen because the endodontic files are attached to an electric engine during utilization. Higher values of potentials (higher than the 800 mV proposed by the norm) can sometimes be expected for this specific application. The immerged instruments area used for calculation of current densities was stipulated as 0.24 cm^2 (surface area of a triangular sectioned pyramid with the same taper and dimensions of the tested files). This value is not precise, but, since the exposed area was the same for all the tested samples, the current values could be compared.

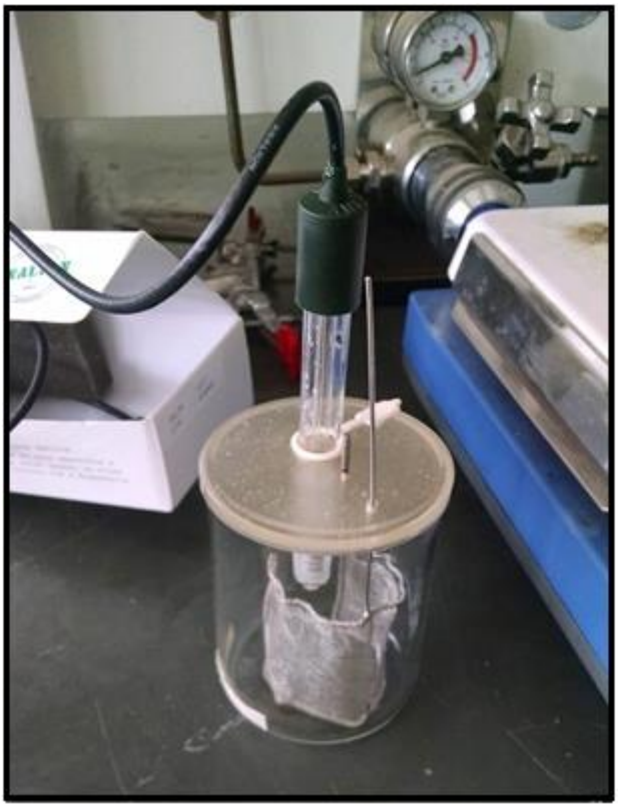

Figure 4.16 – Electrochemical cell used for CPP experiments

Before each measurement, the samples were ultrasonic cleaned for 5 min in a solution 1/1 vol. of ethanol and acetone and rinsed with distillated water. The galvanostat was equipped with a Faraday cage to avoid external interference. A total of 6 samples from each group (AR, CI and TT) were used in these tests.

5. Results and discussion

5.1. TiO_2 film flexibility/biocompatibility optimization

The sol-gel deposition route described in section 4.2.1 (withdraw speed of 7.5m m/s, humid thermal treatment at 100ºC for 45 min, dry thermal treatment at 110ºC for 2 hours and crystallization treatment at 500ºC for 10 min) was the final recipe to obtain optimization between film flexibility and biocompatibility. To arrive at this formula, a deposition loop (Figure 5.1) was used to investigate each coating parameter until the best film performance was achieved.

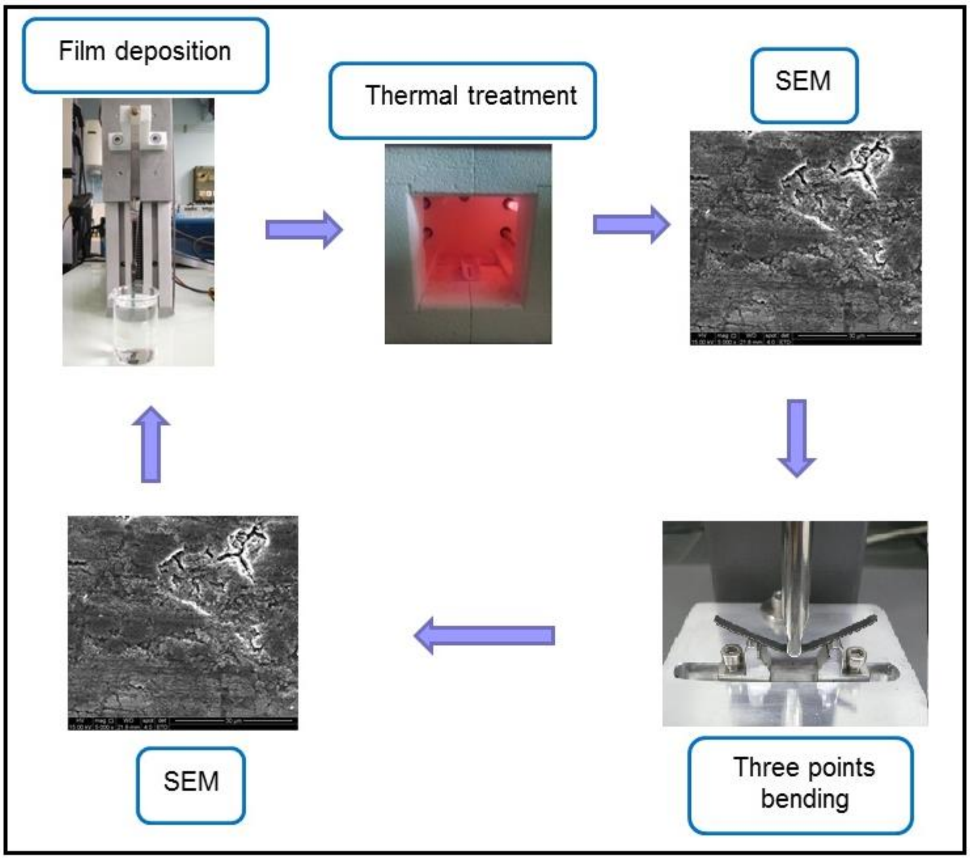

Figure 5.1- Sol-gel deposition loop to obtain optimal film flexibility and biocompatibility

The first deposition tests were conducted with NiTi superelastic strips (50.8 at.% Ni) as received from the factory. The thermomechanical treatment required to obtain a large deformation plateau in the superelastic regime described in section 3.2.1 leaves a high concentration of surface defects on the substrate (Figure 5.2a). Films deposited with this condition cracked during the drying procedure, as shown in Figure 5.2b. This result indicates the need of a surface treatment pre-deposition in order to eliminate defects and decrease the surface roughness.

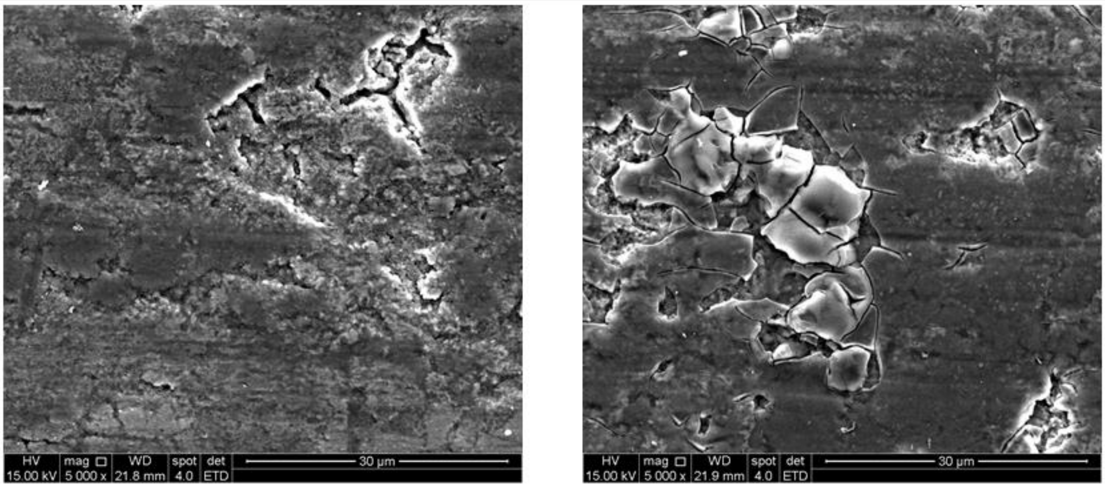

a) b)

Figure 5.2 – Secondary electron images. a) Superelastic NiTi strip surface as received from the factory; b) Cracked TiO_2 layer over NiTi strip after film drying

The first tested surface treatment was mechanical polishing. NiTi strips were polished with #400, #600 and #1200 abrasive paper and finished with 9, 3 and 1μm diamond paste, leaving a mirror like surface. Coating these substrates without the densification thermal treatment using different withdraw speeds generated smooth and continuous TiO_2 films, as it can be observed qualitatively by the roughness decrease between Figures 5.3a and 5.3c. The presence of the films was confirmed by a higher peak intensity of the oxygen line on the EDS spectra (Figs. 5.3b and 5.3d). These TiO_2 films are amorphous, as can be deducted by the lack of anatase or rutile peaks in comparative GIXRD diffractogram showed in Figure 5.4. The oxide layer could sustain up to 4.0%

strain applied in three-points bending tests without cracking (Figure 5.3c). However, the film was severally cracked after a 5.0% strain was applied at the surface, as can be seen in Figure 5.3e.

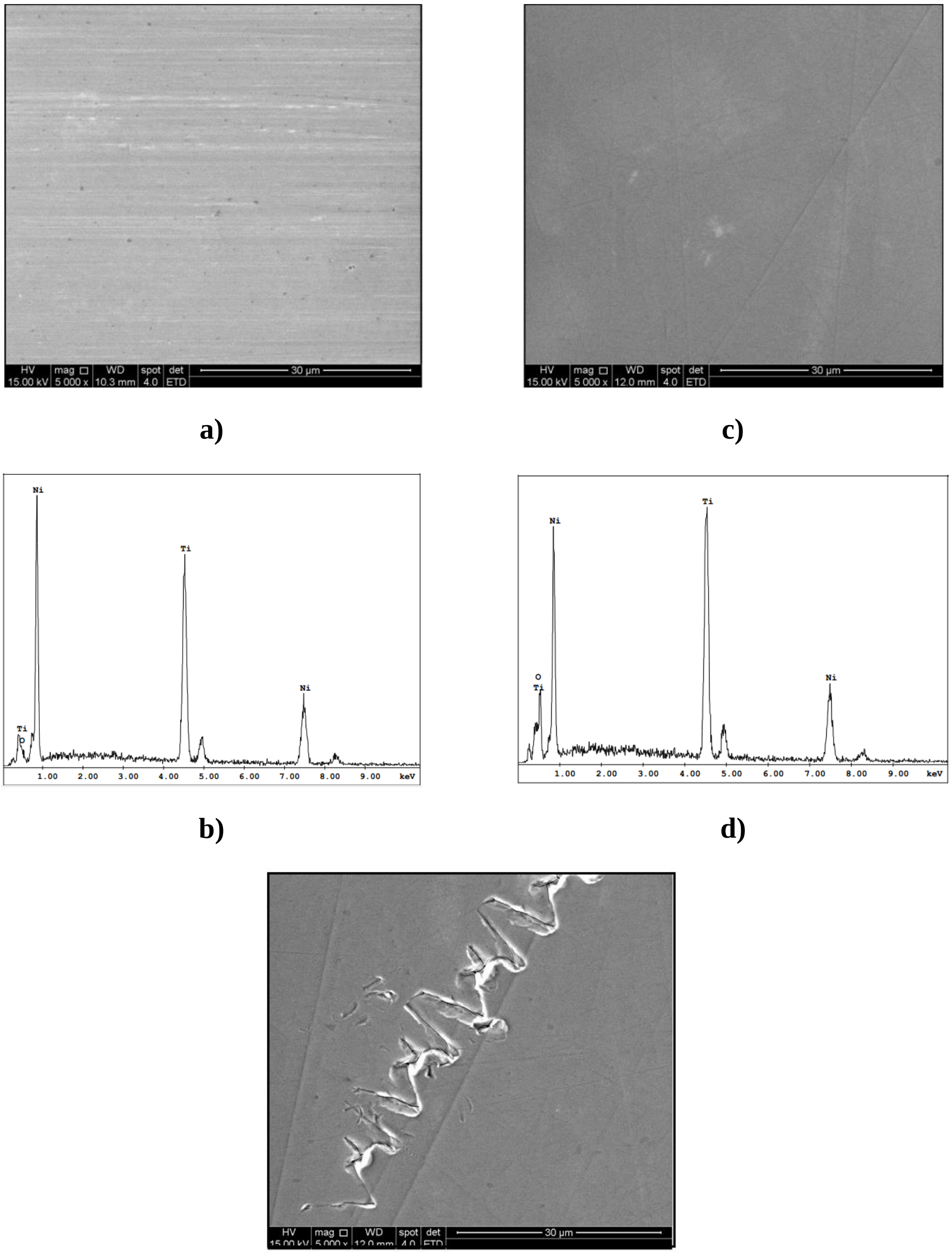

a) **c)**

b) **d)**

e)

Figure 5.3 – Secondary electron images of a) polished NiTi sample and its b) EDS; c) TiO_2 coated NiTi after 4.0% strain applied and its d) EDS; e) TiO_2 coated NiTi after 5.0% strain applied (TiO_2 films dried at 110ºC for 2 hours).

Despite the advantage of a low roughness of the mechanical polished samples which favor the formation of a continuous oxide layer, this treatment is not practical for most of the biological applications of the superelastic alloy. The polishing procedure shows a low reproducibility, adds inclusions on the surface and is not practical for a wire substrate (Shabalovskaya *et al.* 2008). Due to these disadvantages, the NiTi surface should be treated by another method in order to eliminate most of surface defects and reduce roughness. A simple procedure to achieve this goal is to use an acid solution to chemically etch the metal surface.

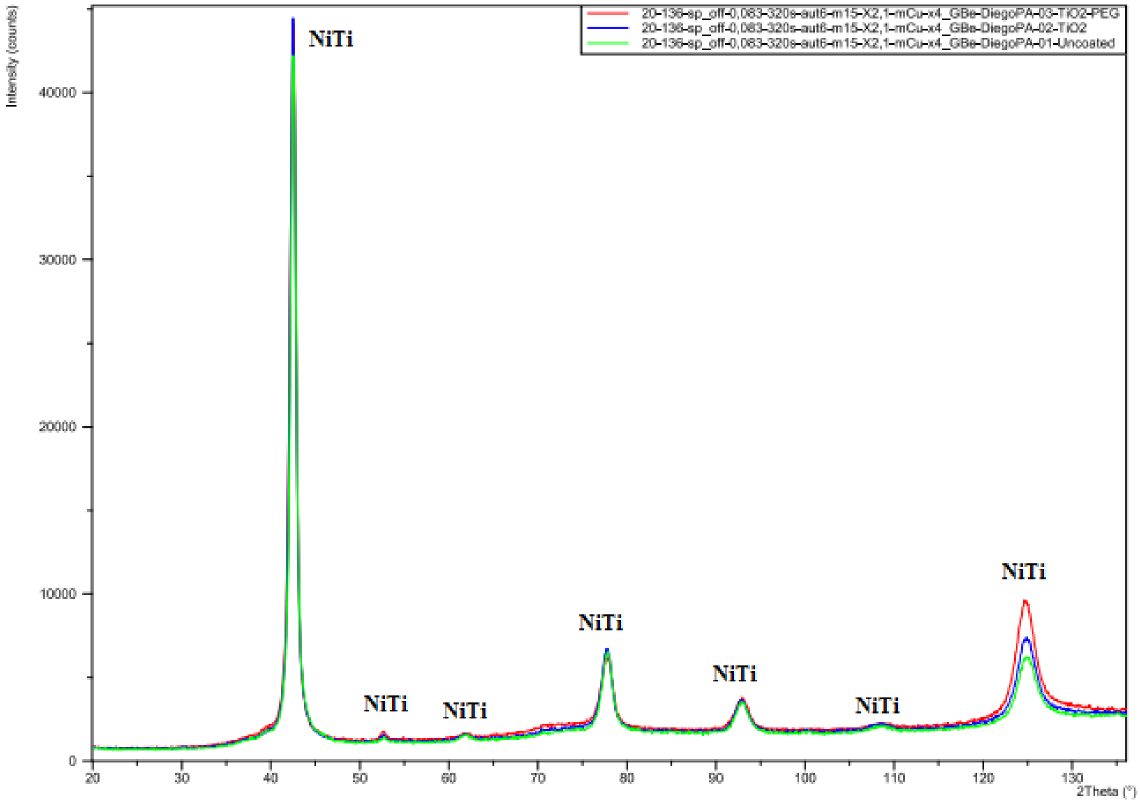

Figure 5.4 - Comparative GIXRD diffractogram for as received NiTi (green), TiO_2 coated NiTi (blue) and TiO_2 + PEG coated NiTi (red).

Etching of NiTi surface is usually accomplished using a HF and HNO_3 solution. This aggressive etching procedure removes the majority of the surface defects generated on the cold work performed with the alloy but leaves the surface with a rough finish, as showed in the work of Vojtech *et al.* (2010; Figure 5.5) who used a 4:1:5 HNO_3:HF:H_2O solution to etch superelastic NiTi wires.

In order to get a smoother surface, a less corrosive solution was chosen for the treatment. The selected solution was the 50 wt.% H_3PO_4 and 30 wt.% H_2O_2 solution proposed by Okazaki *et al.* (2013). NiTi samples were immerged in this acid at 80ºC for times from 5 to 40 minutes in order to compare surfaces. Figure 5.6 shows the secondary electron images of the samples surface after this procedure. The immersion time of 20 min was chosen as the standard after qualitative analysis of the surface topography.

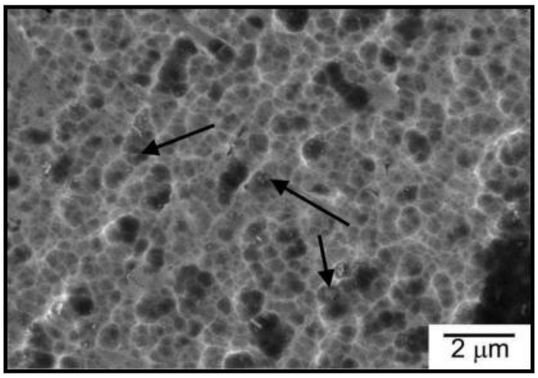

Figure 5.5– Chemically etched NiTi wire using a HNO_3+HF solution. Arrows indicate non-metallic inclusions (source: Vojtech *et al.* 2010)

According to the literature, TiO_2 film thickness deposited via dip-coating sol-gel is governed by the solution viscosity and withdraw speed (Brinker et al. 1991). The higher the withdraw speed, the thicker is the film. To obtain a thick and flexible oxide layer, deposition tests were performed using the following withdraws speeds: 4.5, 5.5, 7.5, 8.5 and 9.5 mm/s. The films emerged at 8.5 and 9.5 mm/s became too thick and cracked during drying procedures, as realized by a simple visual inspection (Figure 5.7). The withdraw speed of 7.5 mm/s was selected as the optimum one for this system, since it produced the thicker stable layer capable of sustaining a high amount of strain, as it will be detailed latter.

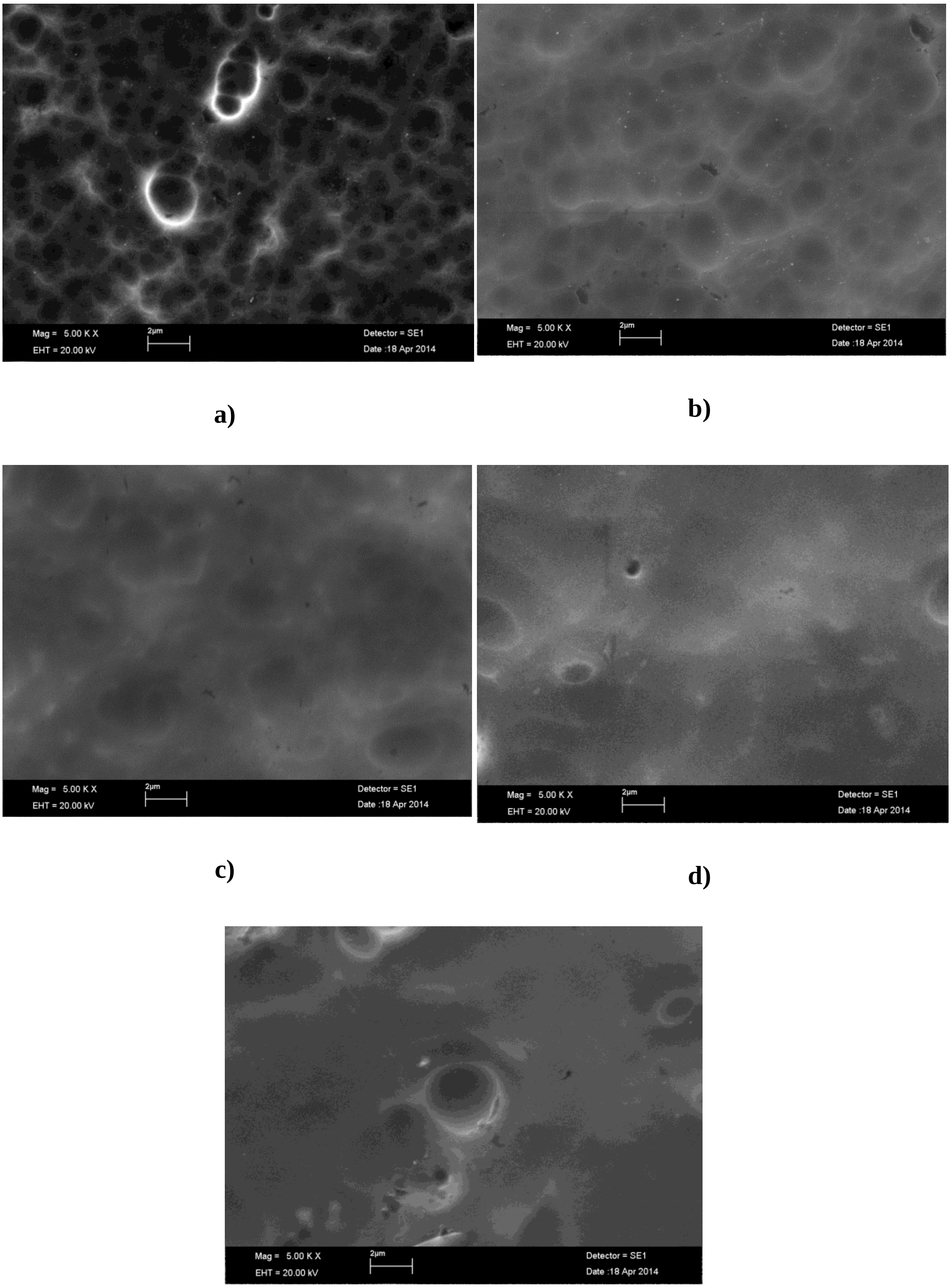

a) **b)**

c) **d)**

e)

Figure 5.6 – Comparative secondary electron images of chemically etched NiTi immerged in the acid solution for a) 5 min; b) 10 min; c) 20 min; d) 30 min; e) 40 min.

One attempt was made to improve film flexibility by changing the composition of the sol-gel solution. Polyethylene Glycol is used as a plasticizer in several systems to improve film flexibility (Vieira et al. 2011). With that in mind, a second TiO_2 sol was prepared adding polyethylene glycol (PEG 300 P.A.) in a 10:1 volumetric proportion between TIPT and PEG. The solution was stable and used to coat 5 mechanical polished NiTi strips with 7.5mm/s withdraw speed. No crystallization thermal treatment was applied to the system. The coated samples were strained and investigated by electron microscopy. Maximum tested strain achieved for the mixed TiO_2/PEG films was 2.0%, lower than the pure TiO_2 film. Mixed films presented a specific morphology with applied strains of 3.0% or over, showing cracks parallel to the tensile direction, as shown in Figure 5.8. No other attempt was made to modify precursor solution composition and the mixed produced solution was discarded.

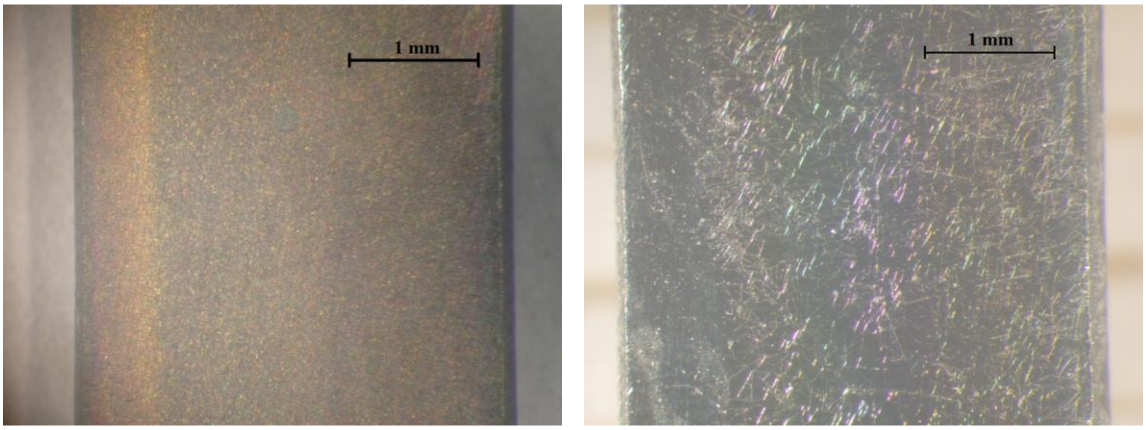

a) **b)**

Figure 5.7 - Optical image of the surface of TiO_2 coated mechanical polished superelastic NiTi alloy deposited with different withdraw speeds: a) 7.5 mm/s; b) 9.5 mm/s

With the objective of improving film biocompatibility, a third thermal treatment was proposed after deposition in order to crystallize part of the TiO_2 layer forming a nanocomposite film. Initially, three different densification treatments were attempted after the coating of chemically etched substrates at 7.5mm/s withdraw speed: 350ºC for

20 min, 500ºC for 10 min and 650 ºC for 10 min. The coated samples with amorphous films were introduced in the furnace already heated. After the densification, samples were characterized by GIXRD, SEM and three-points bending tests. Figure 5.9 shows the diffractograms of the GIXRD measurements.

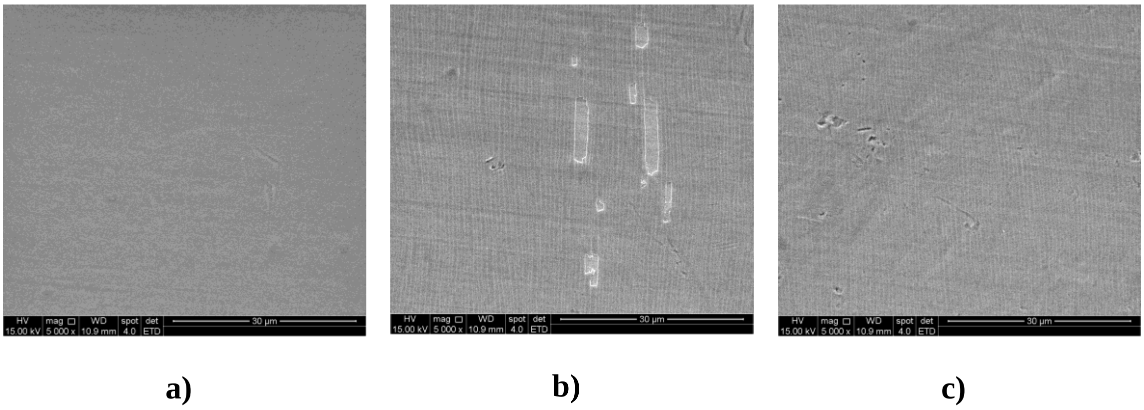

a) **b)** **c)**

Figure 5.8 – Secondary electron image of mixt TiO_2/PEG film deposited over NiTi superelastic strip with 7.5 mm/s withdraw speed a) unstrained; b) sample 1 after being 3.0% strained and c) sample 2 after being 3.0% strained

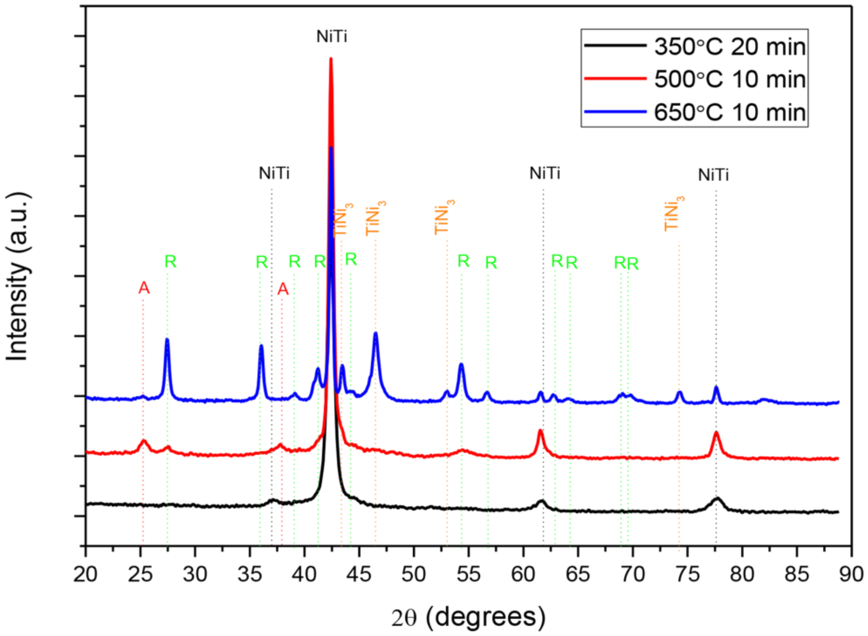

Figure 5.9 – GIXRD diffractogram of TiO_2 coated NiTi after densification treatment at indicated temperatures (insets: A - anatase; R – rutile).

No TiO_2 peaks could be observed on the sample treated at 350ºC for up to 20 min, indicating that the film was still in its amorphous state. In the sample treated at 500ºC, small peaks of anatase and rutile can be observed, indicating that the crystallization process has occurred. At 650ºC, the rutile peaks are dominant for the oxide film; however, peaks of the stable $TiNi_3$ phase can also be noticed in the diffractogram. The formation of this phase indicates a dissolution of the metastable Ti_3Ni_4 (Otsuka & Ren 2005), which implies that this heat-treating condition for the film would change the austenite-to-martensite transformation temperatures of the NiTi alloy, consequently changing its superelastic behavior, as discussed in section 3.2.1.

The coated samples treated at the temperatures above mentioned and the non-crystallized samples (dried at 110ºC for 2 hours) were divided into 4 groups in terms of the densification thermal-treatment for the TiO_2: a control group, without any densification thermal treatment (amorphous), the group treated at 350ºC for 20 min, the one treated at 500ºC and the group treated at 650ºC for 10 min. SEM images of 5 samples in each group were taken before and after they were subjected to tensile strains up to 6.4% at the surface during the three-points bending tests. Typical images are presented in Figure 5.10. Cracks and holes could be observed on the amorphous coatings (Fig. 5.10a) after tensile strains of 3.0% were applied. For samples treated at 350ºC (Fig. 5.10b), the films contained small and sparse fissures after being strained at 6.4%; however, no diffraction peaks corresponding to TiO_2 anatase or rutile could be detected in Figure 5.9. Treatment at 650ºC almost fully crystallized the oxide layer in the rutile phase, as realized by the relative intensity between TiO_2 and NiTi crystalline peaks, making the ceramic coating fragile (Fig. 5.10d), and causing the formation of stable $TiNi_3$, as noted before. The crystallized oxide layer cracked with the application of 2.0% strain. The crystallization temperature of 500ºC resulted in the optimal strain resistance, showing almost no cracks, and started the crystallization process, forming anatase and rutile TiO_2 (Fig. 5.10c). The photocatalytic and superhydrophilic effects are stronger in the anatase. A film containing this phase would present several advantages related to biocompatibility, as discussed in section 3.3.2.

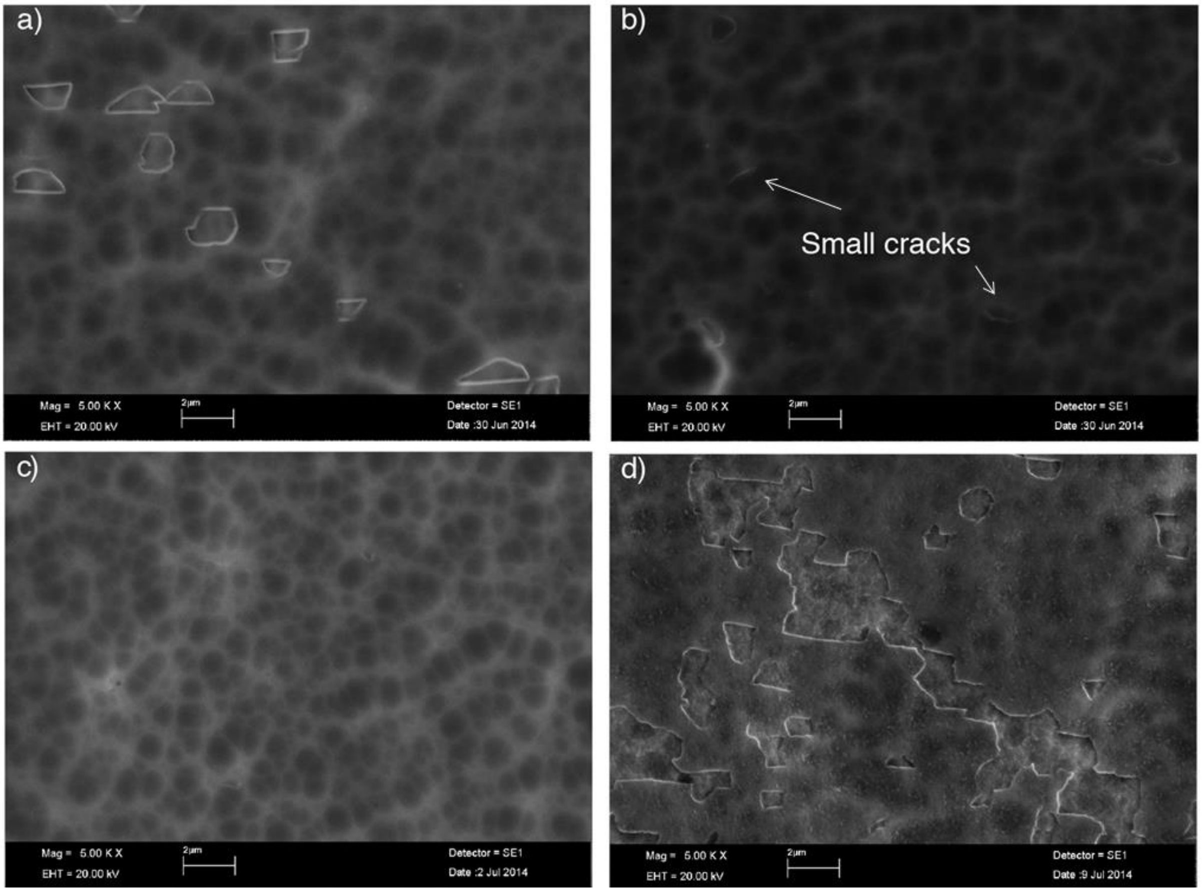

Figure 5.10 – Secondary electron topographic images of TiO_2 coated NiTi alloy after a tenfold 6.4% strain applied in three points bending tests. a) no densification treatment; b) 350ºC for 20 min; c) 500ºC for 10 min; d) 650ºC for 10 min

Since the mechanical behavior, regarding film flexibility, was similar for the samples treated at 350ºC and 500ºC, but the former presented a film in the amorphous state, a fourth densification temperature was tried in order to get a semi-crystallized oxide layer containing a higher anatase quantity, which present advantages in biological systems. Coated strips where treated at 450ºC for 30 min to achieve this objective, and the GIXRD diffractogram of one of these samples is showed in Figure 5.11. Results indicate a higher presence of rutile TiO_2 and also a greater amount of crystallized material as indicated by the relative peak size between the crystalline oxide lines and the substrate ones (the rutile crystalline peak at ~27º is more intense then the NiTi peak at ~44º). This higher amount of crystalline material should decrease film flexibility, since crystalline TiO_2 is a fragile ceramic material. Also, a peak at ~46.5º indicates the presence of the stable $TiNi_3$ phase which presents several disadvantages to the system already described.

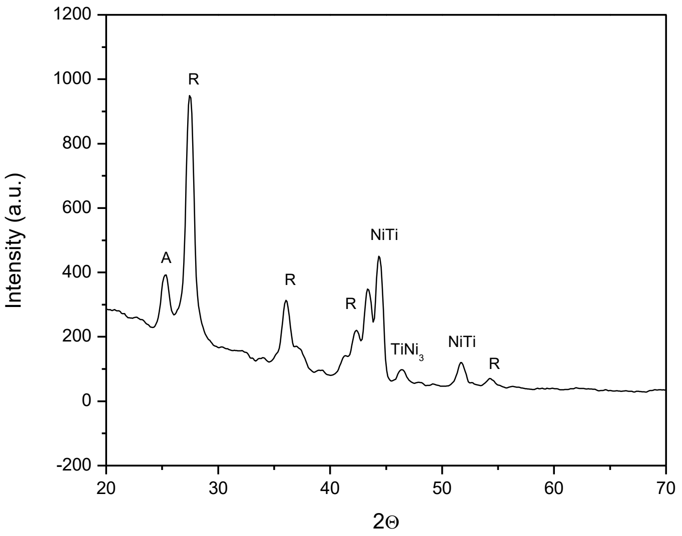

Figure 5.11– GIXRD diffractogram of TiO_2 coated superelastic NiTi strip treated at 400ºC for 30 min (insets: A – anatase; R – rutile)

Best thermal treatment was achieved at 500ºC. To optimize the crystallization, the thermal treatment at this temperature was applied changing exposition times. The GIXRD diffractogram of the tested samples are shown in Figure 5.12. As it can be observed, 5 min was not enough to initiate the crystallization of the oxide layer. At 30 minutes of exposition, the main (110) rutile peak at 27.4º is dominant in relation to the anatase (101) peak at 25.3º, showing a stronger contribution of this phase in the film. Also, the higher peaks intensities for the crystallized TiO_2 (compared to the main NiTi substrate peak) indicate a higher degree of crystallization that would weaken film flexibility, being the deformation of the porous in the amorphous part the main responsible to accommodate severe strain. For longer exposures, rutile lines are dominant for the crystalline phases of the oxide, and the formation of $TiNi_3$ start to occur. Formation of this phase will significantly change the superelastic behavior of the NiTi alloy. Also, samples treated at 500ºC for 7, 15 and 20 minutes presented a worse result regarding flexibility after three-points bending tests when compared to the ones treated for 10 min (Figure 5.13). Higher amounts of film cracks and holes can be observed in the SEM secondary electron images of the Figure 5.13, after a 6.4% strain was applied using the three-points bending machine. No GIXRD diffractograms were collected for these samples.

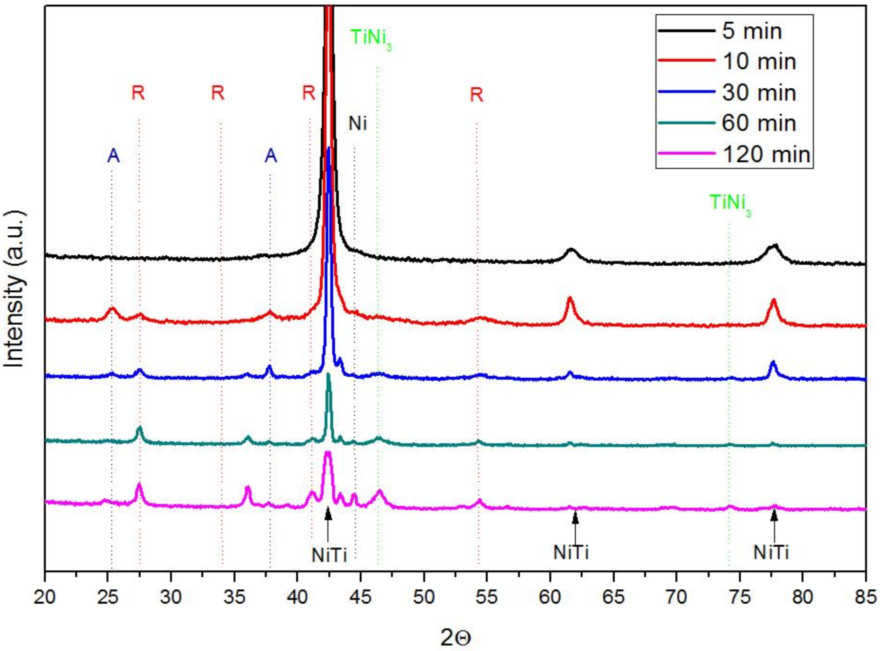

Figure 5.12 – GIXRD diffractograms of TiO_2 coated NiTi treated at 500ºC for 5, 10, 30, 60 and 120 min. A- Anatase; R- Rutile

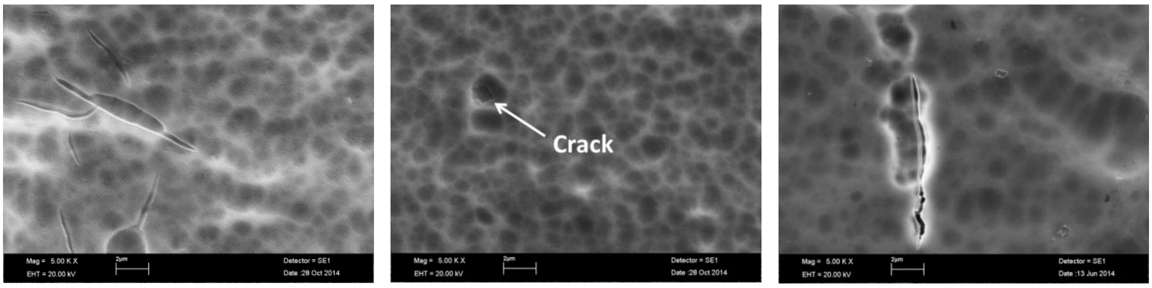

a) b) c)

Figure 5.13 – Secondary electron SEM images of TiO_2 coated NiTi strips treated at 500ºC for a) 7 min; b) 15 min and c) 20 min; after a 6.4% strain applied by three-points bending

The anatase (101) and rutile (110) peaks where used to calculate grain size through the application of the Scherrer equation (equation 4.3) after the removal of the $K_{\alpha2}$ contribution and instrument line broadening (Cullity & stock 2001). The results are shown in table V.1. The minimum crystallite size of TiO_2 anatase and rutile for the chosen treatment of 500ºC for 10 min are of the same order (~10 nm). Since Scherrer equation used to calculate these grain sizes is developed for XRD performed on powder materials and the titania peaks used are small when compared to the NiTi lines, the values presented in table V.1 are not precise, but they give a good estimate of the minimum crystallite size. This small crystallite size and a higher amount of amorphous material could better accommodate deformations, maintaining the ceramic coating flexible, with a higher tensile resistance.

Table V-1- Evolution of the minimum crystallite size of TiO_2 anatase and rutile phases on coated NiTi samples treated at 500ºC

Time (min)	**Anatase (101)**			**Rutile (110)**		
	θ (º)	**β (rad)**	**L (nm)**	**θ (º)**	**β (rad)**	**L (nm)**
5	-	-	-	-	-	-
10	25.31	0.95	10.9	27.49	0.97	10.8
30	25.21	1.17	8.6	27.47	0.77	13.9
60	25.00	1.05	9.7	27.45	0.61	18.7
120	24.80	0.68	16.0	27.45	0.58	19.9

In order to test if the chosen thermal treatment for partial crystallization of the oxide layer would change de superelastic behavior of the samples, 5 uncoated and chemically etched samples and 3 coated strips were tested using three-points bending to record force versus strain curves and study its mechanical behavior. The average curves are presented in Figure 5.14.

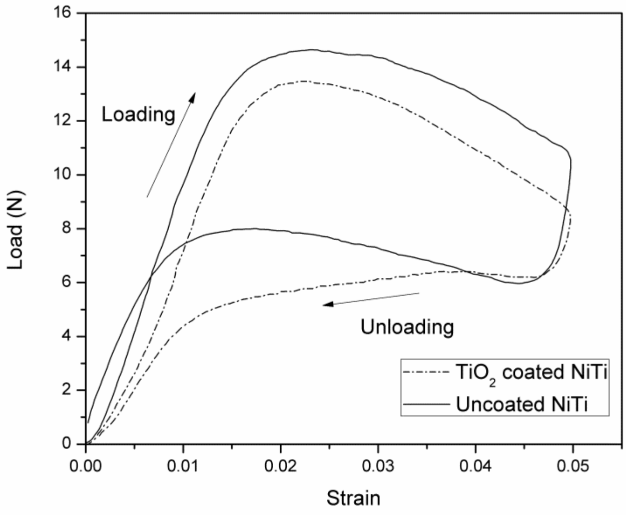

Figure 5.14 – Force x strain curves obtained by three-points bending for uncoated and TiO_2 coated superelastic NiTi strips

The thermal treatment at 500ºC for 10 min was not enough to change the superelastic property of the NiTi alloy. All tested samples showed a total strain recuperation at room temperature (25 ± 2ºC) in the three-points bending tests (Figure 5.14). The characteristic deformation plateau of SMA arising from the emergence of stress-induced martensite started at similar forces for the coated and uncoated samples (around 14 N). Reduction in the loading force in the strain plateau (strains between 0.02 and 0.05) was caused by sliding of the samples on the support pins of the bending test machine for high deformations. A small decrease in the TiO_2 coated strips stiffness can be noticed by higher deformations at lower strengths in the initial stages of the loading. Calorimetry experiments that will be discussed later in this chapter showed that the martensitic and austenitic transformation temperatures were not significantly changed by the selected thermal treatment. The reduction in the alloy stiffness can then be explained by an internal stress relief generated by the thermal treatment that was not enough to precipitate Ti_3Ni_4 or form other phases (as it can be deducted by the maintenance of the transformation temperatures) but can annihilate lattice dislocations.

In summary, after testing individually each deposition parameter (solution composition, withdraw speed, thermal treatment), the optimized relation between TiO_2 film flexibility and thickness, that will be related to the biocompatibility by the decrease in the surface Ni concentration, was achieved by dip-coating sol gel with a 0.4M TIPT alcoholic solution with pH 1.27 and 0.82 water to precursor ratio, with a withdraw speed of 7.5 mm/s, followed by a threefold thermal treatment at 100ºC for 45 min in a humid atmosphere, 110ºC for 2 hours in a dry atmosphere and 500ºC for 10 min in a dry atmosphere. This deposition route was used to coat several NiTi superelastic strips which passed through a chemical etching in a 50 wt.% H_3PO_4 and 30 wt.% H_2O_2 aqueous solution at 80ºC for 20 minutes. All the characterizations described on the next sections were performed using those samples.

5.2. Characterization of the developed TiO_2 film

5.2.1. Roughness characterization

AFM images using the "tapping" mode were acquired on a 40 x 40 μm^2 area of the etched NiTi substrate and the coated samples, in order to characterize the reduction of the surface roughness caused by film deposition. The 3D topographic plots of these regions are showed in Figures 5.15 and 5.16, respectively.

The root mean squared (rms) values for the uncoated and coated samples were 312.7 and 199.6 nm, respectively in the selected region. The reduction of roughness seems to be more evident for the polished samples, as one can observe in Figure 5.3. However, this small reduction should be enough to lower the friction coefficient of the coated samples. In dental applications, for instance, a smoother surface with a low friction is desirable. For the endodontic instruments, it would reduce the chance of torsional overload and the torque required to shape the root canal. In orthodontics, the low friction between arch wire and brackets could facilitate the correct conformation of dentition (Wei *et al.* 2011, Varela *et al.* 2014). Also, as it was discussed in section 3.3.2, the surface roughness increases the protein and cellular adhesion, but the TiO_2 surface should be more adequate than the NiTi one because of a smaller Ni surface concentration.

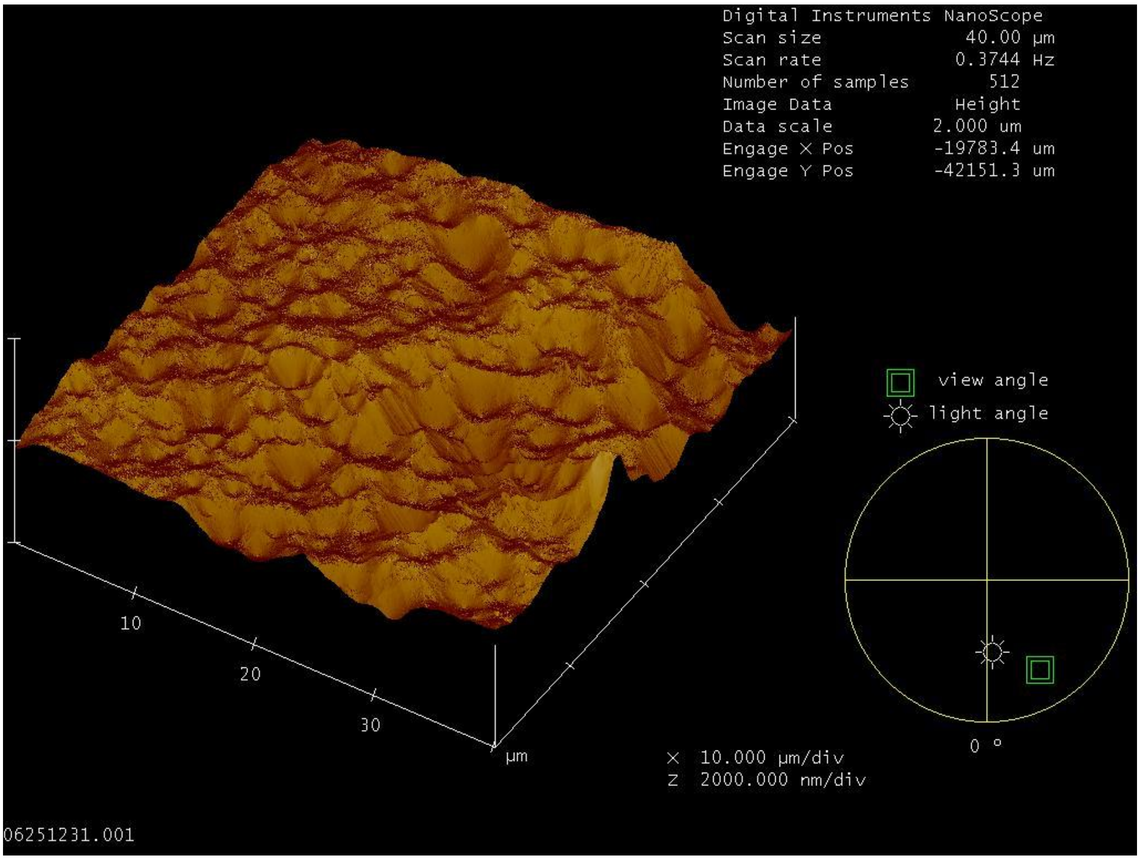

Figure 5.15 – Topographic AFM image of chemically etched NiTi

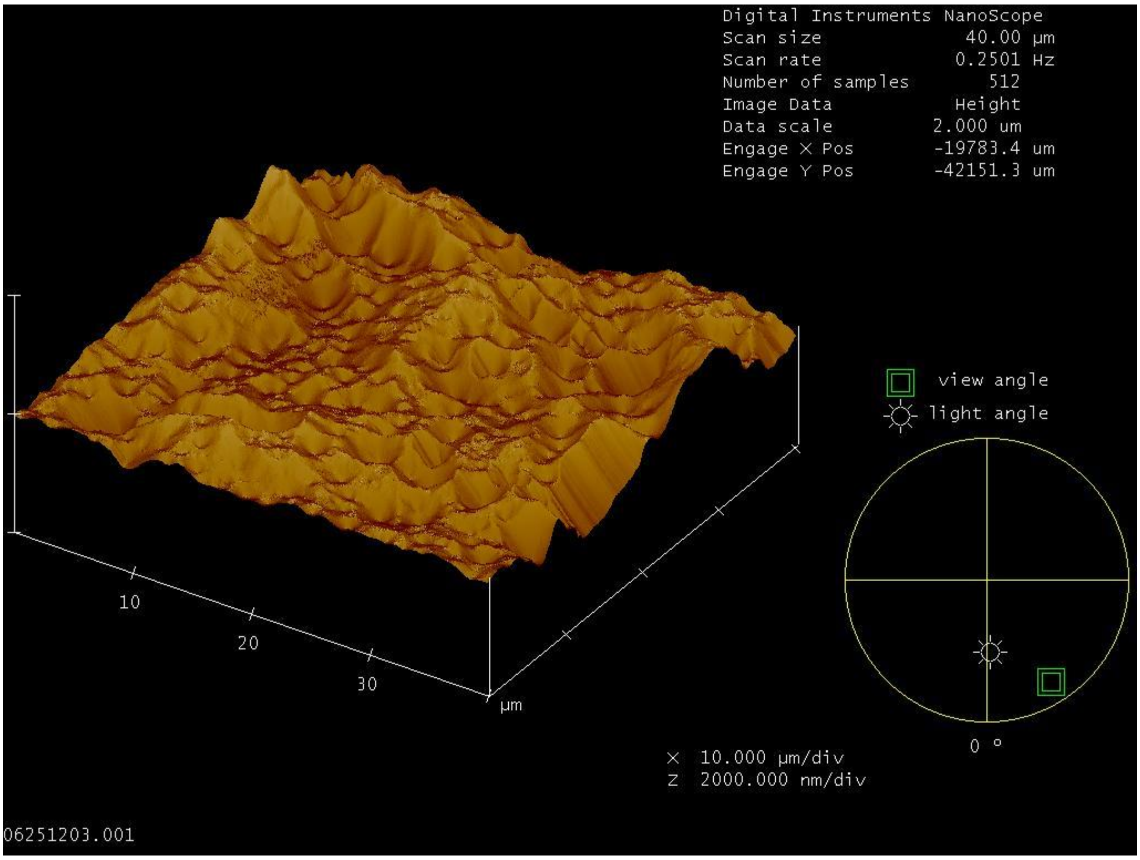

Digital Instruments NanoScope
Scan size 40.00 µm
Scan rate 0.2501 Hz
Number of samples 512
Image Data Height
Data scale 2.000 um
Engage X Pos -19783.4 um
Engage Y Pos -42151.3 um

X 10.000 µm/div
Z 2000.000 nm/div

06251203.001

Figure 5.16 – Topographic AFM image of TiO_2 coated NiTi

5.2.2. Surface chemical analysis by XPS

XPS spectra of as received, chemically etched and TiO_2 coated NiTi with electron collection angle of 90º and 30 º are showed in Figures 5.17 to 5.22. No contamination other than the carbon can be found on the survey spectra of the tested samples, indicating a high purity of the oxide coating. The values used for the peaks decomposition of titanium and oxygen are presented in table V.2 (Armitage & Grant 2003, Houmard 2009, Bhosale *et al*. 2012). The main component for the titanium decomposition on all spectra was the Ti^{4+} $2p_{3/2}$ and Ti^{4+} $2p_{1/2}$ doublet peak at 458.3 eV and 464.0 eV, respectively; however, contributions of the Ti^{3+} and Ti^0 peaks can also be observed, and these are higher for the spectra of the uncoated samples. The presence of the Ti^{4+} doublet with a difference of 5.7 eV confirms the main oxidation state of Ti and the dominant presence of TiO_2 on the substrate and coated sample surfaces (Acik *et al.*

2012, Bhosale *et al.* 2012). It is also evident that the natural passive oxide layer is rapidly formed soon after etching the alloy, since the experiment was performed a few minutes after this surface treatment.

The ratios between Ti^0 $2p_{3/2}$ and $Ti^{4+}2p_{3/2}$ for the TiO_2 coated and etched samples with a 90º collecting angle were 0.03 and 0.09, respectively, indicating that the contribution of the metallic Ti at 454.2 eV is stronger in the chemically etched substrates. This Ti^0 signal most likely arises from the NiTi substrate and is evidence of the small thickness of the natural oxide layer and thus indicates a lower biocompatibility of the uncoated alloy, since a higher concentration of Ni on the surface would increase its release rate.

Transitional oxides as Ti_2O_3 are present on all samples, as realized by the Ti^{3+} signal contribution. The Ti^{4+}/Ti^{3+} ratios for the as received, chemically etched and coated samples are 7.1, 7.5 and 12.0 respectively. This result shows a higher purity and uniformity of the TiO_2 layer for the coated samples. Being more stable, TiO_2 presents a smaller value of free energy when compared with Ti_2O_3 and so, a higher protective capacity. The higher concentration of the stable oxide on the coated samples as indicated by the higher Ti^{4+}/Ti^{3+} ratio is translated as a higher corrosion resistance and biocompatibility for these samples.

Table V.2- Titanium and oxygen XPS fitting parameters (BE - binding energy; FWHM - full width at half-maximum; L/G - Lorentzian to Gaussian ratio; M - metal)

Line	**BE (eV)**	**FWHM (eV)**	**L/G**
Ti^{4+}	458.5 ± 0.2	1.5 ± 0.1	0.1
Ti^{3+}	456.5 ± 0.3	1.7 ± 0.1	0.1
Ti^0	454.5 ± 0.3	1.7 ± 0.1	0.1
O - M	530.0 ± 0.2	1.6 ± 0.1	0.1
OH - M	531.4 ± 0.2	1.6 ± 0.1	0.1
O - C	532.5 ± 0.3	1.6 ± 0.1	0.1

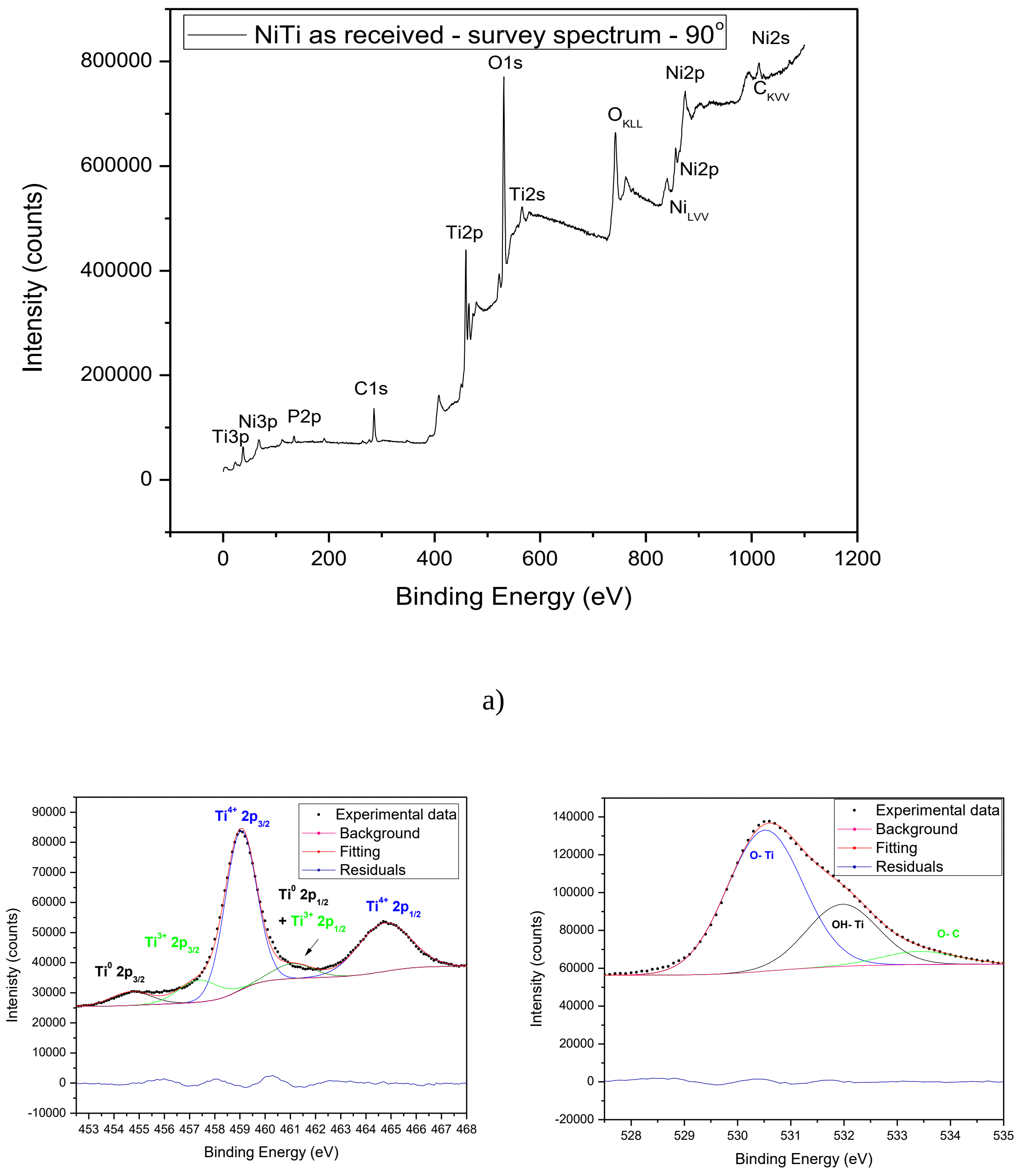

a)

b)

c)

Figure 5.17 – XPS spectra of as received NiTi superelastic alloy collected at 90º. a) Survey spectrum; b) Ti peak decomposition; c) O peak decomposition

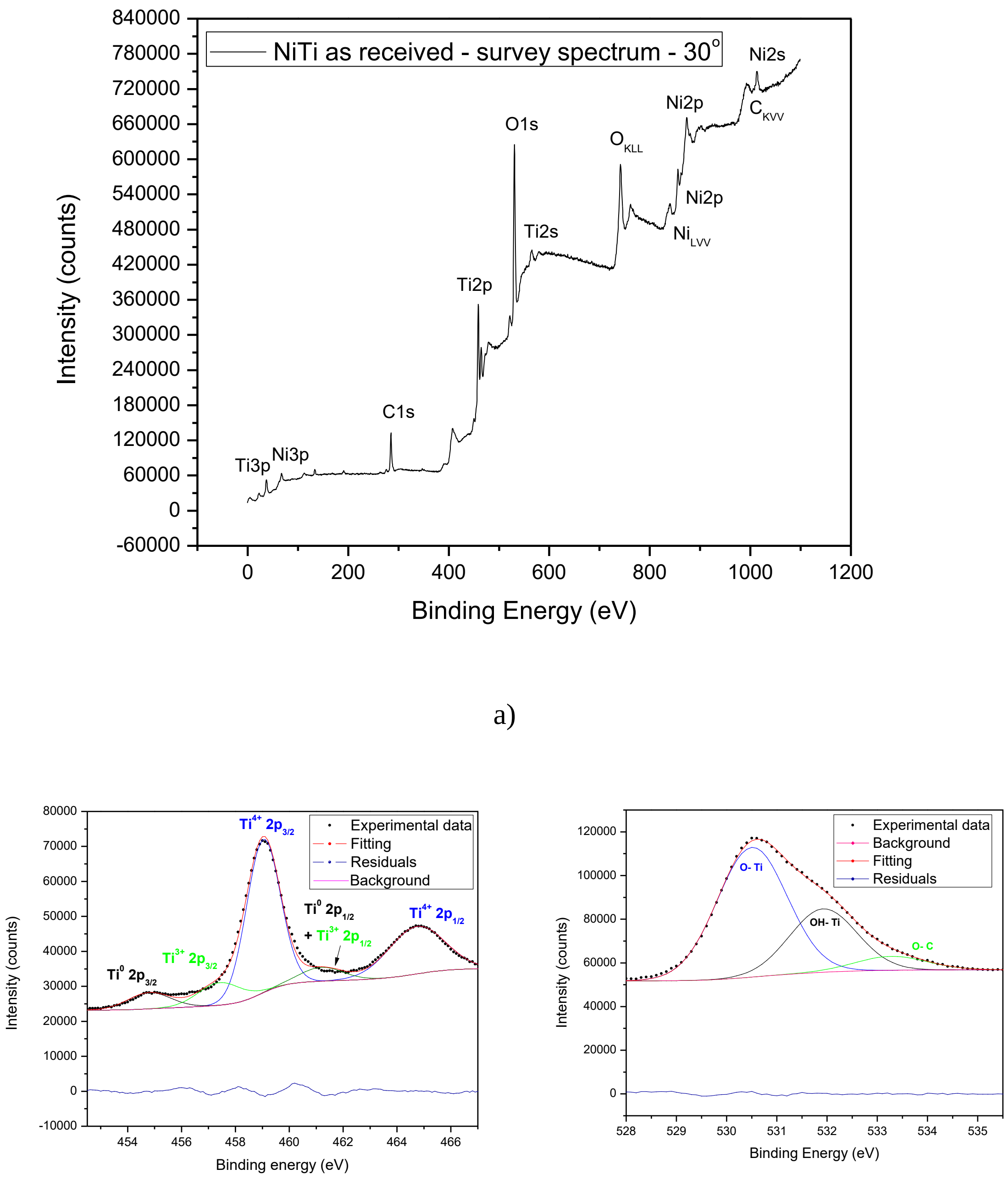

a)

b)

c)

Figure 5.18 – XPS spectra of as received NiTi superelastic alloy collected at 30º. a) Survey spectrum; b) Ti peak decomposition; c) O peak decomposition

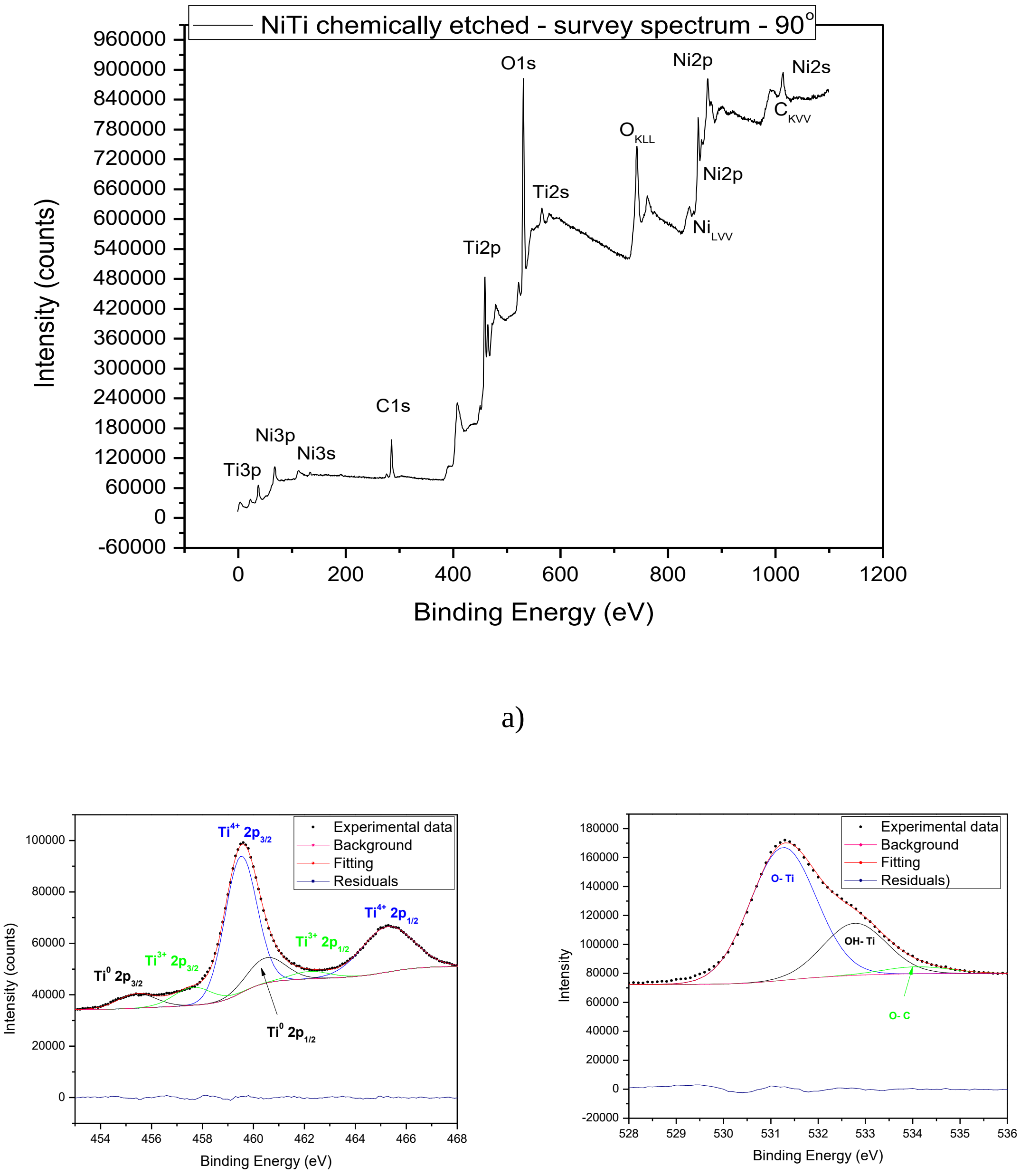

a)

b)

c)

Figure 5.19 – XPS spectra of chemically etched NiTi superelastic alloy collected at 90º. a) Survey spectrum; b) Ti peak decomposition; c) O peak decomposition

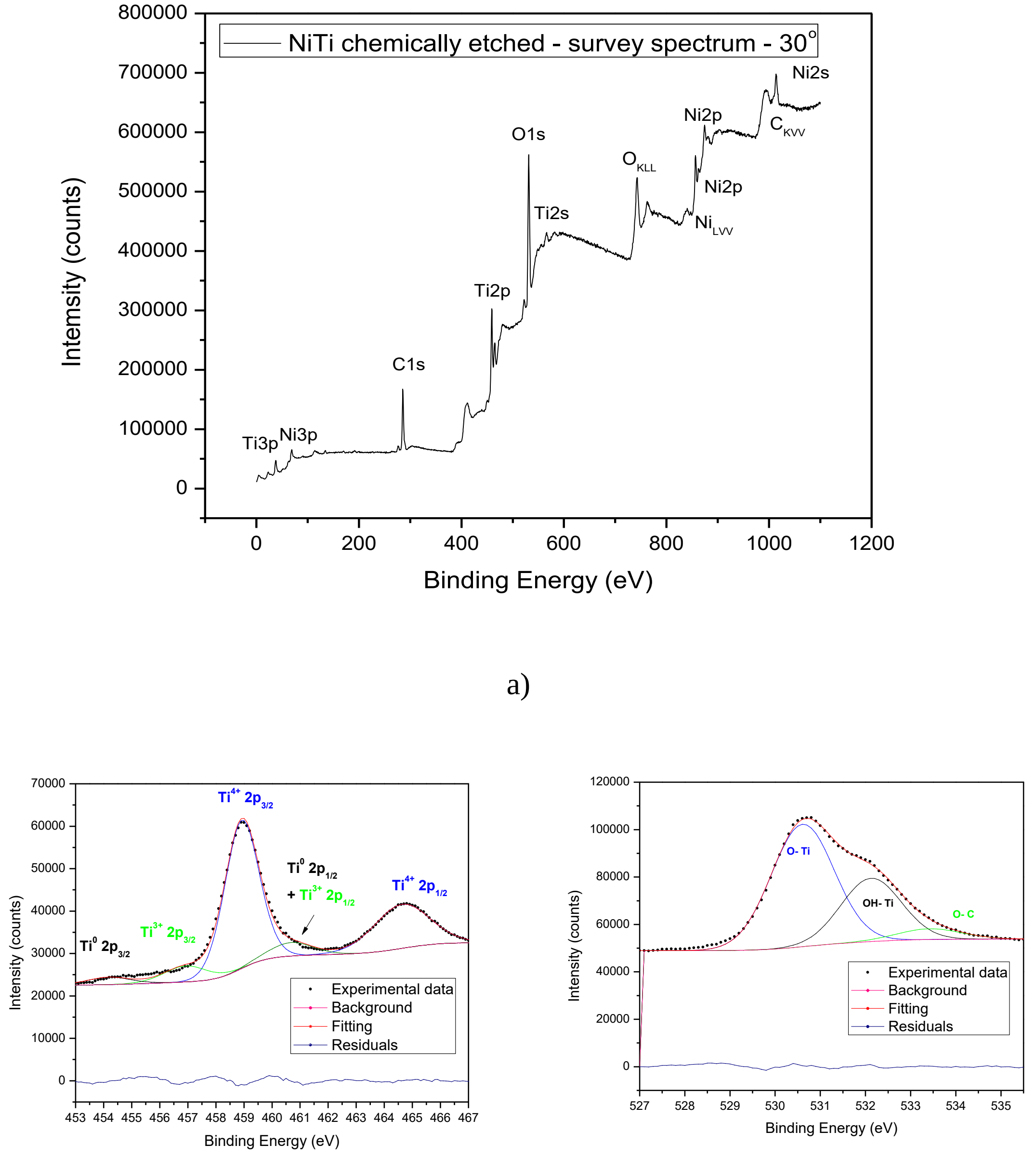

a)

b)

c)

Figure 5.20 – XPS spectra of chemically etched NiTi superelastic alloy collected at 30º. a) Survey spectrum; b) Ti peak decomposition; c) O peak decomposition

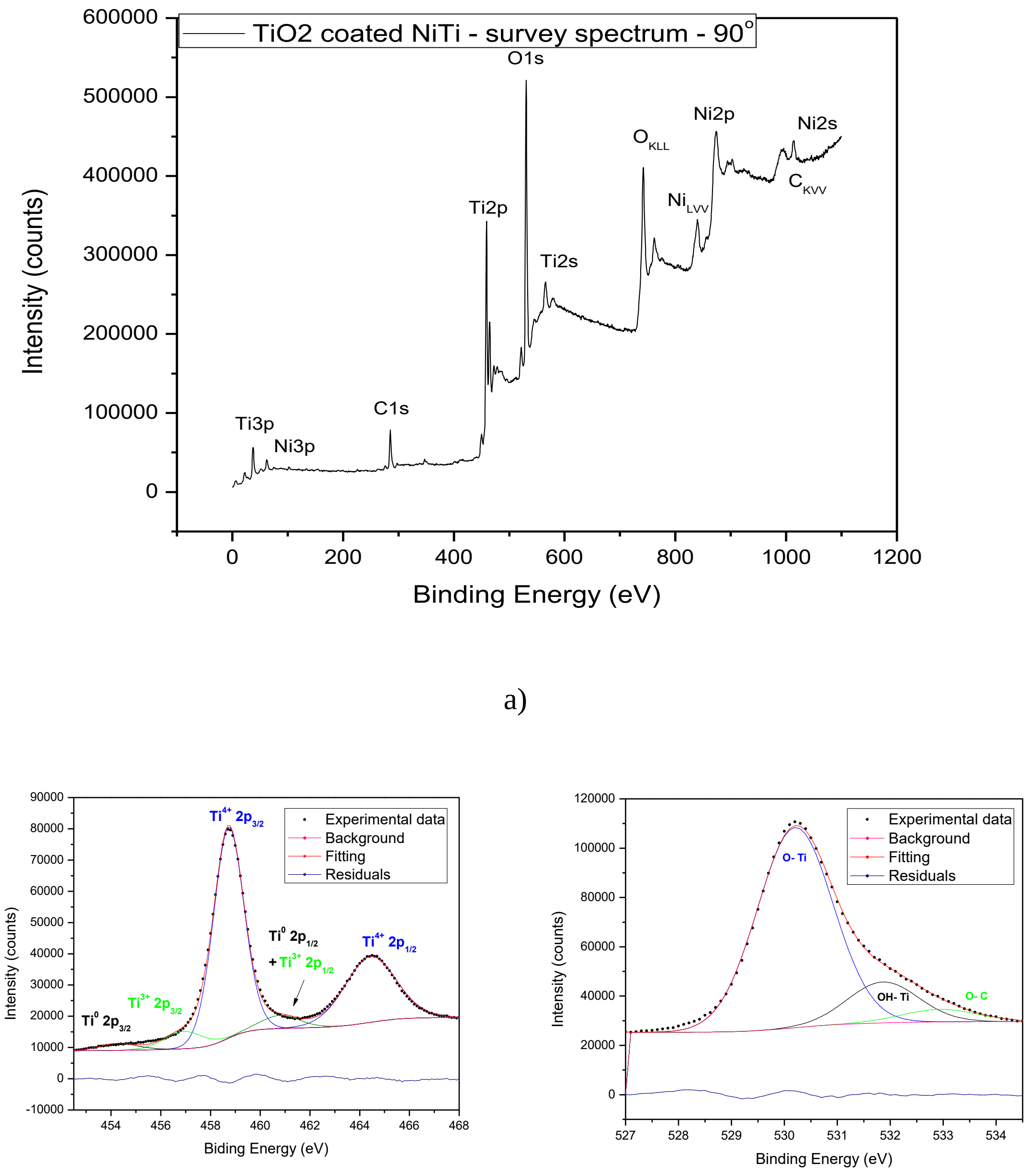

a)

b)

c)

Figure 5.21– XPS spectra of TiO_2 coated NiTi superelastic alloy collected at 90º. a) Survey spectrum; b) Ti peak decomposition; c) O peak decomposition

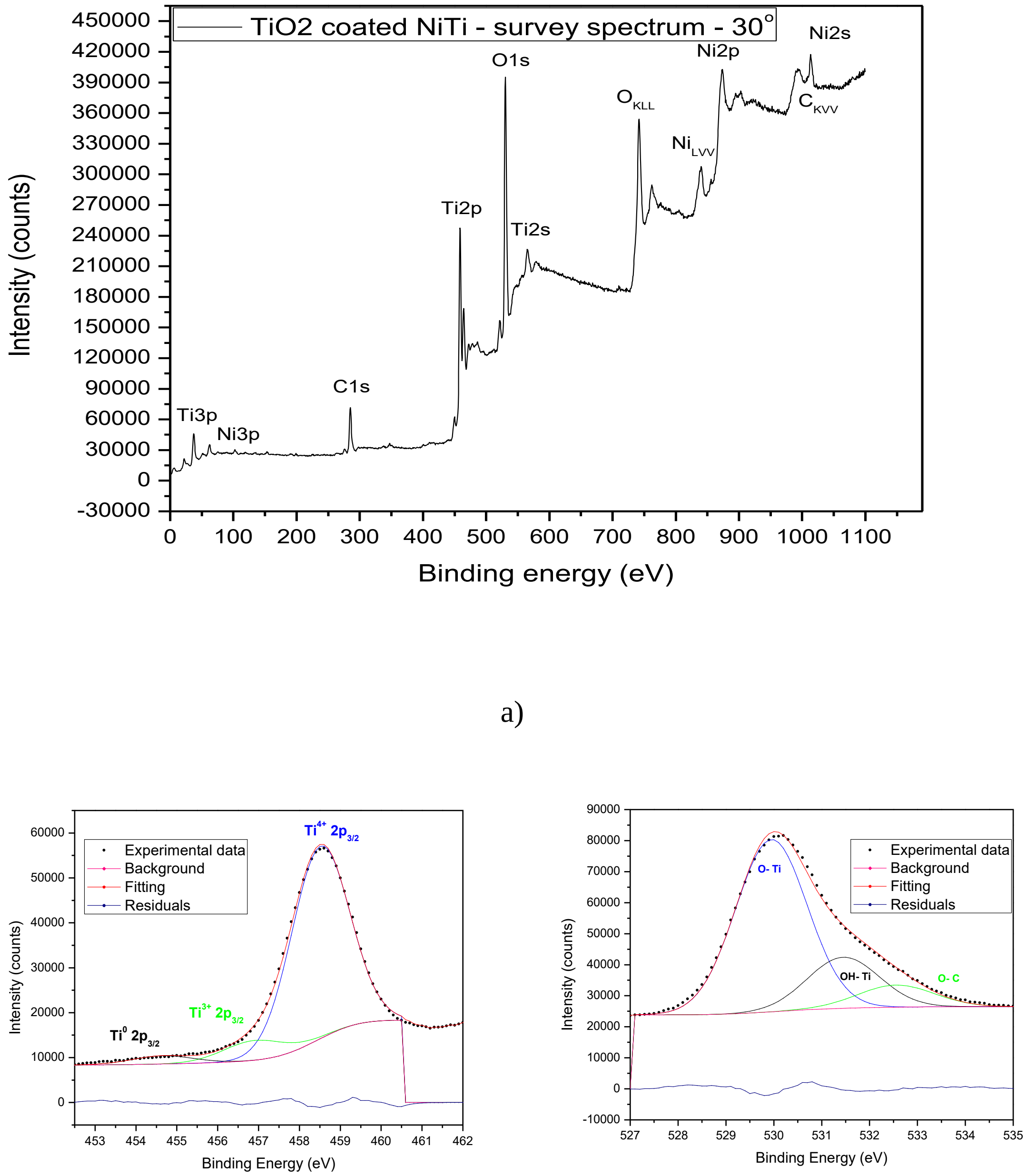

a)

b)

c)

Figure 5.22 – XPS spectra of TiO_2 coated NiTi superelastic alloy collected at 30º. a) Survey spectrum; b) Ti peak decomposition; c) O peak decomposition

The main contribution in the oxygen deconvolution was the O^{2-} component at 530.1 eV related to the oxygen linked to a metal atom and represented by O-Ti in the spectra (Figures 5.17 to 5.22) and by O-M in table V.2. This strong signal also indicates the main presence of the TiO_2. However, a strong component of the decomposition was assigned to hydroxyls bonded to metal, indicated by OH-Ti in the Figures. This component is arriving from non-completely and condensed $Ti(OH)_4$ molecules from hydrolyzed TIPT and also from the presence of small quantities of $Ni(OH)_2$ on the surface (Armitage & Grant 2003). The O-Ti/OH-Ti ratios for the as received, etched and coated samples were 2.3, 2.6 and 5.0, respectively, showing again the higher purity of the oxide layer over the deposited samples.

Ni surface concentration on NiTi alloy is related to the metal biocompatibility, as described in section 3.2.2. A low value of this element on the material surface is desirable to decrease its release. Figure 5.23 plots the Ni concentration calculated using the area of the main peaks of each element in the XPS spectra using the equation (4.5). The decrease in the surface Ni concentration observed in the graphic for the coated samples is associated with the increase in the thickness of the Ti oxide surface layer. This very low Ni concentration on coated samples surface will significantly reduce the release of this element on the blood stream, possibly preventing the triggering of allergenic or carcinogenic reactions.

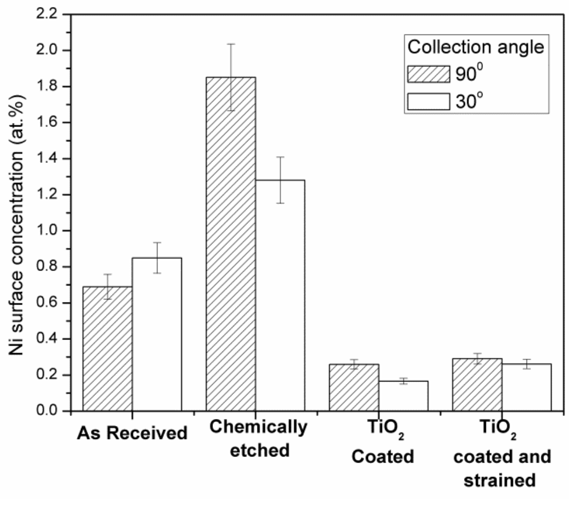

Figure 5.23 – Ni surface concentration for coated and uncoated NiTi alloy

5.2.3. Raman cartography

The results from the Raman cartography are presented in Figure 5.24. For each point on the map, the experimental spectrum was fitted as a linear combination of the reference spectra of amorphous, anatase, and rutile TiO_2, extracted from specific points of the sample. The phase maps were generated with the normalized coefficients of the best fit for each spectrum. One example of the fitting is showed in Figure 5.25. The reference spectrum of anatase shows peaks at 147, 201, 370, and 640cm^{-1}. For the rutile, two main peaks at 445 and 617cm^{-1} can be observed, and no specific peak was detected at points where only the amorphous TiO_2 was present (Figure 5.25). The peak position and width (FWHM) were calculated using Renishaw WIRE 3.0 software for the E_g vibration mode of anatase (~147 cm^{-1}).

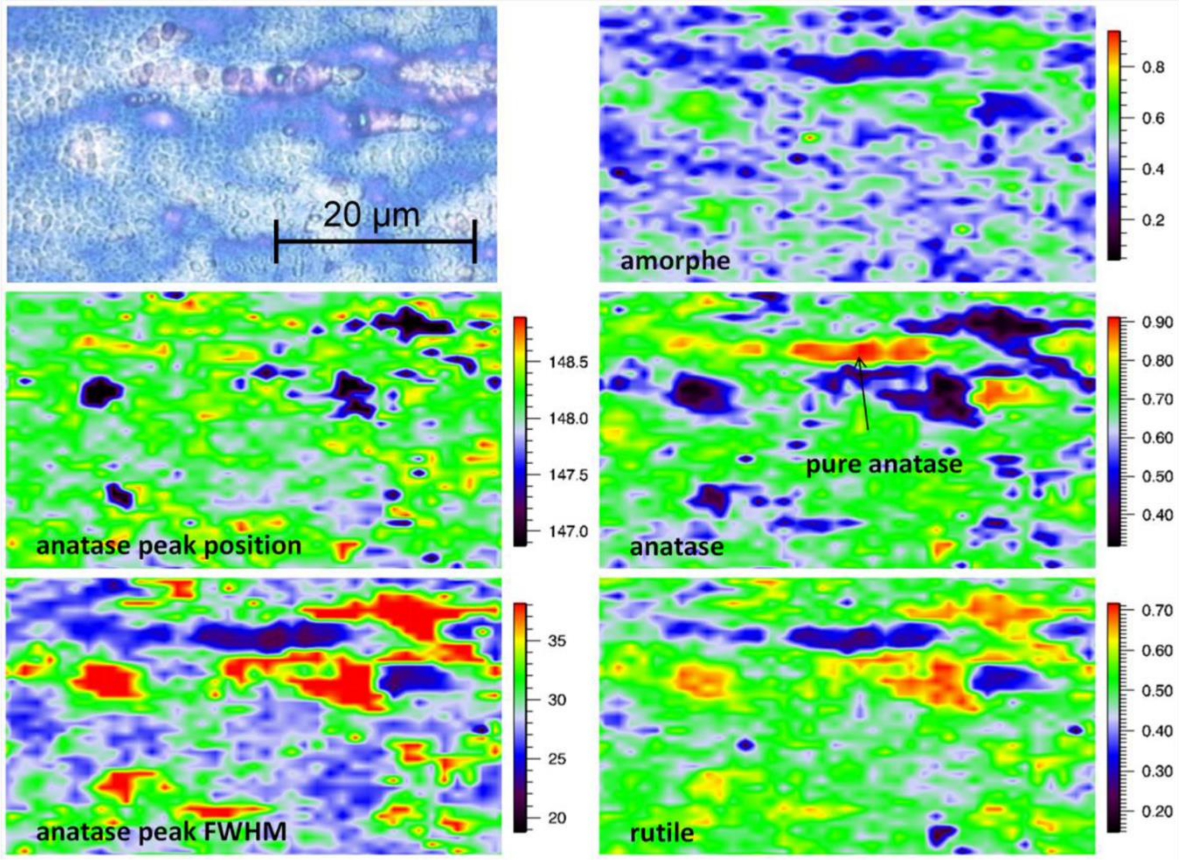

Figure 5.24 – Raman cartography over a 35 x 50 µm^2 area of a TiO_2 coated NiTi alloy treated at 500ºC for 10 min

The Raman images indicate that the basic constitution of the coated samples treated at 500ºC for 10 min was a mixture of amorphous, anatase, and rutile TiO_2; however, small regions containing a single phase were occasionally detected (as indicated for the anatase in Figure 5.22). The reference spectra were acquired in these regions. For the entire film, the main peak of E_g anatase was wide and shifted to higher frequencies, compared with the normal $143 cm^{-1}$ value (Davidsdottir *et al.* 2014). Phonon confinement in nanocrystalline grains and lattice strain are usually the main reasons for these shifts and line broadenings (Georgescu *et al.* 2012). However, Raman images acquired on strained samples showed no significant change in the mean spectrum, eliminating the hypothesis that the shift in the main peak of anatase could be induced by lattice strain. Thus, the peak shift should be caused mainly by phonon confinement due to the nanometric size of the crystallites. This finding is consistent with the XRD results (Table V.1) and TEM measurements that will be described later.

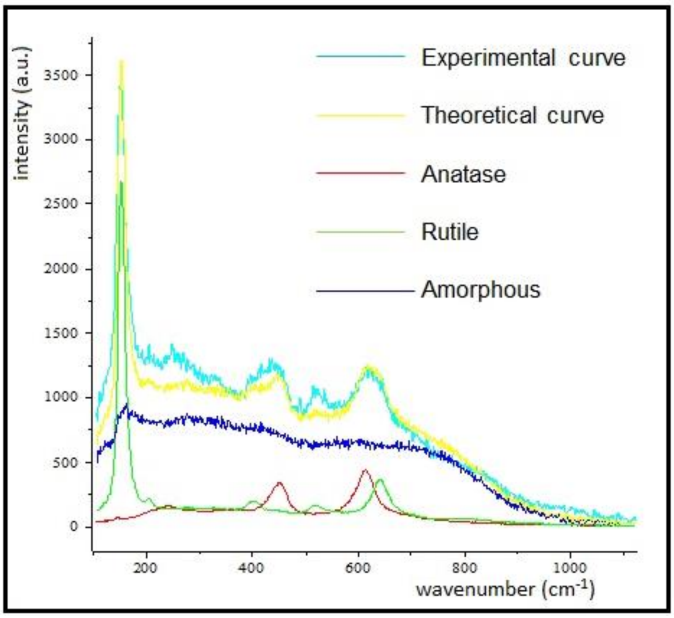

Figure 5.25 – Raman curve fit and anatase, rutile and amorphous reference spectra used for the decompositions

5.2.4. Cross section analysis of coated samples using TEM

A virtual dark-field (VDF) TEM image together with the phase and orientation maps of the cross-section of a coated specimen heat-treated at 500ºC for 10 min are presented in

Figure 5.26. The diffuse diffraction rings of the amorphous part of the film were selected to highlight the difference between denser interfacial region and the amorphous upper layer. The images reveal a ~100 nm bilayer film with anatase and rutile crystals on the alloy/film interface and amorphous TiO_2 on the extreme top surface.

The first 50 nm on the substrate interface is composed of crystals of anatase and rutile, 10–50 nm in diameter, which agrees with the results of the GIXRD presented in table V-1. The presence of these crystals are highlighted by the ASTAR images and is showed in the phase and orientation maps of the region (Figure 5.26a and 5.26b, respectively). The map also revealed a slightly dominant presence of rutile (blue color) compared with anatase (green color) in Fig. 5.26a for the first 50 nm. These results, together with the GIXRD diffractogram showed in Figures 5.9 and 5.12 suggest an epitaxial influence of the substrate favoring the rutile phase transformation. The lattice mismatch between rutile TiO_2 and the B2 phase of NiTi is small (2.1%), mainly when compared with the mismatch among anatase and the cubic phase (19.2%). This small difference can catalyze the rutile formation and explain the higher quantity of this phase showed in Figure 5.26a and its formation at 500ºC.

To confirm this epitaxial influence of the substrate, the transitional phase temperature of the TiO_2 powder obtained by drying the precursor solution at 60ºC was measured by DSC and the result is shown in Figure 5.27. The heating rate used for this experiment was 10ºC/min from room temperature to 600ºC. The main objective of this experiment was to check if rutile is formed at 500ºC without the influence of the substrate. The heat flow curve shows the peak of anatase transition at 370ºC, but no characteristic peak for the rutile transformation. A second heating with the same samples showed no peaks indicating the total transformation of the TiO_2 in anatase on the first run. This result corroborates with the affirmation about the epitaxial influence of the substrate on the rutile formation. Without the presence of the substrate, the oxide did not changed to the rutile phase for temperatures smaller than 600ºC.

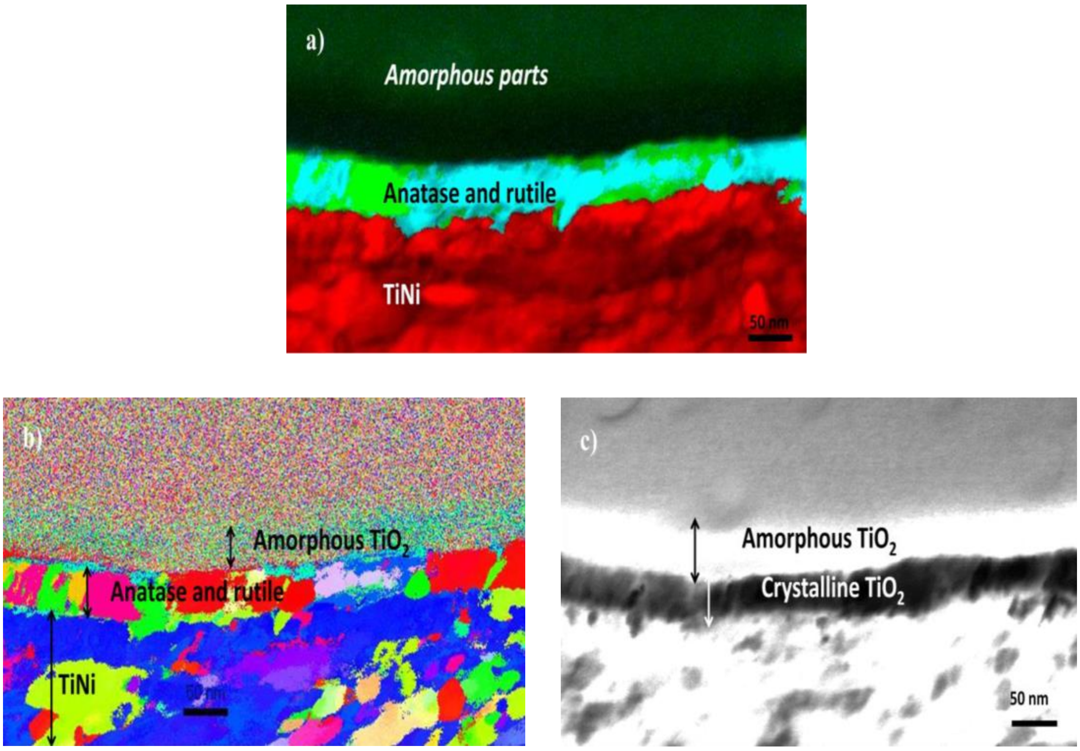

Figure 5.26 - a) Phase map, b) orientation map, and c) virtual-dark-field TEM images of the cross-section of TiO_2-coated NiTi with thermal treatment at 500ºC for 10 min

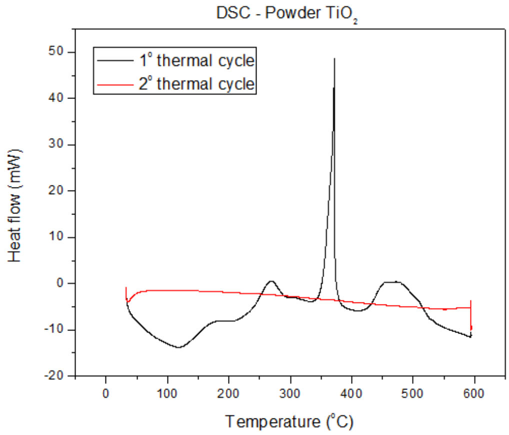

Figure 5.27 – DSC result for powder TiO_2 obtained by drying the sol-gel solution

The crystalline dense layer formed at the film/alloy interface will act as barrier for the diffusion of Ni from the rich concentrated sub-layer to the surface, reducing the possibility of Ni release and thus increasing the alloy biocompatibility. On the top of this crystalline layer, another 50 nm of amorphous TiO_2 can be observed. Electron diffraction of that region reveals no long-range order, confirming the amorphous nature of this cover. This porosity is fundamental for improving film flexibility, being the deformation of the mechanism of the film to accommodate the severe strains imposed on superelastic materials.

Bright-field TEM images and EDS mappings of the cross section of the coated sample treated at 500ºC for 10 min are presented in Figure 5.28. The substantial drop of the Ti concentration, followed by the marked drop in the concentration of oxygen on the amorphous part of the film indicate a high porosity degree of the outer surface, which should be essential for the elasticity of the ceramic coating and can be easily explained by the sol–gel deposition method. The EDS mapping of Ni illustrates the diffusion of this element from the alloy into the film; however, as previously observed by XPS (Figure 5.23), the thermal-treatment conditions were appropriate to prevent Ni atoms from arriving at the surface, which would compromise the biocompatibility of the material. As mentioned, the Ni atoms became “stuck” at the crystalline layer of the film.

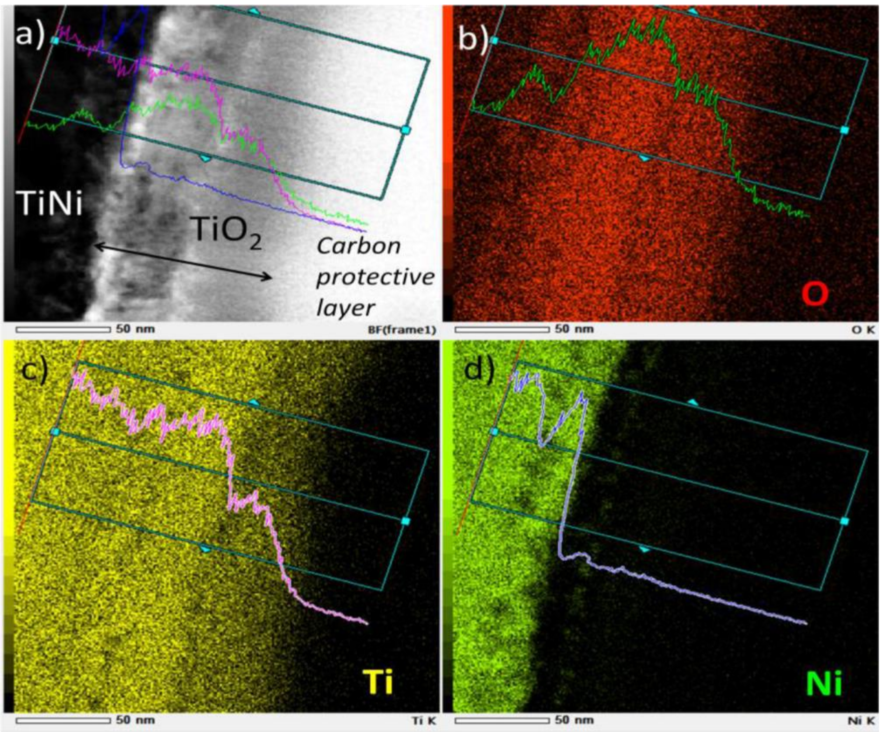

Figure 5.28 - TEM bright field image of TiO_2-coated NiTi unstrained sample (top left), and EDX mappings for O, Ti, and Ni K_α

5.3. Coating application on NiTi endodontic instruments model RaCe

For a practical application of the deposition route described in section 5.1, 16 NiTi endodontic instruments model RaCe 25/0.06 were coated with the flexible TiO_2 film. The main objectives for the coating were to improve instrument corrosion resistance, fatigue life and cutting efficiency. The RaCe 25/0.06 instruments were chosen as substrates because their high caliber (0.25 mm) make them more susceptible to fracture by fatigue (Melo *et al*. 1999, Bahia & Buono 2005) and also because the instrument has an electropolished surface which favor the formation of a smoother and continuous film. For the comparative analyzes, the samples were divided into three groups: instruments as received from the factory (AR), TiO_2 coated instruments (CI) and thermally treated instruments (TT) which passed through the same thermal treatment required to coat the CI samples but without the sol-gel film.

5.3.1. Surface characteristics of the instruments

Surface secondary electron images of coated and uncoated instruments are shown in Figure 5.29. The coated surface is not completely smooth as it would be the ideal for corrosion protection. Small and sparse fissures on the TiO_2 layers resulting from thicker layers in these curved surfaces can be observed with a magnification of 5000x, mainly next to cutting edges (Figure 5.29c) but the instrument surface is almost fully coated. These small fissures will expose the substrate alloy to the environment which could lead to a reduction in corrosion resistance and induce crevice corrosion as it will be realized by an equal breakdown potential in CPP corrosion tests in NaClO that will be better analyzed in section 5.3.4.

5.3.2. The phase transition temperatures of the instruments

The active part of 3 endodontic instruments of each group (AR, CI and TT) was cut and submitted to DSC analysis. Best results were obtained with 5 mg samples cut next to instrument shaft. Due to high internal tensions at the tip caused by machining this low diameter part, DSC curves using instrument point showed a mixture of several small transformation peaks making it difficult to analyze the results. The curves of the samples cut next to the shaft are presented at appendix B and show the normal phase transformation behavior of superelastic NiTi alloys. The martensitic phase transformation pass first through the R-phase (smaller and wider peak), followed by a definite exothermic peak for the B19' conversion.

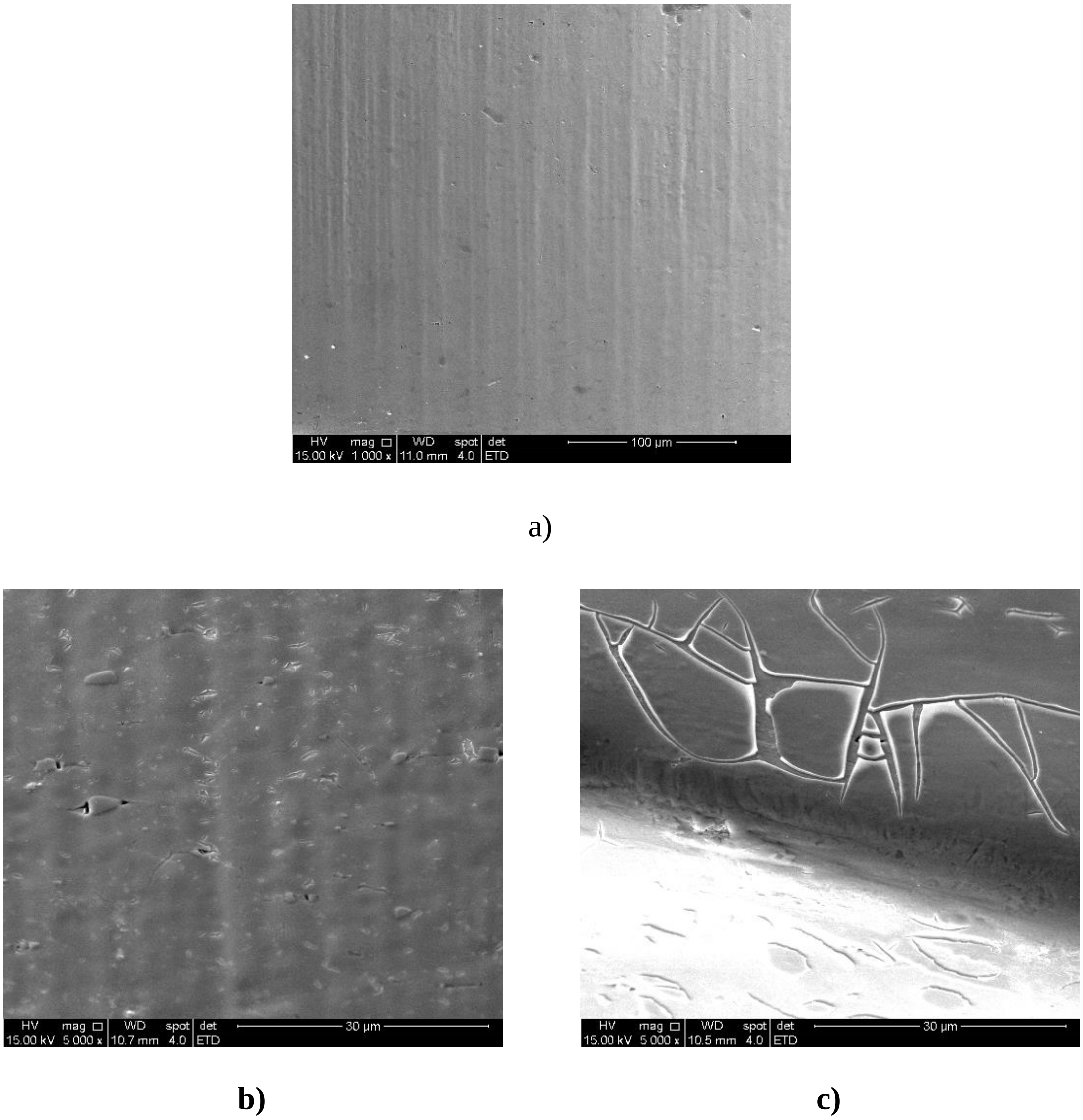

a)

b) **c)**

Figure 5.29 – Secondary electron images of RaCe endodontic instruments a) as received; b) TiO_2 coated and c) TiO_2 coated at the cutting edge; with a magnification of 5000x

The intercept method was used with the DSC curves to calculate the transformation temperatures of the alloy (Höhne *et al.* 2003). The mean values for the martensitic and austenitic transformation temperatures for the tested samples are given in Table V.3. The high temperature used to partially crystallize the oxide film is enough to promote de decomposition of the supersaturated matrix phase on Ti_3Ni_4. However, the short exposure time (10 min) did not changed significantly the martensitic peak and martensitic start and austenitic peak and austenitic final temperatures, therefore maintaining the stress needed to induce martensitic transformation close to the original, as showed in the three-points bending results of Figure 5.14. Martensitic final and austenitic start temperatures had increased with the thermal treatment, making the transformation temperature range shorter for each phase. This short transformation range is ideal for applications of the alloy as thermally activated sensors and actuators (Jani et al. 2014).

Table V-3– Phase transformation temperatures (active part of NiTi endodontic instruments RaCe 25/0.06; standard deviations are indicated in parenthesis)

Group	**Ms (ºC)**	**Mp (ºC)**	**Mf (ºC)**	**As (ºC)**	**Ap (ºC)**	**Af (ºC)**
As received	25 (5)	18 (6)	-1 (3)	6 (4)	25 (6)	33 (4)
Thermally treated	29 (3)	14 (2)	10 (2)	21 (2)	23 (3)	37 (1)
TiO_2 coated	26 (4)	19 (3)	10 (2)	21 (3)	29 (2)	37 (2)

5.3.3. The cutting efficiency of the instruments

Cutting capacity and apical force average curves from 10 instruments of each group (AR, CI and TT) can be seen in Figs. 5.30 and 5.31, respectively. In both cases, the curves are similar to each other, showing a close behavior of instruments regardless of the treatment. The inset in each graph gives the total area under the curve. This area is proportional to the work done to pierce through the artificial canal. In the first case (Fig. 5.30), this area is proportional to the total energy spent by the engine to shape the root canal. The second one (Fig. 5.31) is proportional to the work done by the operator to reach the end of the block. In both cases, the area of the coated sample is slightly lower when compared with the other 2 groups. This change can be explained by a difference in friction between root canal walls and instrument blades. A smoother surface can be seen on the SEM and AFM images for the layered instruments. This feature can be further studied for other applications as in orthodontics arch wires, where the friction between the NiTi wire and the brackets is important for the evolution of the treatment (Wei *et al.* 2011, Varela *et al*. 2014).

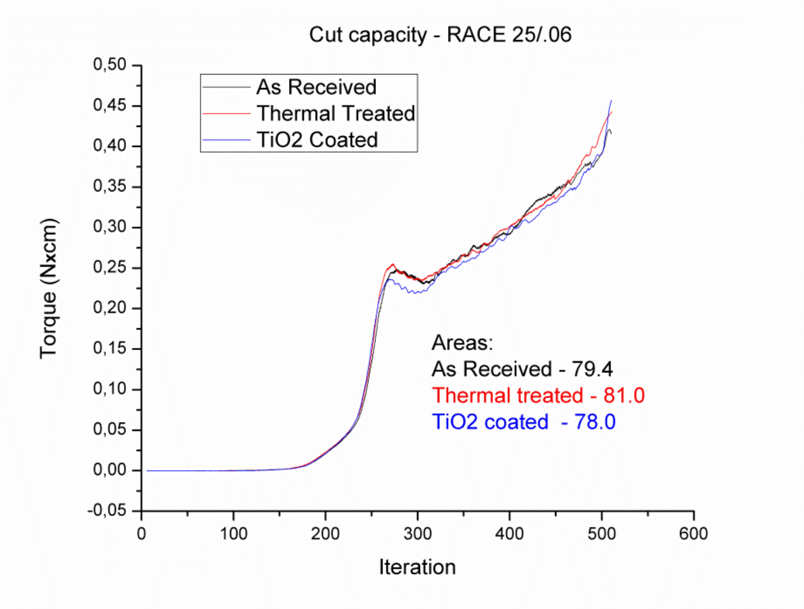

Figure 5.30 – Cutting efficiency of NiTi endodontic instruments RaCe 25/0.06

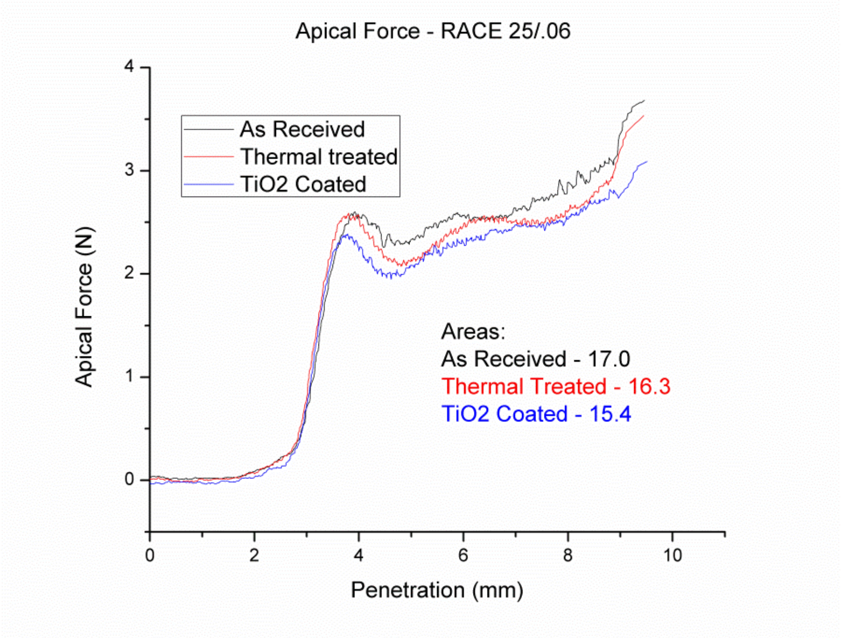

Figure 5.31– Apical force for NiTi endodontic instruments RaCe 25/0.06

5.3.4. The corrosion of the instruments in NaClO

Cyclic polarization curves for 6 samples of each group (AR, CI and TT) in NaClO with pH 12.3 are showed in appendix C. Results showed a high corrosion resistance of all instruments in the tested solution, as realized by a negative hysteresis loop in all measurements and by the non-formation of pits in potentials below 800 mV, which is the maximum potential suggested by ASTM F2129 norm, for the majority of the tested samples (4 of 6 for each group). On these cases, abrupt increase in current density occurred only for potentials above 1.0 V, caused by the evolution of the oxygen on water oxidation. This outcome agreed with other results from the literature (Busslinger et al. 1998, O'Hoy et al. 2003, Darabara et al. 2004, Berutti et al. 2006, Martins et al. 2006, Nóvoa *et al.* 2007).

The average values for the zero current potential (E_{zc}), breakdown potential (E_{pit}) and passivation current density (I_{pass}) shown in table V.4 were calculated with the 2 results of each group that showed pitting corrosion (abrupt increase in current density at lower potentials). Standard deviation for E_{pit} and I_{cor} were smaller than 3%, with the exception of I_{pass} for the thermally treated group which generated a large value (close to 100%). A comparative curve of these samples is shown in Figure 5.32.

Table V-4– Cyclic polarization test mean results (only for corroded samples)

Group	**E_{zc}(mV)**	**E_{pit}(mV)**	**I_{pass}(µA/cm^2)**
As received	213	548	1.71
Thermally treated	40	600	182.1
TiO_2 coated	161	568	0.187

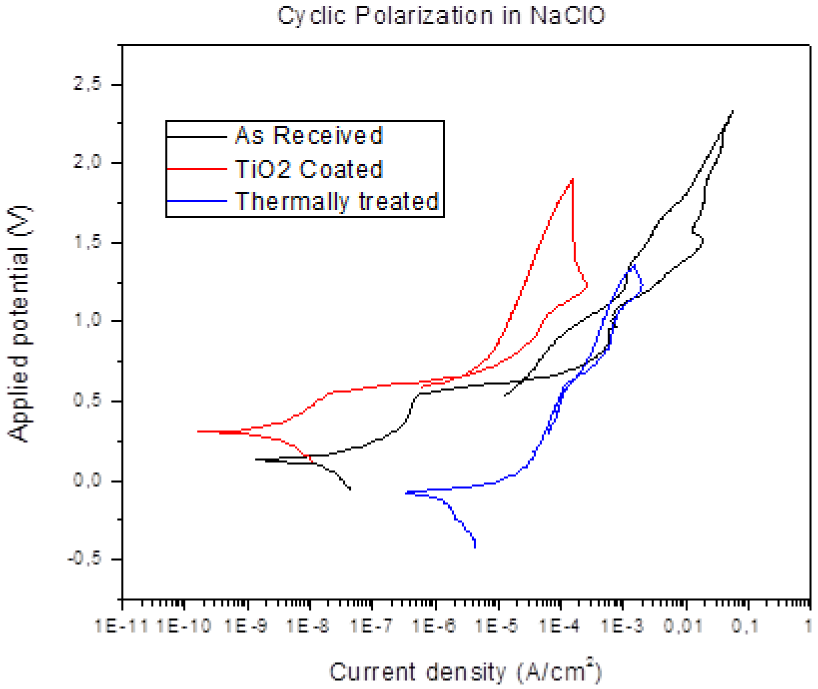

Figure 5.32– Comparative cyclic polarization curves for as received, thermally treated and TiO_2 coated RaCe endodontic instruments in NaClO

Pitting potential for the corroded samples was similar for the three tested groups, but a significantly higher value of I_{pass} was measured for the TT samples. The proximity of the E_{pit} values could be caused by the non-uniformity (cracks) of the film on the coated group (Figure 5.27) and the natural oxide layer on the TT group. The TiO_2 sol-gel layer covers almost all the active part of the instruments leaving only a few cracks where pitting corrosion can be initiated at lower potentials, keeping a reduced corrosion rate. The high value of I_{pass} for the samples from TT group showed a passivation at higher corrosion current densities, meaning that these files suffer greater amounts corrosion before the passivating film start acting as a protective barrier. The surface of one of those samples (TT group) showing a high amount of pit corrosion is presented at Figure 5.33.

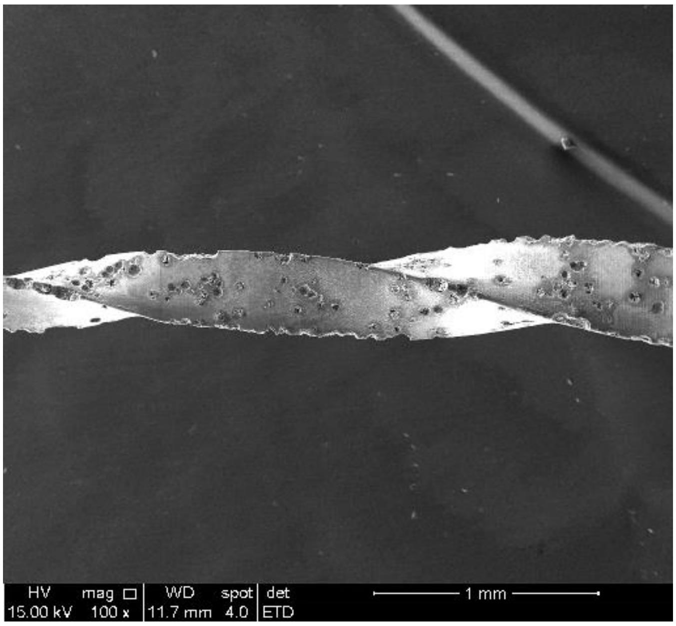

Figure 5.33 – Secondary electron Image of thermally treated endodontic instrument after suffering severe pitting corrosion with 2.0 V applied tension in NaClO

Comparison between AR and CI groups showed a very similar behavior. However, the experiments were performed with instruments in its unstrained state, due to equipment limitations. NiTi alloys are susceptible to stress cracking corrosion (Yokoyama et al. 2004, Chan et al. 2012, Liu *et al*. 2014). Film elasticity and adhesion was confirmed by three-points bending tests and its protectiveness properties should also work on the strained state. A difference in corrosion tests between these last two groups should be expected if the test were performed with stressed samples. The ability to keep a low corrosion rate even on the strained state can also be very useful to reduce Ni release in NiTi alloys used for implants and improve its biocompatibility.

5.2.5. The fatigue resistance of the instruments

The results of the flexural fatigue tests are presented in Figure 5.34. To investigate if the calculated mean values for the number of cycles until fracture N_f where statistically different, the statistical analyses of variances (ANOVA; Montgomery & Runger 2012) were performed among the groups with 95% confidence level ($\alpha = 0.05$). The test can only be applied if the data residuals showed a normal distribution. The normality of the data residuals was confirmed by Shapiro-Wilk tests (1965). Results from the analysis of variances of the samples before the corrosion showed a statistical difference between the mean values of N_f for the three groups ($P = 0.003$). Fishers least significant difference tests (Montgomert & Runger 2012) indicated a similarity between average N_f values for the TT and CI groups and a difference between these two and the control AR group, meaning that the thermal treatment itself was responsible for increasing the fatigue life.

The T-test analysis among each group before and after the corrosion showed a significant statistical reduction in fatigue life for the thermally treated group ($P = 0.005$) but no statistic difference between the other two ones ($P = 0.3$ for as received samples and $P = 0.4$ for TiO_2 coated instruments). Best performance in fatigue life after corrosion was achieved by the TiO_2 coated endodontic instruments.

In summary, the statistical analysis of the fatigue test data led to two conclusions:

- Before the corrosion tests, fatigue life of endodontic instruments was improved by the thermal treatment, since N_f value for both CI and TT groups is larger than the one for the AR group.
- After the corrosion tests, the mean value of N_f for the TT group had decreased due to sample corrosion. This makes the coated samples group the one with the better performance in fatigue life.

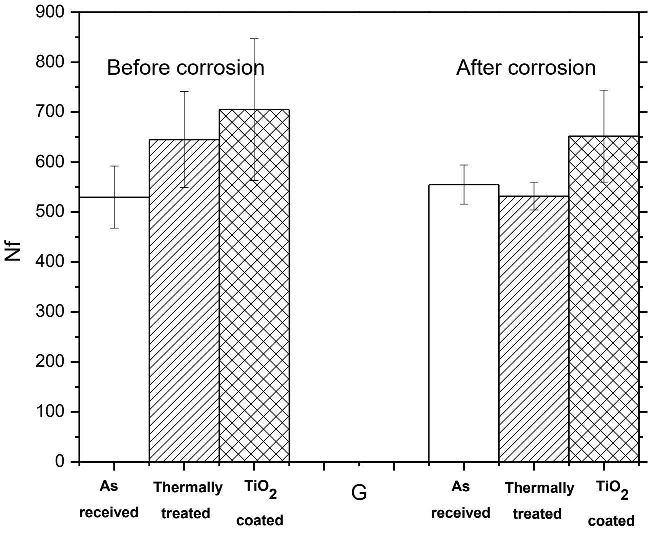

Figure 5.34 – Number of cycles until fracture on fatigue tested NiTi instruments model RaCe

The thermal treatment chosen for film formation was enough to initially improve material fatigue life. Strains normally imposed on endodontic instruments are extremely high (4 to 6 %), in a way that it is almost impossible to avoid crack formation through enhancement of surface smoothness, as demonstrated by a reduction in fatigue life of electrical polished instruments (Bui *et al.* 2008). In those cases, the mechanism to improve fatigue resistance is to reduce crack propagation. The short thermal treatment at 500ºC was not enough to significantly change phase composition as deducted from the DSC results. The improvement was then achieved by the reduction of internal stresses produced during instrument fabrication. This result corroborates with life improvement expectance caused by thermal treatment of endodontic instruments (Montalvão *et al.* 2014). The reduction in fatigue life after corrosion for the thermally treated group was caused by the higher corrosion of a few instruments, as seen by the high value on passivating current density showed in table V.4. A low value of N_f for two thermally treated instruments, the same two which presented higher corrosion currents, kept the mean number of cycles to fracture low.

Fractured surfaces were analyzed by SEM. The cross-section of two fatigued instruments of each group after corrosion tests are showed in Figure 5.35. The process of failure by fatigue occur in three distinct steps, as described in section 3.2.3: formation of surface cracks, inward propagation of those cracks with each tensile cycle and finally abrupt material separation when stress is increased enough due to cross-sectional area reduction. Endodontic instruments are subjected to high strain cycles with its normal use. This makes the first stage of failure by fatigue to occur during the firsts few rotations of the instrument inside the root canal. The second stage, crack propagation, will then be dominant step that will define instruments fatigue life. As it can be easily observed in Figure 5.35, the propagation area for the coated samples is larger when compared to the other two groups after corrosion, in agreement with the results presented in Figure 5.34 that indicate a higher fatigue life for those samples.

A higher magnification of the crack propagation areas can be seen in Figure 5.36. All samples presented the same morphology, showing the dimples characteristics of a ductile final fracture, indicating that the coating or thermal treatment did not change the fatigue fracture mechanism of the instruments.

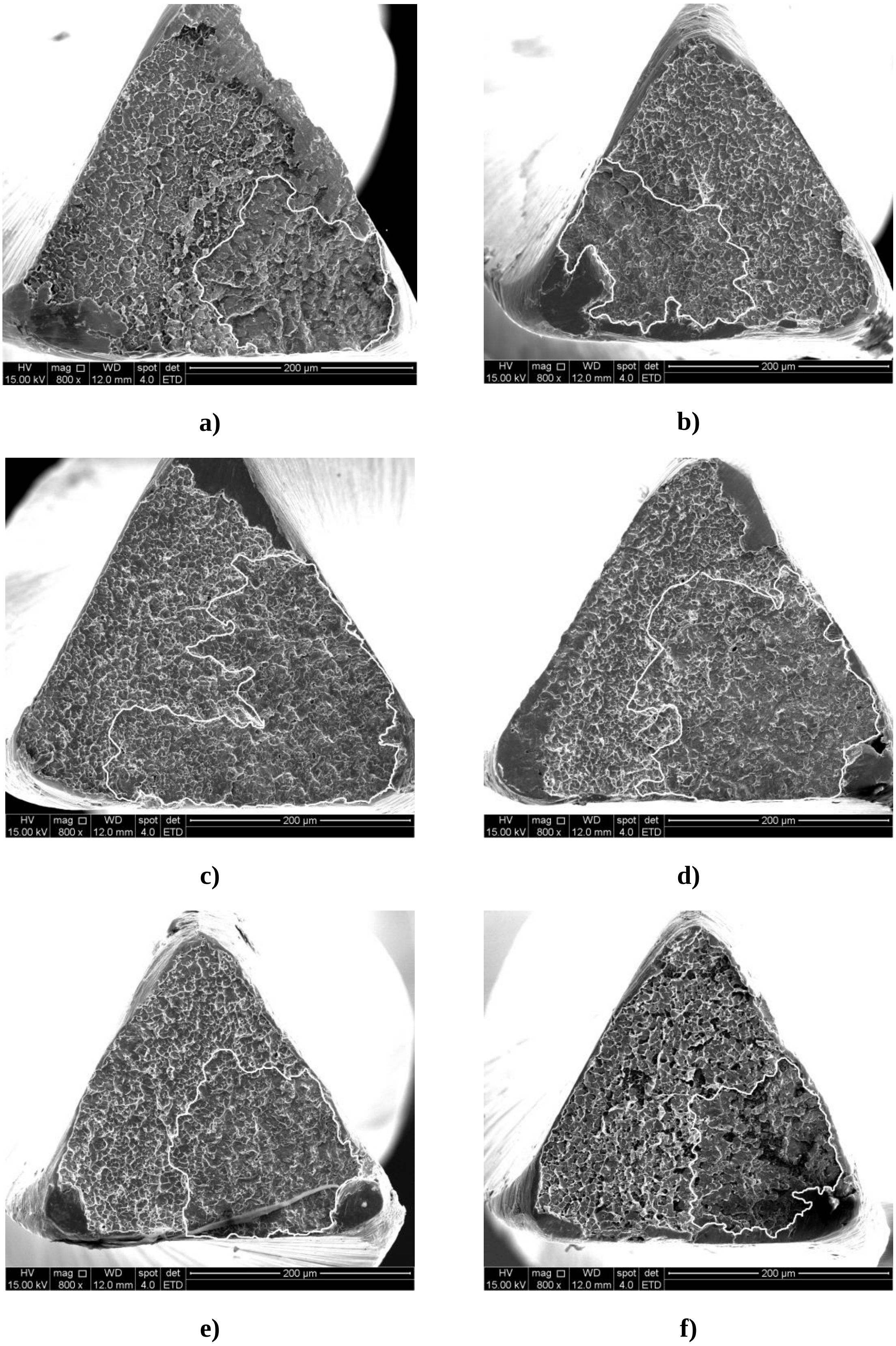

Figure 5.35 – Secondary electron images of fractured endodontic instruments after fatigue and corrosion tests. a) AR 1; b) AR 2; c) CI 1; d) CI 2; e) TT 1; f) TT 2

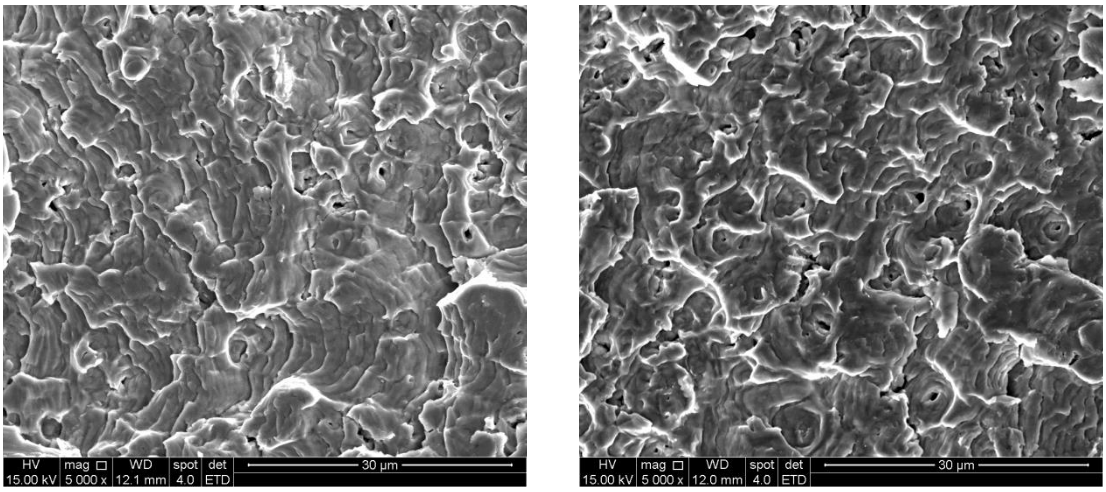

a) **b)**

Figure 5.36 - Secondary electron image of crack propagation area of the cross-section of the a) as received and b) TiO_2 coated samples fatigued after corrosion test

In summary, NiTi endodontic instruments RaCe 25/0.06 were coated using the deposition route developed in section 5.1 and characterized in section 5.2. The thermal treatment needed to coat the material did not significantly changed the transformation temperatures, maintaining the general mechanical properties of the files, but improving instruments fatigue life through stress relaxation mechanism. The oxide layer also did not altered drastically the cutting efficiency of the instruments, only slightly reducing torque needed to shape artificial canals, probably due to the effect of lower friction. The deposited TiO_2 layer improved files corrosion resistance in NaClO by lowering the passivating corrosion current density, mainly when compared with the thermally treated group. The effect of corrosion protection should be more pronounced with the material in a strained state, since NiTi shape memory alloy is subjected to stress-induced corrosion. The corrosion protection of the oxide layer was also noticed by a larger difference in the number of cycles until failure between the coated group, which presented the highest value of N_f, in comparison with the other two groups after corrosion.

6. Final considerations

6.1. Original contributions to knowledge

Over the last decades, intense research was made to modify NiTi shape memory alloys surface in order to improve its biocompatibility. The main objective of all the works was to reduce Ni surface concentration in order to prevent Ni release inside the highly corrosive human body. However, there was little or no focusing on the mechanical properties of the modified surface. The main reason for the introduction of shape memory alloys in medicine was its capacity to recover its original shape after suffering severe strain. The modified surface should bear the same deformation without losing its functionality.

The developed coating procedure in this work meets these requirements. The oxide layer formed is effective to protect against corrosion, significantly reduced the Ni surface concentration and is capable of sustaining up to 6.4% deformation. To the author knowledge, up to the date the only surface modification treatment capable of enduring this kind of deformation is the electropolishing followed by water boiling to restore the TiO_2 natural oxide layer, which have only a few dozen nanometers in thickness presenting a higher Ni surface concentration and a lower biocompatibility.

For the practical application, the coating had significantly improved endodontic instruments fatigue life and corrosion resistance. These improvements should be even more pronounced under strained conditions, since NiTi alloys are prompt to stress induced corrosion and the protective layer will not crack within normally imposed strains.

The developed method to measure cutting efficiency can be easily applied in other researches and can be further developed to become a standardized methodology to assess this parameter.

6.2. Suggestions to future investigations

As mentioned in the literature review, NiTi shape memory alloys are susceptible to stress induced corrosion. The developed coating should be able to protect the metal surface against chemical attack even when strained. Due to equipment limitations, the corrosion resistance of the coated alloy could not be investigated under stressed conditions. This coating feature should be further tested to confirm the hypothesis.

Developed route produced a nanocomposite film constituted of amorphous, anatase and rutile TiO_2. The crystalline phases of the oxide present a strong photocatalytic activity and superhydrophilicity. These combined characteristics can be used to easily sterilize NiTi biomedical objects by a simple UV light exposure followed be rinsing with water. The effectiveness of this simple sterilizing procedure can be tested.

The decrease in roughness caused by the film can also be additionally explored. A low friction coefficient is useful in biological applications, as it is the case for orthodontic arch wires and endodontic instruments.

The surface roughness is also connected to the biocompatibility through the modification of the potential to cellular adhesion. *In vitro* cellular adhesion or protein adhesion tests can be performed to better understand the link between these two parameters. Also, as discussed on section 3.3.2, TiO_2 crystallinity can influence the surface capacity to adsorb protein and cellular adhesion. New thermal treatments can be tried to modify rutile and anatase amounts in order to “program” the surface to have a high or low cellular adhesion potential. Specific TiO_2 coatings can then be generated for each particular biological application.

Still in the biocompatibility issue, one attempt was made to comparatively measure Ni release of coated and uncoated NiTi in simulated body fluid. The sensibility of the used equipment to measure Ni concentration on the solution was not enough to differentiate the extremely low amounts of Ni on the solutions. Ni release tests can be made in strained and unstrained states to compare release rate in coated and uncoated samples.

Finally, in this work the coating was applied in one specific system. The procedure can be used to coat any biomedical device. The route should be tested to coat endovascular stents, orthodontic arch wires, orthopedic implants, endovascular filters, among others.

6.3. General conclusions

In this work, it was developed a route to coat NiTi shape memory alloys with a thick and flexible TiO_2 composite bilayer in order to improve alloy corrosion resistance and biocompatibility. The film was first characterized and then applied to coat endodontic instruments. The results of this research can lead to the following conclusions:

- The proposed deposition route produced a nanocomposite film ~100 nm thick, composed of a mixture of anatase and rutile TiO_2 at the first 50 nm of the film/alloy interface, followed by 50 nm amorphous film capable to sustain up to 6.4% strain without cracking or peeling that can be used to coat NiTi devices for bioapplications.
- The thermal treatment used to partially crystallize the film improving its biocompatibility and flexibility did not significantly change the mechanical properties of the alloy.
- An epitaxial effect on the NiTi/TiO_2 interface catalyzed the formation of rutile at lower temperatures.
- Developed coating can reduce NiTi surface roughness and thus decrease friction.

- The coating reduced Ni surface concentration which should improve the alloy biocompatibility.
- The route was used to coat NiTi endodontic instruments model RaCe 25/0.06 forming a protective oxide layer covering most of the file active part surface.
- The thermal treatment used to crystallize the TiO_2 film improved endodontic instrument fatigue life.
- The TiO_2 film did not significantly changed instruments cutting efficiency.

The proposed objectives of the work were successfully accomplished and the developed route should be further explored to coat other NiTi biomedical and dental devices.

References

ACIK, O., *et al*. Characterization of samarium and nitrogen co-doped TiO_2 films prepared by chemical spray pyrolisis, *Applied Surface Science*, v.261, p. 735 – 741, 2012

ANDREASEN, G.F.; Hilleman, T.B. An evaluation of 55 cobalt substituted Nitinol wire for use in orthodontics. *Journal of American Dental Association*, v. 82, p.1373-1375, 1971.

ARMITAGE, D.A., GRANT, D.M. Characterization of surface-modified nickel titanium alloys. *Materials Science & Engineering A*, v.349, p. 89-97, 2003.

ASTM INTERNATIONAL, West Conshohocken, Standard Test Method for Conducting Cyclic Potentiodynamic Polarization Measurements to Determine the Corrosion Susceptibility of Small Implant Devices, 2015. 9p.

BAHIA, M.G.A. Resistência à fadiga e comportamento em torção de instrumentos endodônticos de NiTi*ProFile* (Tese de doutorado em engenharia metalúrgica e de Materiais). Belo Horizonte, Brasil: Universidade Federal de Minas Gerais, 2004.

BAHIA, M. G.A., BUONO, V.T.L. Decrease in fatigue resistance of nickel-titanium rotary instruments after clinical use in curved root canals. *Oral Surg. Oral Med. Oral Pathol. Oral Radiol. Endod.*, v.100, n.2, p.2249-2255, 2005.

BAHIA, M. G. A., GONZALEZ, B. M., BUONO, V. T. L. Fatigue behavior of Nickel-titanium superelasctic wires and endodontic instruments. *Fatigue Fracture. Engineering. Materials &. Structure*,v.29, n.7, p.518-523, 2006.

BERGER-GORBET, M., BROUXUP, B., RIVARD, C., YAHIA, L. H. Biocompatibilty testing of NiTi screws using immunohistochemestry on sections containing metallic implants. *Journal Biomedical Material Research*, v.32, n.2, p.243-248, 1996.

BERUTTI, E., ANGELINI, E., RIGOLONE, M., MIGLIARETTI, G., PASQUALINI, D. Influence of sodium hypochlorite on fracture properties and corrosion of ProTaper Rotary instruments. *International Endodontic Journal*, v.39, n.9, p. 693-699, 2006.

BHOSALE, R.R., *et al*., Photocatalytic activity and characterization of sol-gel-derived Ni-doped TiO_2-coated active carbon composites. *Applied Surface Science,* v.261, p. 835 – 841, 2012.

BRINKER, C.J., FRYE, G.C., HURD, A.J., ASHLEY, C.S. Fundamentals of sol-gel dip coating. *Thin Solid Fimls,* v.201, p. 97-108, 1991.

BUI, T.B., MITCHELL, J.C., BAUMGARTNER, J.C. Effect of Electropolishing ProFile Nickel–Titanium Rotary Instruments on Cyclic Fatigue Resistance, Torsional Resistance and Cutting Efficiency. *Journal of Endodontics*, v.34, p. 190 – 193, 2008

BURGOS, M., LANGLET, M. Condensation and Densification Mechanisms of Sol-Gel TiO_2 Layers at Low Temperature. *Journal of Sol-Gel Science and Technology*, v.16, 267 – 276, 1999a.

BURGOS, M., LANGLET M. The sol-gel transformation of TIPT coatings: a FTIR study. *Thin Solid Films*, v.349, 19 – 23, 1999b.

BUSSLINGER, A., SENER, B., BARBAKOW, F. Effects of sodium hypochlorite on nickel-titanium Lightspeed instruments. *International Endodontic Journal,* v.31, n.4, p.290-294, 1998.

CARP, O., HUISMAN, C. L., RELLER, A. Photoinduced reactivity of titanium dioxide. *Progress in Solid State Chemistry*, v.32, n.1-2, p.33-177, 2004.

CHAN, C. W., MAN, H. C., YUE, T. M., Susceptibility to stress corrosion cracking of NiTi laser weldment in Hank's solution. *Corrosion. Science,* v.57, p.260-269, 2012.

CHANG, L. C., READ, T. A. Behavior of the elastic properties of AuCd. *Transactions AIME*, v.191.47-52, 1951.

CHENG, Y., ZHENG, Y. The corrosion behavior and hemocompatibility of TiNi alloys coated with DLC by plasma based ion implantation. *Surface Coaingt Technology,* v.200, n.14-15, p.4543-4548, 2006.

CULLITY, B.D., STOCK, S.R. Elements of X-ray diffraction, 3rd ed., New Jersey, U.S.A: Prentice Hall, Inc. 2001. 664 p.

DARABARA, M. L., BOURITHIS, L., ZINELIS, D., PAPADIMITRIOU G.D., Susceptibility to localized corrosion of stainless steel and NiTi endodontic instruments in irrigating solutions. *International Endodontic Journal*, v. 37, n.10, p.705-710, 2004.

DAVÍÐSDOTTIR, S. *et al*. Interfacial Structure and Photocatalytic Activity of Magnetron Sputtered TiO_2 on Conducting Metal Substrates. *Applied Materials & Interfaces,* v. 6 (24), p. 22224 – 22234, 2014.

HÖHNE, G.W.H., HEMMINGER, W.F., FLAMMERSEHIM, H.J. Differential Scanning Calorimetry, 2nd ed., Berlin, Germany. Ed. Springer. 2003

DUERIG, T. W., MELTON, K. N., PROFT, J. L. Wide hysteresis shape memory alloys. In: DUERIG, T. W.; MELTON, K. N.; STÖCKEL, D.; WAYMAN, C. M. *Engineering Aspects of Shape Memory Alloys*. Butterworth-Heineman: 1990.p. 499.

ES-SOUNI, M., ES-SOUNI M., FISCHER-BRANDIES, H. Assessing the biocompatibility of NiTi shape memory alloys used for medical applications. *Analytical and Bioanalytical Chemistry*, v.381, p. 557 – 567, 2005

FELT, R. A., MOSER, J. B., HEUER, M. A. Flute design of endodontic instruments: its influence on cutting efficiency. *Journal Endodontics*, v. 8, n.6, p.253-259, 1982.

FUSHIMI, K., STARTMANN, M., HASSEL, A. Electropolishing of NiTi shape memory alloys in methanolic H2SO4. *Electrochemical Acta*, v.52, n.3, p.1290-1295, 2006.

GEORGESCU D., BAIA, L., ERSEN, O., BAIA, M., SIMON, S. Experimental assessment of the phonon confinement in TiO_2 anatase nanocrystallites by Raman spectroscopy. *Journal of Raman Spectroscopy*, v. 43 (7), p. 876-883, 2012

GRENINGER, A. B., MOORADIAN, V. G. Strain Transformation in metastable beta copper–zinc and beta copper–Ti alloys. *Aime Transactions*,v.128, p.337-69, 1938.

HAAPASALO, M., SHEN, Y., QIAN, W., GAO, Y., Irrigation in endodontics. *Dental Clinics of North America*, v.54, n.2,p. 291-312, 2010.

HAÏKEL, Y., SERFATY, R., LWIN, T.T., ALLEMANN, C. Measurements of the cutting efficiency of endodontic instruments: a new concept. *Jounal of Endodontics*, v. 22, n. 12, p.651-656, 1996.

HARTL, D. J., LAGOUDAS, D.C. Aerospace applications of shape memory alloys. Proc Inst MechEng, Part G: *Journal Aerospace Engineering*, v.221, p.535-552, 2007.

HENCH, L.L., WEST, J.K. The Sol-Gel Process. *Chemical Review*, v. 90, p. 33 – 72, 1990.

HE**β**ING, C., FRENZEL, J., POHL, M., SHABALOVSKAYA, S. Effect of martensitic transformation on the performance of coated NiTi surfaces. *Materials Science Engineering A*, v.486, n.1-2, p.461-469, 2008.

HOUMARD, M. Revêtements sol-gel TiO_2-SiO_2 naturellement super-hydrophiles visant à developer des surfaces à nettoyabilité accrue (these pour obtenir le grade de docteur en Matériaux, Mécanique, Génie civil et Électrochimie). Grenoble, France. Grenoble INP, 2009.

HUMBEECK, J. V. Non-medical applications of shape memory alloys. *Materials Science and Engineering A*, v.273-275, p.134-148, 1999.

JANI, J.M., LEARY, M., SUBIC, A., GIBSON, M.A. A review of shape memory alloy research, applications and opportunities. Materials and Design, v. 56, p. 1078 – 1113, 2014.

KAUFFMAN G, MAYO I. The story of Nitinol: the serendipitous discovery of the memory metal and its applications. *Chemical Educator*, v.2, n.2, p.1–21, 1997.

KOHL M. Shape memory microactuators (microtechnology and MEMS). 1 ed. Heidelberg: Springer-Verlag Berlin; 2010.

KULKARNI, M., et al. Titanium nanostructures for biomedical applications. *Nanotechnology*, v. 26, p. 1 – 18, 2015

KURDJUMOV GV, KHANDROS LG. First reports of the thermoelastic behaviour of the martensitic phase of Au–Cd alloys. *Doklady Akademii Nauk SSSR*, v.66, p.211–3, 1949.

LEO, D.J., WEDDL, C., NAGANATHAN, G., BUCKLEY, S.J. Vehicular applications of smart material systems. *SPIE Digital Library*, v.3326, p.106-116, 1998.

LEONG, S., RAZMJOU, A., WANG, K., HAPGOOD, K., ZHANG, X., WANG, H. TiO2 based photocatalytic membranes: a review. *Journal of Membrane Science*, v.472 p.167-184, 2014.

LIU, J.-K., LIU I.-H., LIU C., CHANG C. -J., KUNG K.-C., LIU Y.-T., LEE T.-M., JOU, J.-L. Effect of titanium nitride/titanium coatings on the stress corrosion of nickel–titanium orthodontic archwires in artificial saliva. *Applied Surface Science*, v. 317, n.30, p. 974-981, 2014.

LOTKOV, A., MEISNER, L., GRISHKOV, V. Titanium nickelide-based alloys: surface modifications with ion beam, plasma flows and chemical treatment. *Physics of Metals Metallography*, n.99, p.508-19, 2005.

MAITZ M, SHEVCHENKO N. Plasma-immersion ion-implanted Nitinol surface with depressed Ni concentration for implants in blood. *Journal of Biomedical Materials Research*,v.76A, n.2, p.356-65, 2006.

MANSUR, H.S. Técnicas de caracterização de materiais. In: ORÉFICE, L.R., PEREIRA, M.M., MANSUR, H.S. Biomaterias: Fundamentos & Aplicações. São Paulo: Guanabara Koogan, 2012, p. 283-327.

MARTINS RC, M.G.A. BAHIA, V.T.L. BUONO. The effect of sodium hypochlorite on the surface characteristics and fatigue resistance of ProFile nickel-titanium instruments.*Oral Surgery, Oral Medicine, Oral Pathology, Oral Radiology, and Endodontology*, v.102, n.4,p. e99-e105, 2006.

MASSALSKI, T. B.; OKAMOTO, H.; SUBRAMANIAN, P. R.; KACPRZAK, L. Binary Alloy Phase Diagrams. 2. ed. Ohio: ASM International, 1990. 2875 p.

MELO, M.C.C. Avaliação da resistência à fadiga de instrumentos de Níquel-Titânio acionados a motor (Dissertação de Mestrado em Endodontia) – Belo Horizonte, Brasil. Faculdade de Odontologia, Universidade Federal de Minas Gerais, Belo Horizonte, 1999.

MCCAFFERTY, E. Introduction to Corrosion Science, 1st ed., New York, U.S.A.: Springer, 2010. 575 p.

MONDAL S.; MADHURI R.; SHARMA P. K. PVA assisted low temperature anatase to rutile phase transformation (ART) and properties of titania nanoparticles. *Journal of Alloys and Compounds*, v.646, n.15, p.565-572, 2015.

MONTALVÃO D, Q. SHENDWEN, M. FREITAS.A study of Ni-Ti M-Wire in the flexural fatigue life of endodontic rotary files by using Finite Element Analysis, *Material Science and Engineering C*, v.40, p.172-179, 2014.

MONTGOMERY D.C., RUNGER, G.C. Estatística Aplicada e Probabilidade para Engenheiros, 5th ed., São Paulo, Brasil: ed. LTC. 2012. 548 p.

MORGAN NB. Medical shape memory alloy applications – the market and its products. *Material Science and Engineering A*, v.378, p.16-23, 2004.

NÓVOA X.R., MARTIN-BIEDMA B., VARELA-PATIÑO P.,COLLAZO A., MACÍAS-LUACES A., CANTATORE G., PEREZ M. C., MAGA-MUÑOZ F.The corrosion of nickel-titanium rotator endodontic instruments in sodium hypochlorite. *International Endodontic Journal*, v.40, p.36-44, 2007.

O´HOY PYZ, H.H. MESSER, E. A. PALAMARA.The effects of cleaning procedures on fracture properties and corrosion of NiTi files.*International Endodontic Journal*, v.36, n.11, p.724-732, 2003.

OKAZAKI S., OHHASHI T., NAKAO S. HIROSE Y., HITOSUGI T., HASEGAWA T. Wet Etching of Amorphous TiO2 Thin Films Using H3PO4-H2O2 Aqueous Solution, *Japanese Journal of Applied Physics*, v. 52, n.9R, 098002, 2013.

OTSUKA, K., REN X. Physical metallurgy of Ti-Ni-based shape memory alloys. *Progress in Materials Science,* v.50, 511- 678, 2005.

OTSUKA, K.; WAYMANN, C.M. Shape memory materials, 1st ed. Cambridge: Cambridge University Press, 1998. 284 p.

PARASHOS P., MESSER H.H., Rotary NiTi Instruments and its consequences. *Jounal of Endodontics,* v.32,n.11, p. 1031-1043, 2006.

PEIXOTO I. F. C., PEREIRA E. S. J., AUN D. P., BUONO V. T. L., BAHIA M. G. A. Constant insertion rate methodology for measuring torque and apical force in 3 nickel-titanium instruments with different cross-sectional designs. Journal of Endodontics, v.41, n.9, p.1540-1544, 2015.

PETERS O. A. Current Challenges and concepts in preparation of root canal systems: A review. *Jounal of Endodontics*, v.30, n. 8, p. 559 -567, 2004.

PLOTINO G., GRANDE N. M., CORDARO M, TESTARELLI L., GAMBARINI G.A Review of cyclic fatigue testing of niquel-titanium rotary instruments, *Jounal of Endodontics*, v.35, n.11, p.1469-1476, 2009.

POON R. W.Y., YEUNG K.W.K., LIU X.Y., CHU P. K., CHUNG C.Y., LU W.W., CHEUNG K. M. C., CHAN D.Carbon plasma immersion ion implantation of NiTi shape memory alloys. *Biomaterials*, v.26, n.15, p. 2265-2272, 2005.

PRUTTON, M. Introduction to surface physics, Oxford University Press Inc., New York, 2002.

QIAN H, LI H, SONG G, CHEN H, REN W, ZHANG S. Seismic vibration control of civil structures using shape memory alloys: a review. In: Earth and Space 2010@ Engineering, science, construction, and operations in challenging environments. ASCE; 2010. p. 3377–95.

RAUCH, E.F., VÉRON, M. Automated crystal orientation and phase mapping in TEM. *Materials Characterization*, v. 98, p. 1-9, 2014

RUSSEL, S. *Shape Memory Applications*. http://www.smainc.com/nitivssteel.html, 1998.

SABURI, T. TiNi shape memory alloys. In: OTSUKA, K.; WAYMAN, C.M. *Shape memory materials*, Cambridge: Cambridge Univ. Press, 1998. 289 p.

SANTOS L. A. Aplicação do método dos elementos finitos na análise do comportamento mecânico de instrumentos endodônticos de níquel-titânio.(Tese de Doutorado em Engenharia Metalúrgica e de Materiais). Belo Horizonte, Brasil: Universidade Federal de Minas Gerais, 2013.

SANTOS L.A., LÓPEZ J.B., LAS CASAS E., BAHIA M.G.A., BUONO V.T.L. Mechanical behavior of three nickel-titanium rotary files: A comparison of numerical simulation with bending and torsion tests, *Material Science and Engineering C*, v.37, n.1,p.258-263, 2014.

SCHÄFER E.; OITZINGER M. Cutting efficiency of rotary Nickel-Titanium instruments. *Jounalof Endododontics*, v.34, n.2, p. 198-200, 2008.

SCHMAHL, W. W., KHALIL-ALLAFI, J., HASSE, B., WAGNER, M., HECKMANN, A., SOMSEN, C. Investigation of the phase evolution in a superelastic NiTi shape memory alloy (%50.7 at.%Ni) under extensional load with synchrotron radiation. *Materials Science and Engineering A*, v.378, p.81-84, 2004.

SHABALOVSKAYA S, J. ANDEREGG, J. VAN HUMBEECK.Critical overview of Nitinol surfaces and their modifications for medical applications. *Acta Biomaterialia,* v. 4, n.3, p.447-467, 2008.

SHABALOVSKAYA S, WATAHA J, ANDEREGG J, HAUCH K, CUNNICK J. Surface treatments and biocompatibility of Nitinol. In: Proceedings of international conference on shape memory and superelastic technologies. Germany: Baden–Baden; 2004. p. 367–73.

SHABALOVSKAYA S. Surface, corrosion and biocompatibility aspects of Nitinol as an implant material. *Biomedical Materials and Engineering*, v.12, n.1, p.69–109, 2002.

SHAPIRO, S.S., WILK, M.B. AN ANALYSIS OF VARIANCE TEST OF NORMALITY (COMPLETE SAMPLES). *Biometrika*, V.52, Nº 3 and 4, p. 591-611, 1965

SHEVCHENKO N, PHAM M, MAITZ M. Studies of surface modified NiTi alloys. *Applied Surface Science*, v.235,n.1-2, 2004.

SHI P, CHENG F, MAN H. Improvement in corrosion resistance of NiTi by anodization in acetic acid. *Materials Letters*, v.61, n.11-12, p.2385-2388, 2007.

SILVA, M.A.C. Caracterização da vida em fadiga de limas endodônticas rotatórias de níquel-titânio. 2004. Dissertação (Mestrado), COPPE, Universidade Federal do Rio de Janeiro, Rio de Janeiro, 2004.

STRÓŻ, D. Studies of the R-phase transformation in a Ti-51at.%Ni alloy by transmission electron microscopy. *Scripta Materialia*, v.47, n.6, p.363-369, 2002.

SUN L, HUANG WM, DING Z, ZHAO Y, WANG CC, PURNAWALI H, TANG G. Stimulus-responsive shape memory materials: A review. *Materials and Design*, v.33, p.577-640, 2012.

THOMPSON S.A. An Overview of nickel-titanium alloys used in dentistry. *International Endodontic Journal*, v.33, n.4, p. 297-310, 2000.

TIMOSHENKO S, Strength of Materials Part I , third ed., Krieger,1958.

VANDENABEELE, P. Raman Spectroscopy. *Analytical and Bioanalyitcal Chemisstry*, v. 397 (7), p. 2629-2630, 2010.

VARELA J.C.,VELO M., ESPINAR E., LLAMAS J.M., RÚPEREZ E., MANERO J.M., JAVIER F.J. Mechanical properties of a new thermoplastic polymer orthodontic archwire. *Materials Science and Engineering C*, v.42, n.1, p.1-6, 2014.

VIEIRA EP, FRANÇA E.C., MARTINS R.C., BUONO V.T.L., BAHIA M.G.A. Influence of multiple clinical use on fatigue resistance of ProTaper rotary nickel-titanium instruments. *International Endodontic Journal*, v. 41, n.8, p.163-172, 2008.

VIEIRA, M.G.A., DA SILVA, M.A., DOS SANTOS, L.O., BEPPU, M.M. Natural-based plasticizers and biopolymer films: A review. *European Polymer Journal*, v. 47, p. 254 – 263, 2011.

VOJTECH D., FOJT J., LOSKA L., NOVAK P. Surface treatment of NiTi shape memory alloy and its influence on corrosion behavior. *Surface and Coatings Technology*,v.204, n.23,p.3895-3901, 2010.

WAYMAN, C.M., DUERIG, T.W. An introduction to martensite and shape memory. *Engineering Aspects of Shape Memory Alloys,* p.3-20. 1990.

WEI S., SHAO T., DING P. Improvement of orthodontic friction by coating archwire with carbon nitride film. *Applied Surface Science,* v.257, n.24, p. 10333-10337, 2011.

WEVER D. J., VELDHUIZEN A. G., VRIES J., BUSSCHER H. J., UGES D.R.A., VAN HORN J.R. Electrochemical and surface characterization of a nickel-titanium alloy. *Biomaterials*, v.19, n.7-9, p.761-769, 1998.

YEUNG K.W. K., POON R. W. Y., LIU X. Y., HO J. P. Y, CHUNG C. Y., CHU P. K, LU W.W., CHAN D., CHEUNG K.M.C.Improvement of corrosion resistance, mechanical properties and cytocompatibility of NiTi shape memory alloys using nitrogen, and oxygen plasma immersion ion implantation. *Journal of Biomedical Materials Research*, v.75A, n.2, p.256-267, 2005.

YGUEL-HENRY, S.; STEBUT, J. Cutting efficiency loss of root canal instruments due to bulk plastic deformation, surface damage, and wear. *Journal of Endodontics*, v.20, n.8, 1994.

YIN, Z.F., WU, L., YANG, H.G., SU, Y.H. Recent progress in biomedical applications of titanium dioxide. *Physical Chemistry and Chemical Physics*, v. 15, p. 4844 – 4858, 2013.

YOKOYAMA K, K. KANELO, E. YABUTA, K. ASAOKA, J. SAKAI. Fracture of nickel-titanium superelastic alloy in sodium hypochlorite solution. *Materials Science and Engineering A*, v.369, n.1-2, p.43-48, 2004.

ZEHNDER M, Root canal irrigants. *Journal of Endodontics,* v.32,n 5, p. 389-398, 2006.

Appendix A – Torque x Current cutting efficiency calibration

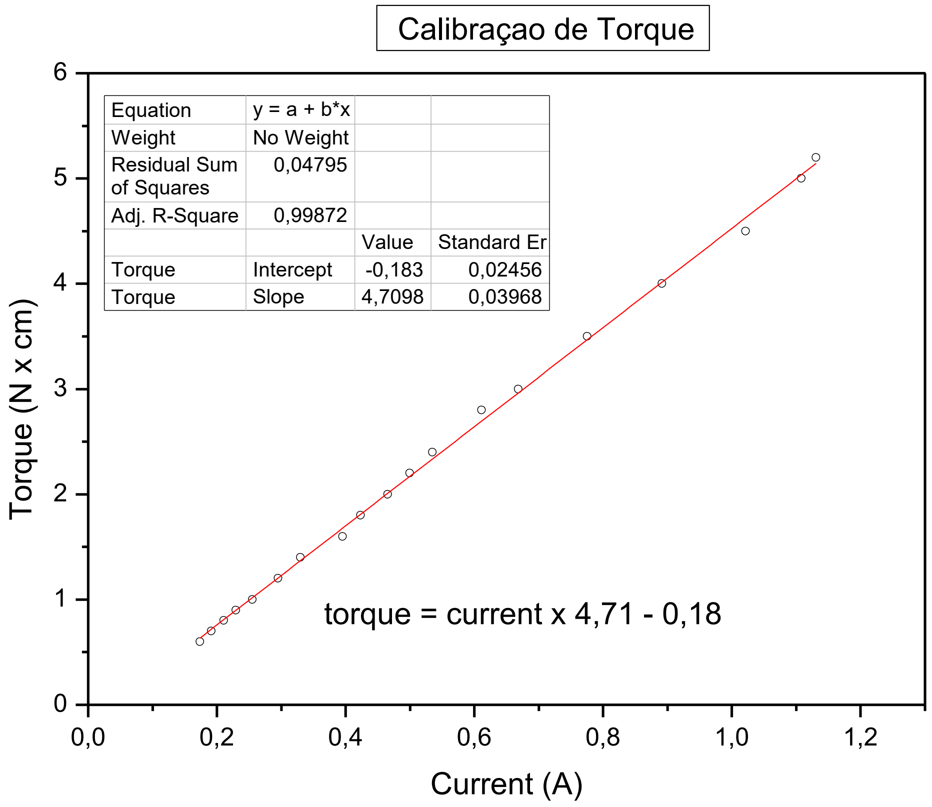

Appendix B –Differential Scanning Calorimetry of RaCe endodontic instruments

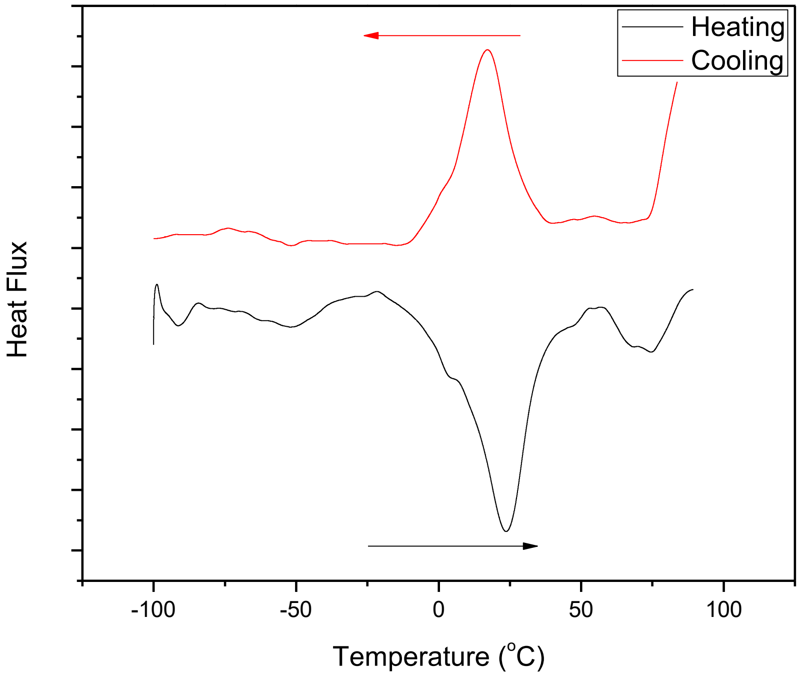

RaCe 25/0.06 as received 1

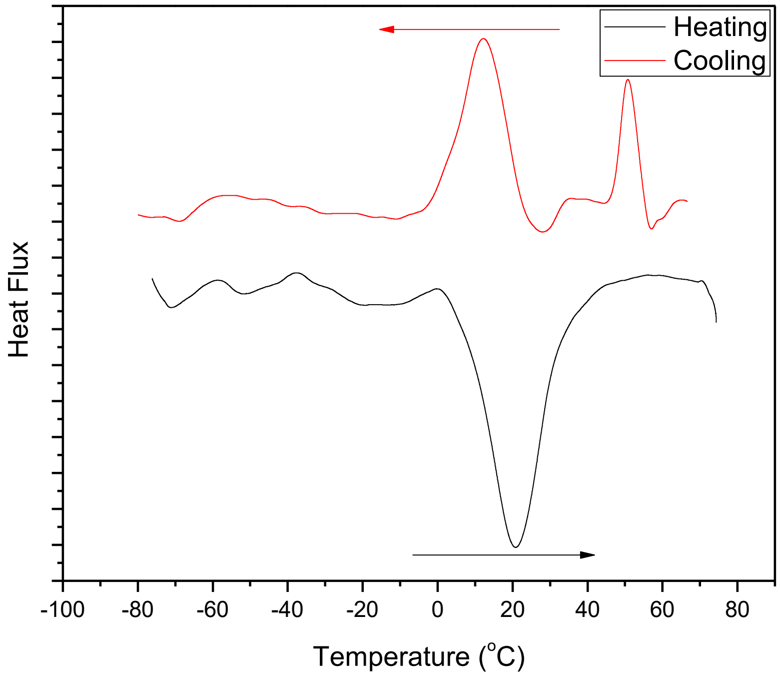

RaCe 25/0.06 as received 2

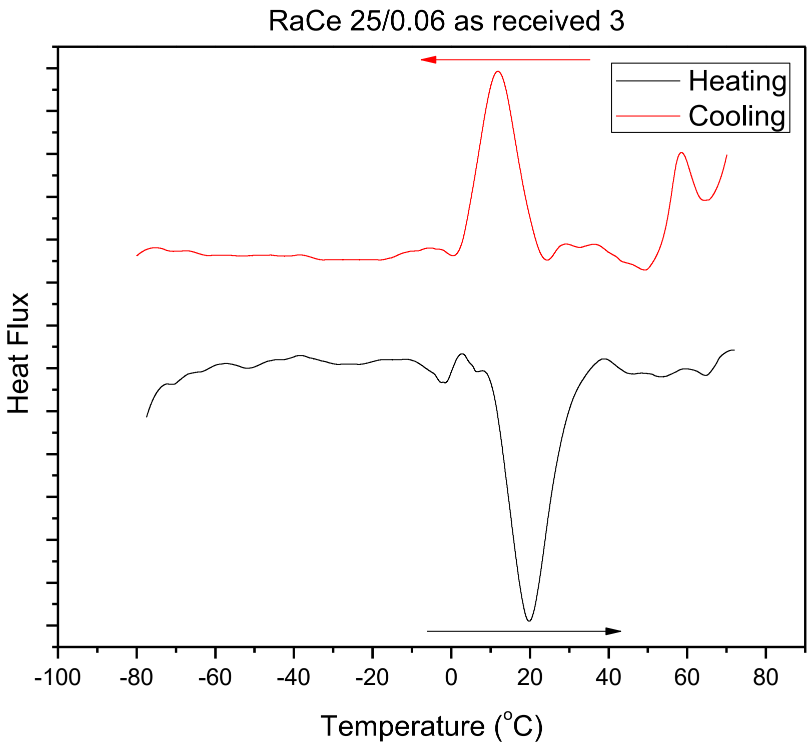
RaCe 25/0.06 as received 3
Heating
Cooling
Heat Flux
-100
-80
-60
-40
-20
0
20
40
60
80
Temperature (°C)

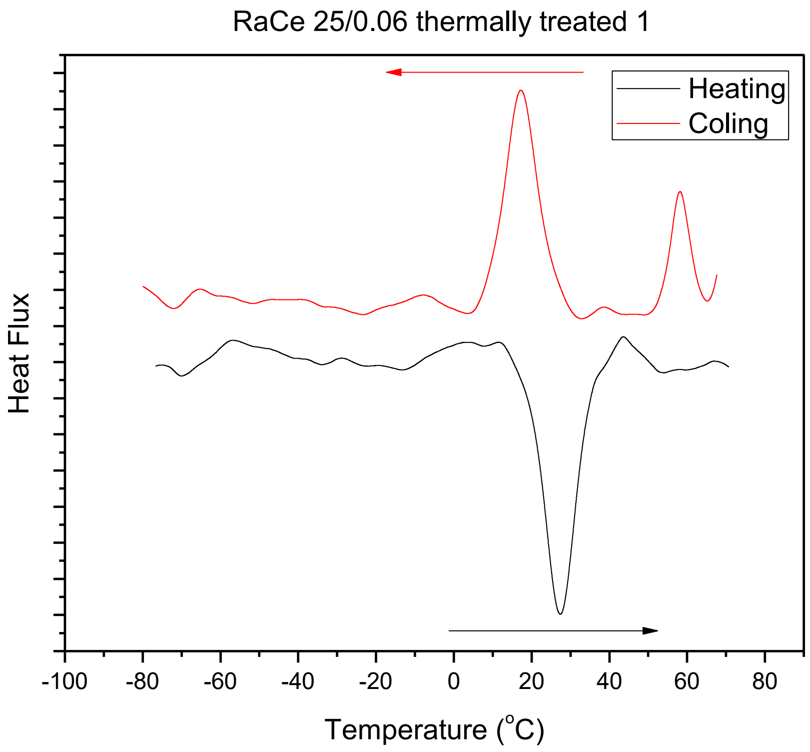
RaCe 25/0.06 thermally treated 1
Heating
Coling
Heat Flux
-100
-80
-60
-40
-20
0
20
40
60
80
Temperature (°C)

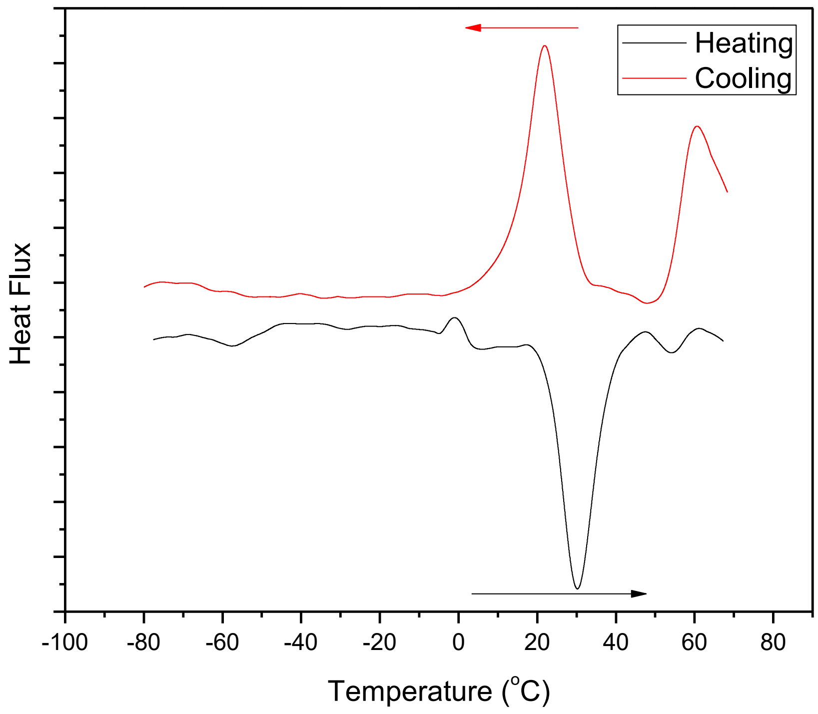

RaCe 25/0.06 thermally treated 2

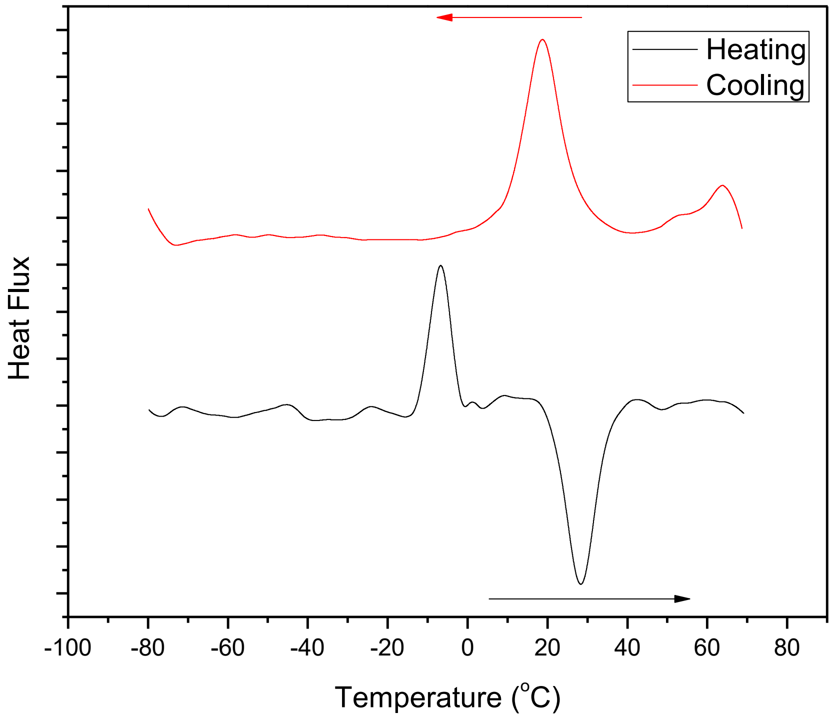

RaCe 25/0.06 thermally treated 3

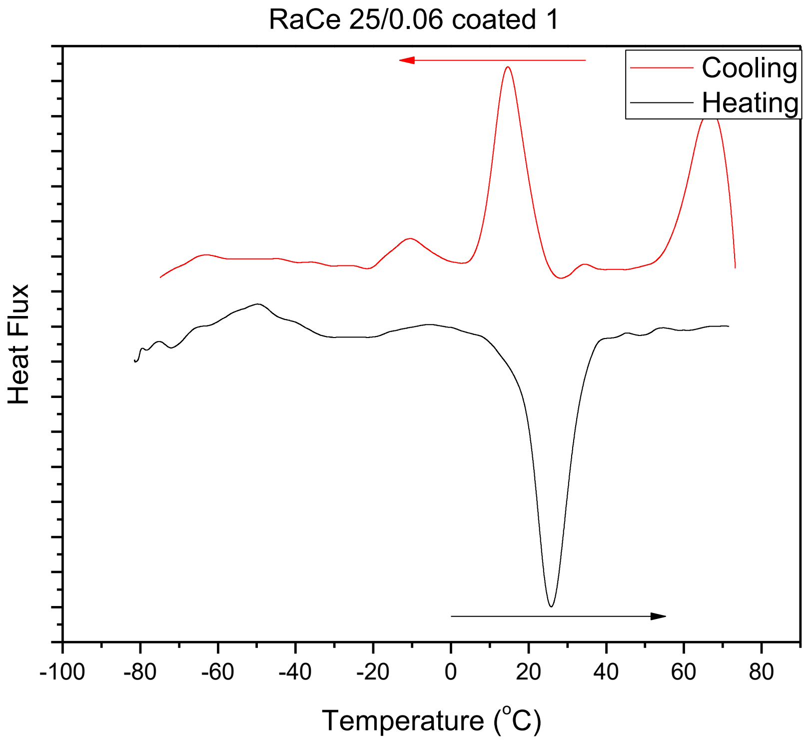
RaCe 25/0.06 coated 1
Cooling
Heating
Heat Flux
-100
-80
-60
-40
-20
0
20
40
60
80
Temperature (°C)

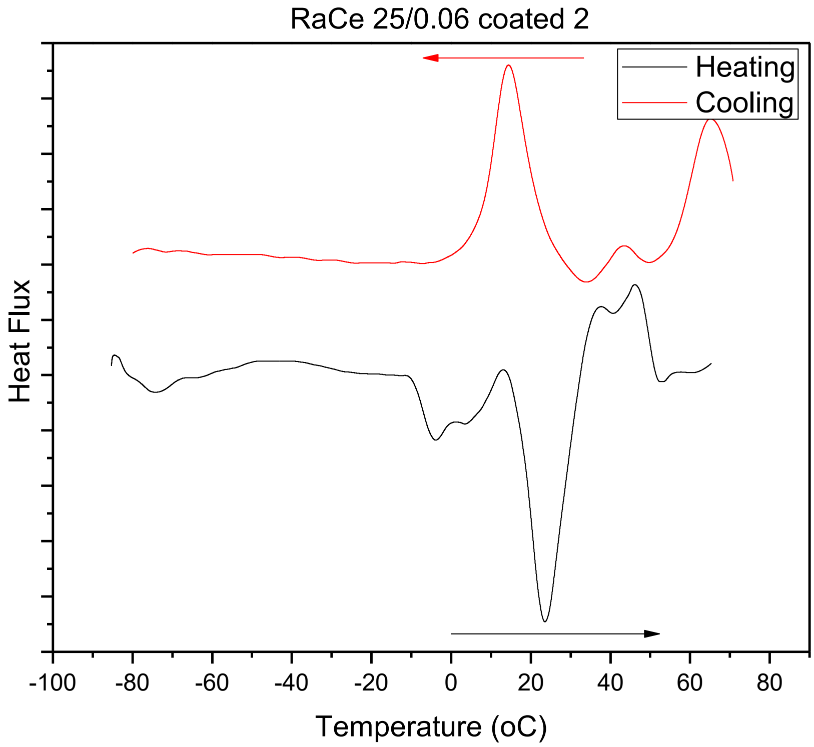
RaCe 25/0.06 coated 2
Heating
Cooling
Heat Flux
-100
-80
-60
-40
-20
0
20
40
60
80
Temperature (oC)

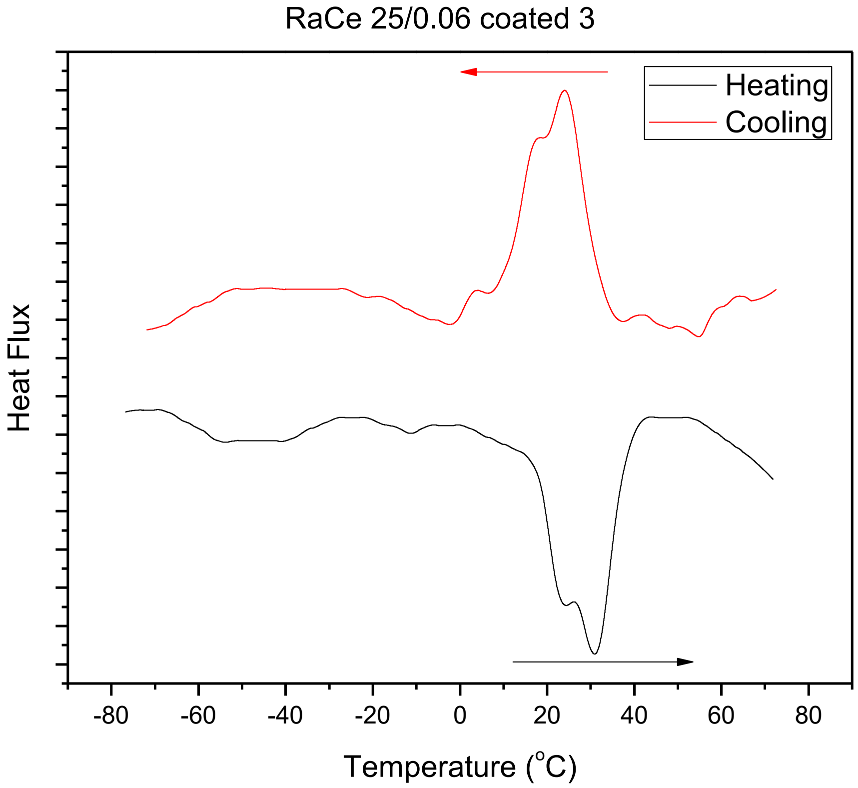
RaCe 25/0.06 coated 3
Heating
Cooling
Heat Flux
-80
-60
-40
-20
0
20
40
60
80
Temperature (^{o}C)

Appendix C – Cyclic Polarization curves for RaCe endodontic instruments

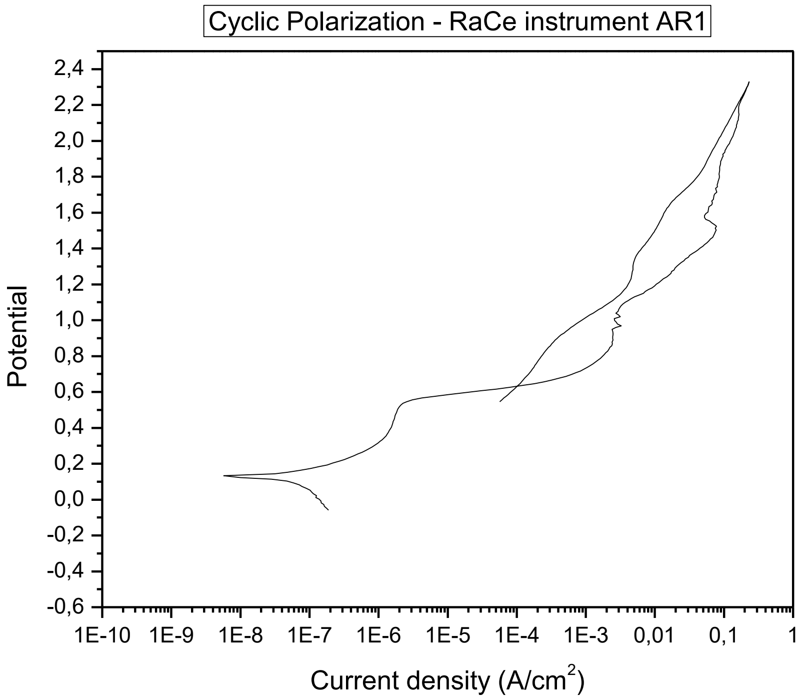

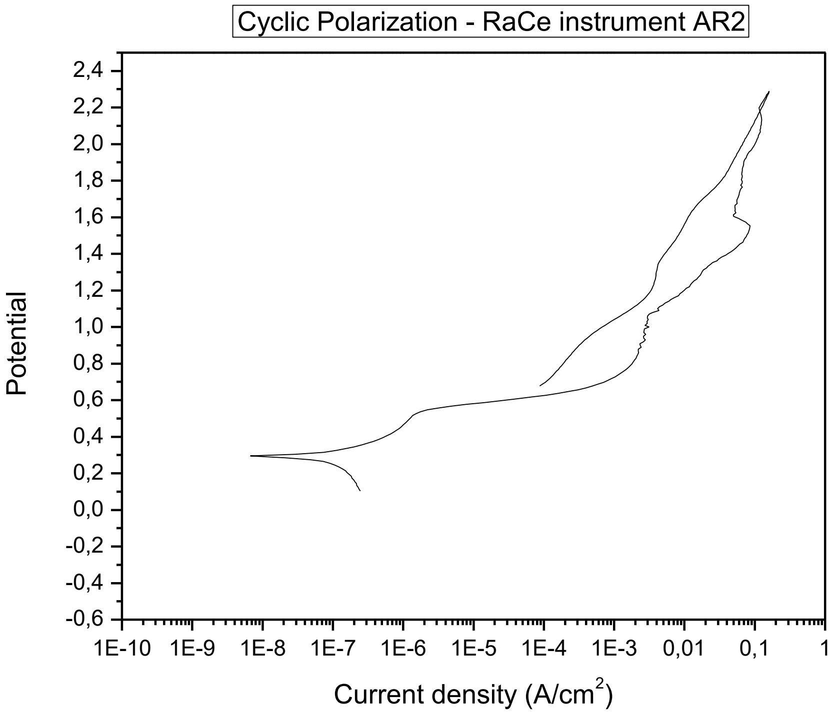

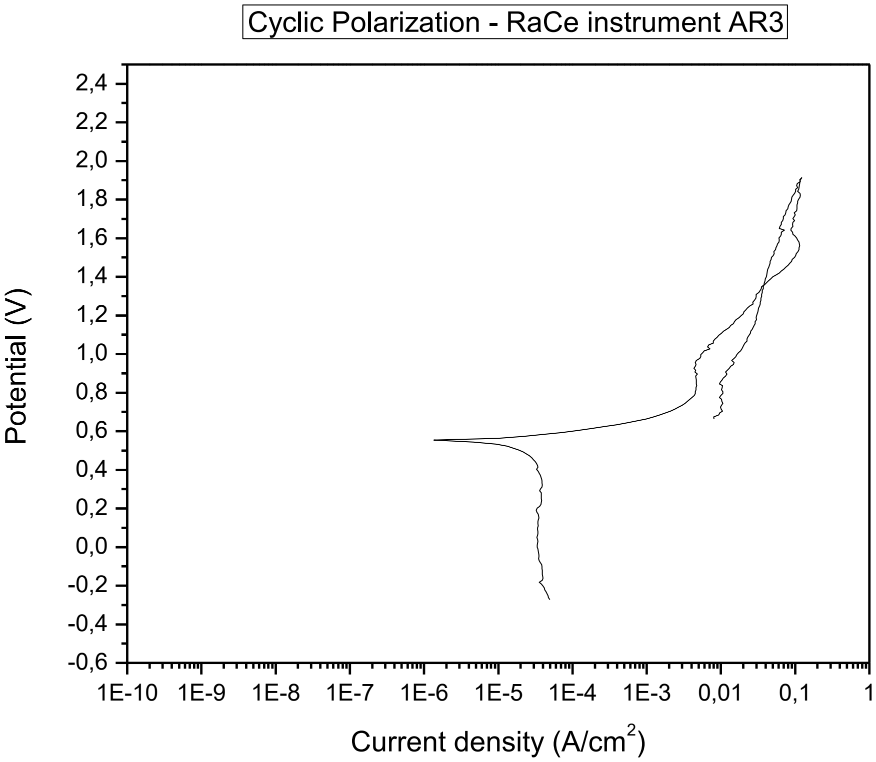
Cyclic Polarization - RaCe instrument AR3
Potential (V)
2,4
2,2
2,0
1,8
1,6
1,4
1,2
1,0
0,8
0,6
0,4
0,2
0,0
-0,2
-0,4
-0,6
1E-10
1E-9
1E-8
1E-7
1E-6
1E-5
1E-4
1E-3
0,01
0,1
1
Current density (A/cm^2)

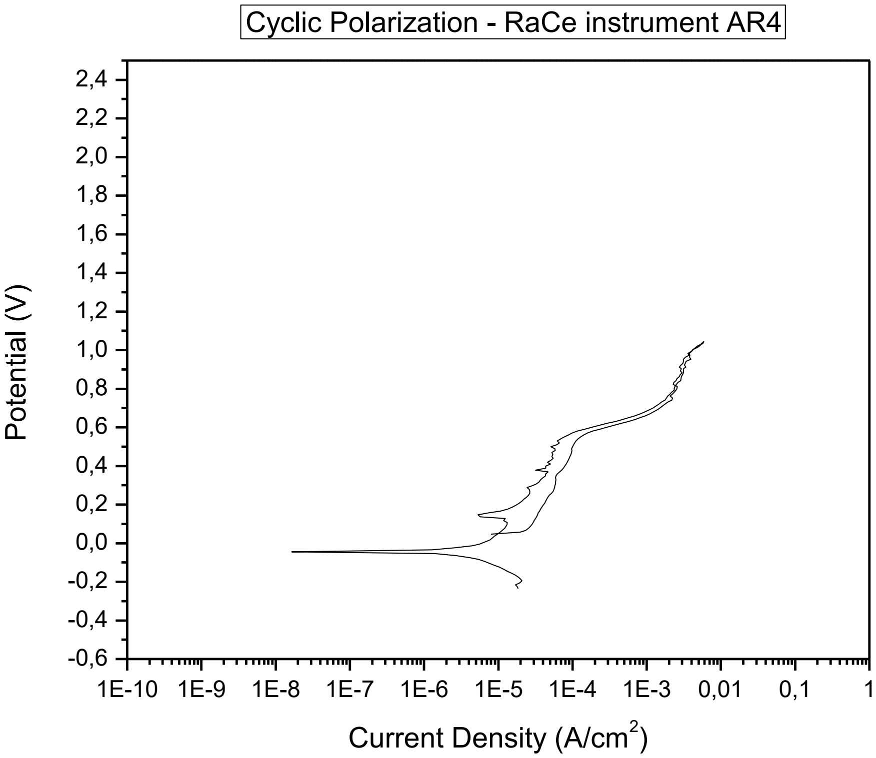
Cyclic Polarization - RaCe instrument AR4
Potential (V)
2,4
2,2
2,0
1,8
1,6
1,4
1,2
1,0
0,8
0,6
0,4
0,2
0,0
-0,2
-0,4
-0,6
1E-10
1E-9
1E-8
1E-7
1E-6
1E-5
1E-4
1E-3
0,01
0,1
1
Current Density (A/cm^2)

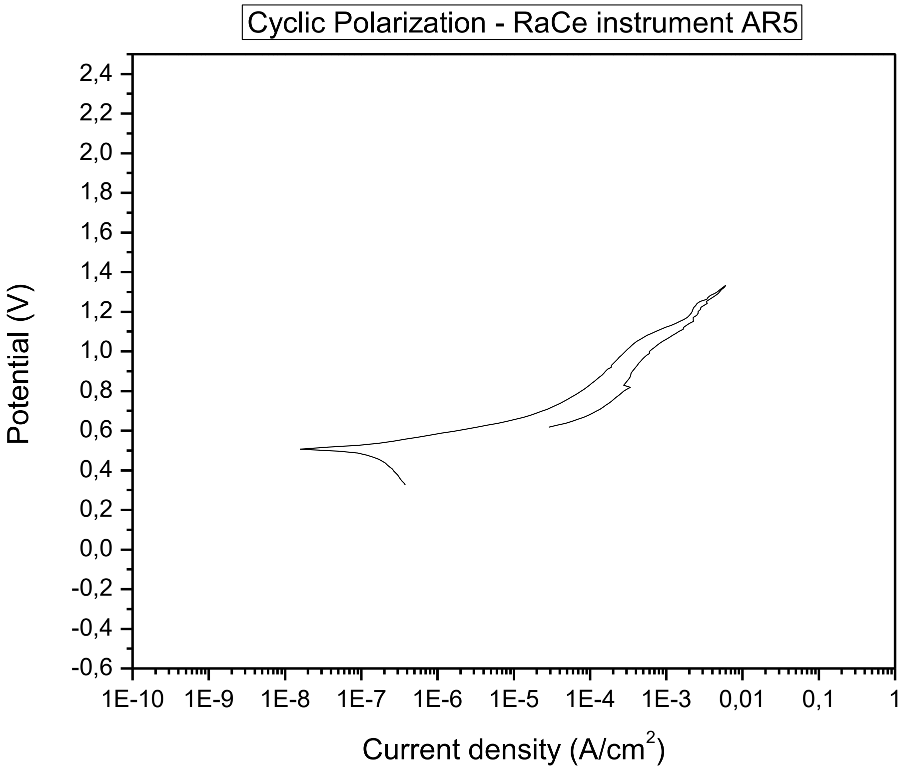
Cyclic Polarization - RaCe instrument AR5
Potential (V)
2,4
2,2
2,0
1,8
1,6
1,4
1,2
1,0
0,8
0,6
0,4
0,2
0,0
-0,2
-0,4
-0,6
1E-10
1E-9
1E-8
1E-7
1E-6
1E-5
1E-4
1E-3
0,01
0,1
1
Current density (A/cm^2)

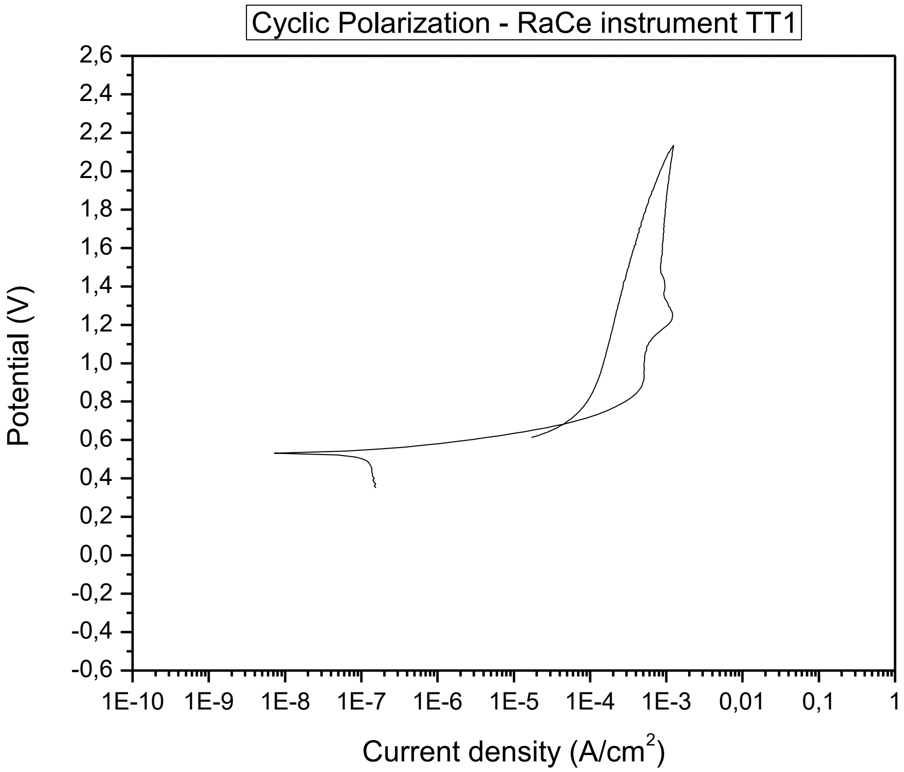
Cyclic Polarization - RaCe instrument TT1
Potential (V)
2,6
2,4
2,2
2,0
1,8
1,6
1,4
1,2
1,0
0,8
0,6
0,4
0,2
0,0
-0,2
-0,4
-0,6
1E-10
1E-9
1E-8
1E-7
1E-6
1E-5
1E-4
1E-3
0,01
0,1
1
Current density (A/cm^2)

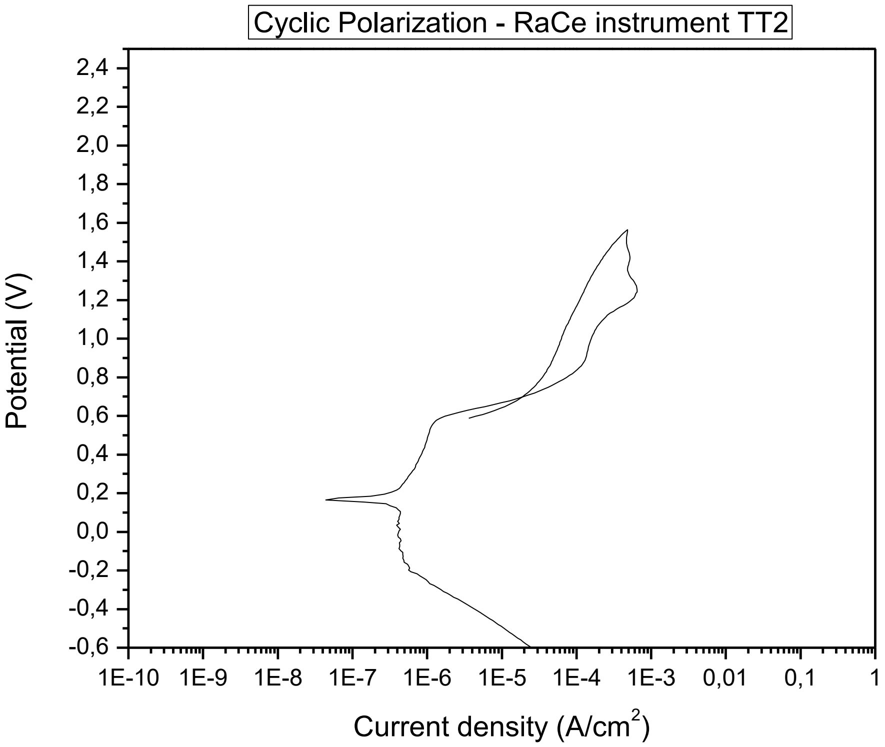
Cyclic Polarization - RaCe instrument TT2
Potential (V)
2,4
2,2
2,0
1,8
1,6
1,4
1,2
1,0
0,8
0,6
0,4
0,2
0,0
-0,2
-0,4
-0,6
1E-10
1E-9
1E-8
1E-7
1E-6
1E-5
1E-4
1E-3
0,01
0,1
1
Current density (A/cm2)

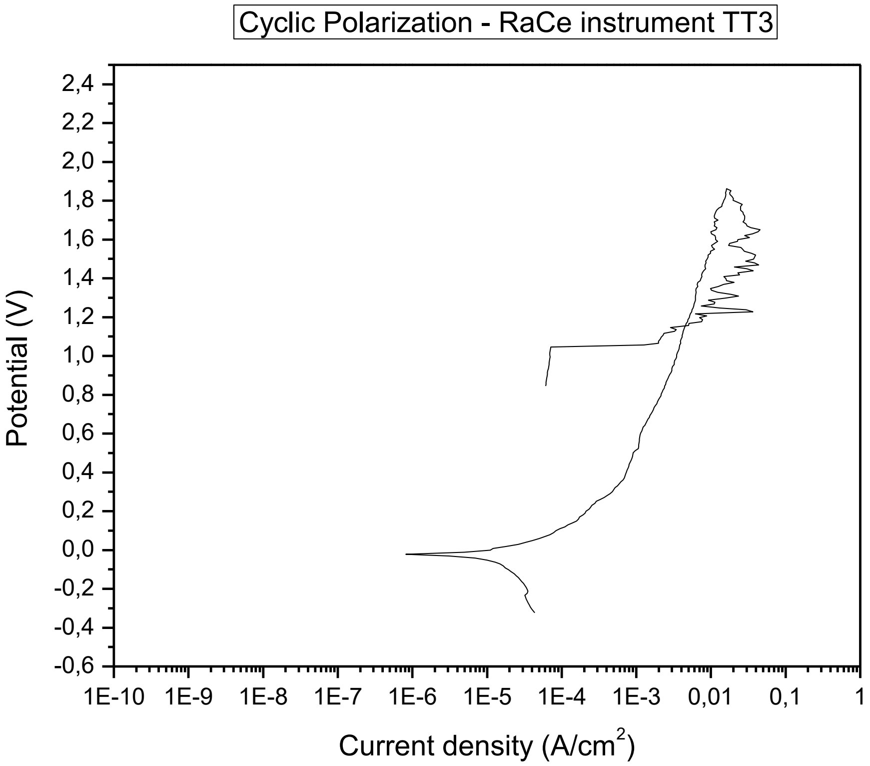
Cyclic Polarization - RaCe instrument TT3
Potential (V)
2,4
2,2
2,0
1,8
1,6
1,4
1,2
1,0
0,8
0,6
0,4
0,2
0,0
-0,2
-0,4
-0,6
1E-10
1E-9
1E-8
1E-7
1E-6
1E-5
1E-4
1E-3
0,01
0,1
1
Current density (A/cm2)

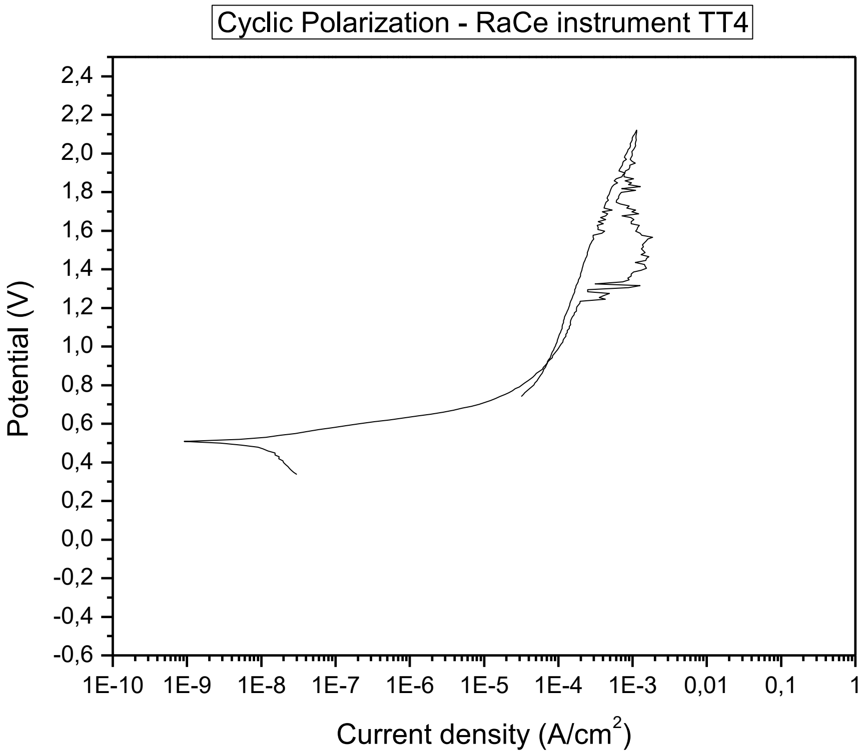
Cyclic Polarization - RaCe instrument TT4

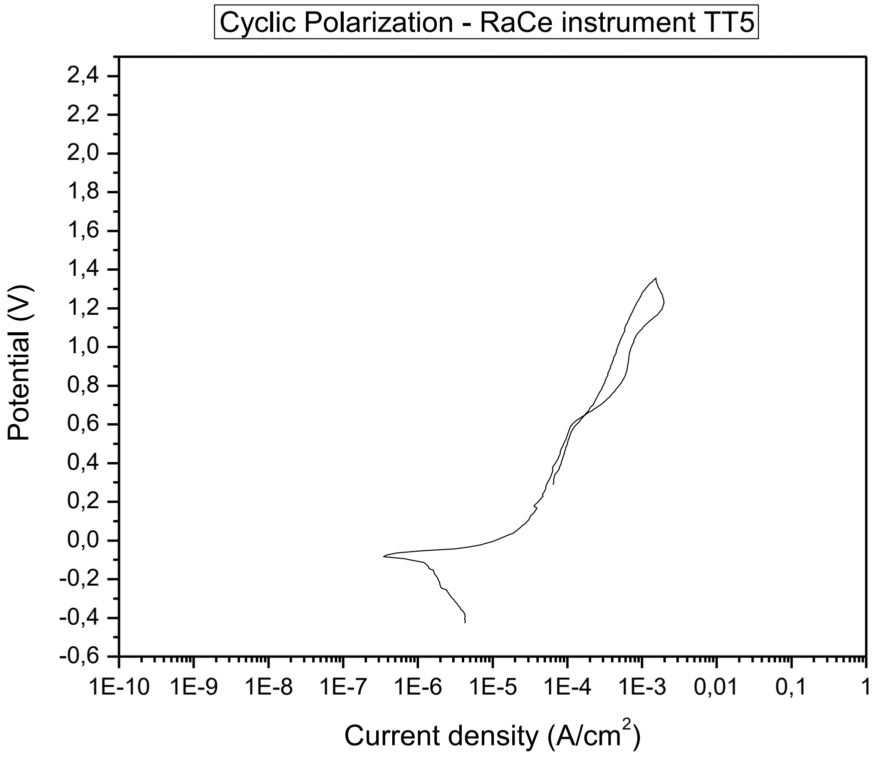
Cyclic Polarization - RaCe instrument TT5

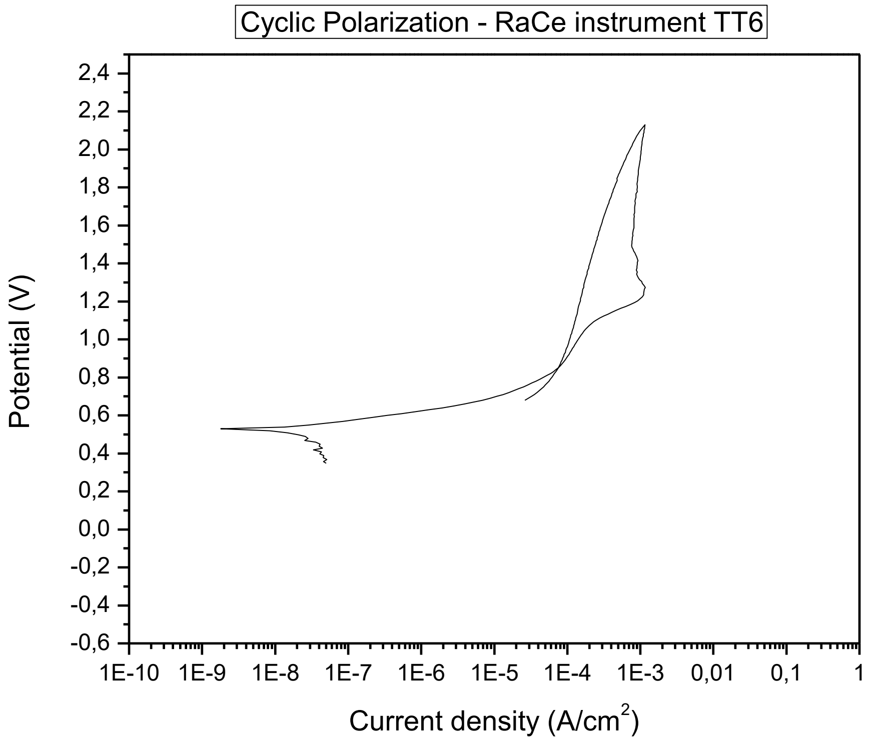
Cyclic Polarization - RaCe instrument TT6
Potential (V)
2,4
2,2
2,0
1,8
1,6
1,4
1,2
1,0
0,8
0,6
0,4
0,2
0,0
-0,2
-0,4
-0,6
1E-10
1E-9
1E-8
1E-7
1E-6
1E-5
1E-4
1E-3
0,01
0,1
1
Current density (A/cm^2)

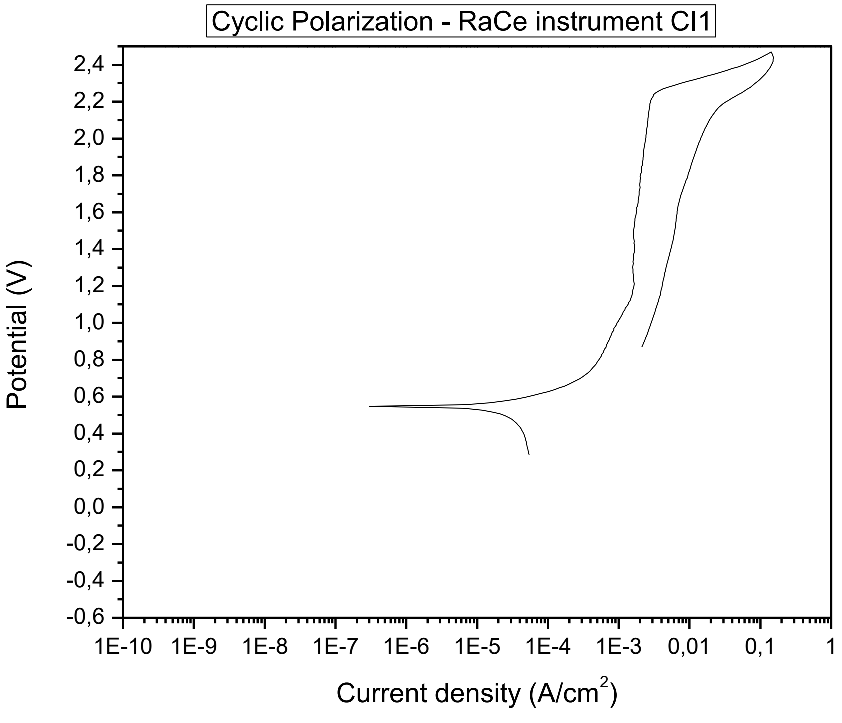
Cyclic Polarization - RaCe instrument CI1
Potential (V)
2,4
2,2
2,0
1,8
1,6
1,4
1,2
1,0
0,8
0,6
0,4
0,2
0,0
-0,2
-0,4
-0,6
1E-10
1E-9
1E-8
1E-7
1E-6
1E-5
1E-4
1E-3
0,01
0,1
1
Current density (A/cm^2)

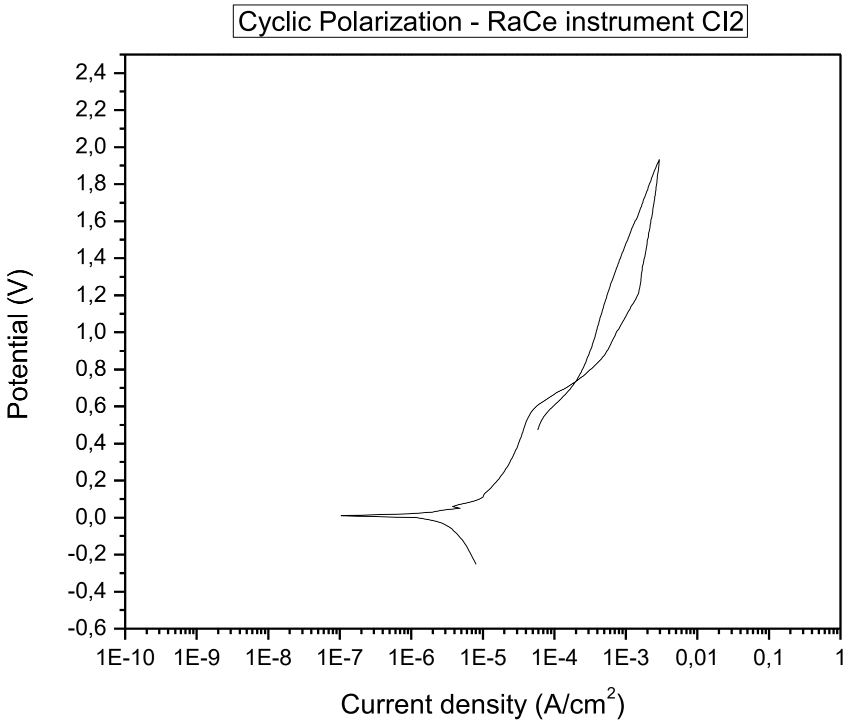
Cyclic Polarization - RaCe instrument CI2
Potential (V)
2,4
2,2
2,0
1,8
1,6
1,4
1,2
1,0
0,8
0,6
0,4
0,2
0,0
-0,2
-0,4
-0,6
1E-10
1E-9
1E-8
1E-7
1E-6
1E-5
1E-4
1E-3
0,01
0,1
1
Current density (A/cm^2)

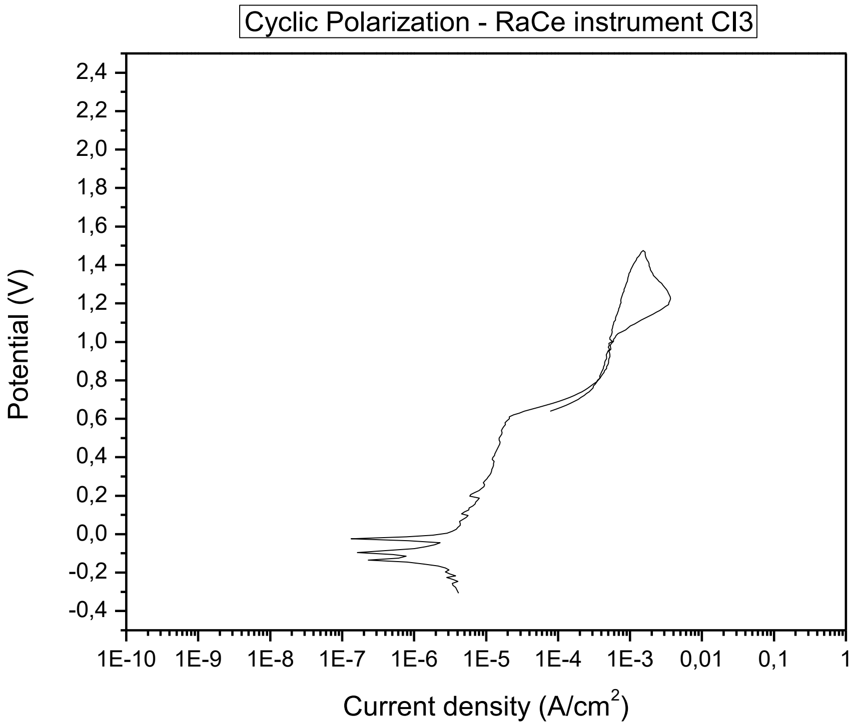
Cyclic Polarization - RaCe instrument CI3
Potential (V)
2,4
2,2
2,0
1,8
1,6
1,4
1,2
1,0
0,8
0,6
0,4
0,2
0,0
-0,2
-0,4
1E-10
1E-9
1E-8
1E-7
1E-6
1E-5
1E-4
1E-3
0,01
0,1
1
Current density (A/cm^2)

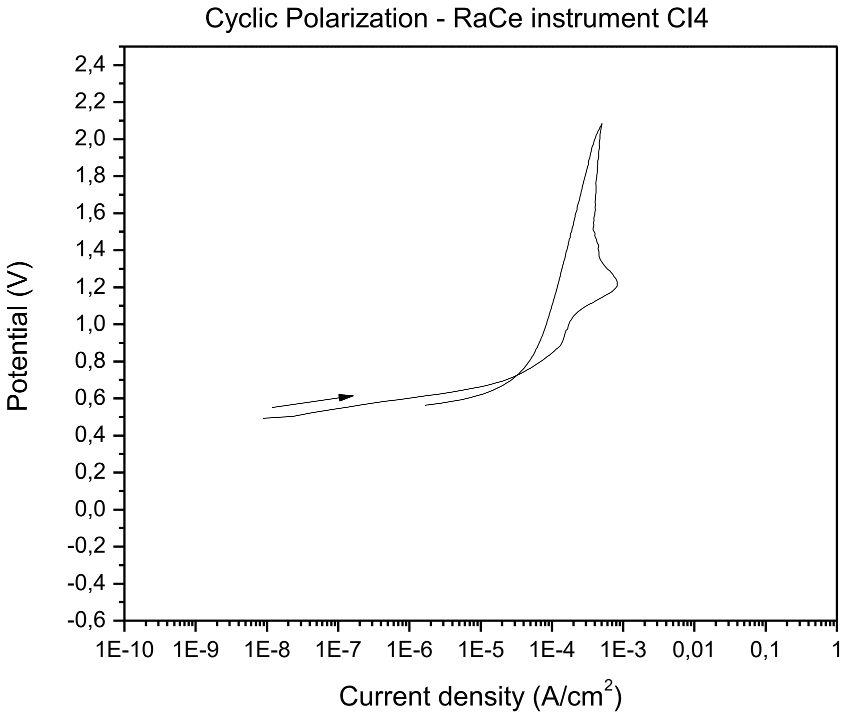
Cyclic Polarization - RaCe instrument CI4

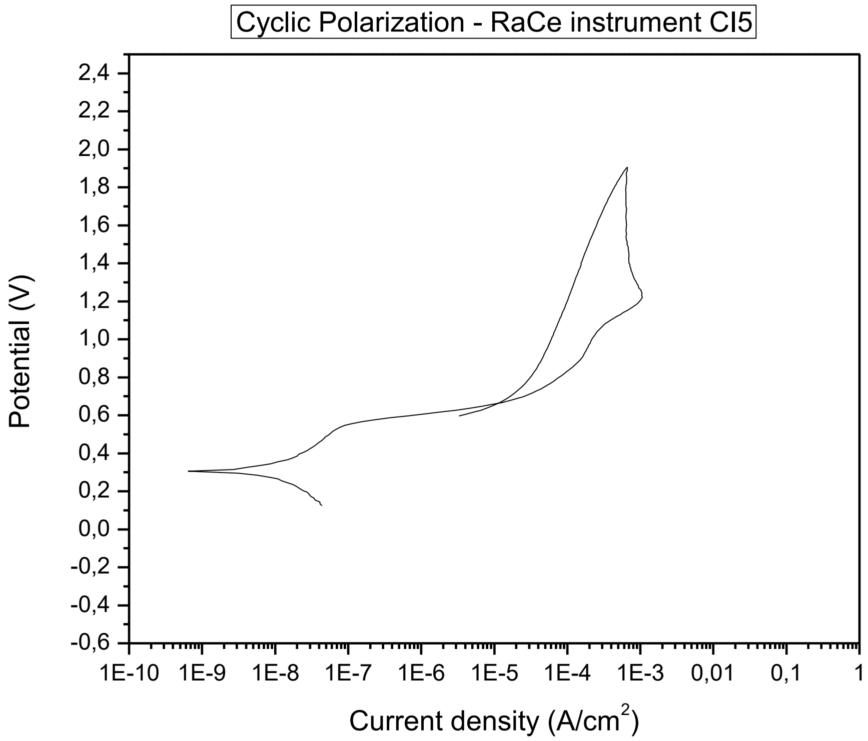
Cyclic Polarization - RaCe instrument CI5

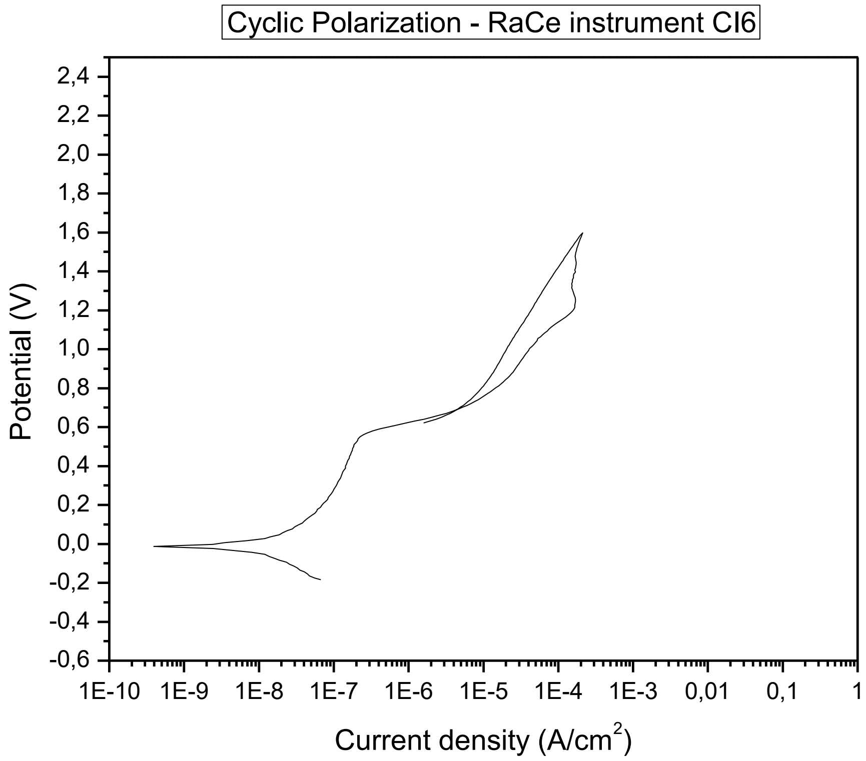
Cyclic Polarization - RaCe instrument CI6
Potential (V)
2,4
2,2
2,0
1,8
1,6
1,4
1,2
1,0
0,8
0,6
0,4
0,2
0,0
-0,2
-0,4
-0,6
1E-10
1E-9
1E-8
1E-7
1E-6
1E-5
1E-4
1E-3
0,01
0,1
1
Current density (A/cm2)